Consortium

for

Small-Scale Modelling

Deutscher Wetterdienst
MeteoSwiss
Ufficio Generale Spazio Aereo e Meteorologia
EΘNIKH METEΩPOΛOΓIKH ΥΠHPEΣIA
Instytucie Meteorogii i Gospodarki Wodnej
Administratia Nationala de Meteorologie
ROSHYDROMET
Agenzia Regionale Protezione Ambiente Piemonte
Agenzia Regionale Prevenzione Ambiente Energia Emilia Romagna
Centro Italiano Ricerche Aerospaziali
Amt für GeoInformationswesen der Bundeswehr
Israel Meteorological Service

www.cosmo-model.org

The COSMO Priority Project $T^2(RC)^2$:

Testing and Tuning of Revised

Cloud Radiation Coupling, Final Report

Project participants:

H. Muskatel[1]‡, **U. Blahak**[2], **P. Khain**[1],

A. Shtivelman[1], **M. Raschendorfer**[2], **M. Kohler**[2],

D. Rieger[2], **O. Fuhrer**[3], **X. Lapillonne**[3],

G. Rivin[4], **N. Chubarova**[4], **M. Shatunova**[4], **A. Poliukhov**[4],

A. Kirsanov[4], **T. Andreadis**[5], **S. Gruber**[6]

‡ Project Coordinator

[1] Israel Meteorological Service - IMS

[2] Deutscher Wetterdienst - DWD

[3] MeteoSwiss - MCH

[4] HydroMetCenter of Russia - RHM

[5] Hellenic National Meteorological Service - HNMS

[6] Karlsruhe Institute of Technology - KIT

Contents

1 Introduction

Radiation transfer schemes are critical part of numerical weather prediction (NWP) models since solar energy is the engine for atmospheric dynamics. The seasonal and diurnal cycles are governed by attenuations in sunshine duration and intensity. The first and most important factor which determines the solar irradiance is the solar zenith angle. This angle is defined by the location on earth and the time and can be accurately calculated from deterministic equations. The second most important effect is the cloud cover, and not less important, the cloud optical thickness. The radiation-clouds are coupled in a two-way manner. The hitting of land and sea surfaces causes the thermodynamic instability that is needed for cloud formation and precipitation but also creates a mask that prevents solar fluxes to penetrate the atmosphere hence reducing the instability. Other constituents that impact the atmosphere opacity are the gasses, mainly H_2O, O_3 and CO_2, and aerosols.

The radiation scheme is a computationally expensive part of most NWP models although many simplifications are considered. Some of the simplifying assumptions used are the reduction of the dimension of the problem from 3D to a 1D problem namely the two-stream approximation in which only upward/downward fluxes are calculated. Another generalization is the use of only few spectral intervals (bands), in COSMO only 8, to describe the entire shortwave (SW) incoming solar radiation and the outgoing long wave (LW) radiation. This is a rough approximation especially for the description of the gasses absorption spectra which is rapidly changing as a function of wavelength. In COSMO radiation scheme the k-distribution method is applied to solve this problem and will be described later in section 4. As for clouds, parametrizations are used to describe the radiation-cloud interaction. First, the bulk cloud properties such as effective size and number concentration are defined from ice and water contents and assumptions about the size distribution functions. Second are the optical properties of the hydrometeors which are parametrized as a function of the effective size. In this project both steps were re-visited. The water droplets and ice particles number concentrations were calculated by more realistic schemes using forecasted aerosols contents to better define the effective size. The optical properties parametrizations of water droplets and ice particles were recalculated using sophisticated spectral integration with an elegant formulation that covers a very wide particles size range therefor allowing the inclusion of both rain and snow in the radiative transfer scheme. In addition, for the first time, the asymmetry factor for which defines the amount of forward vs. backwards scattering, was evaluated as a function of aspect ratio of the ice particles instead of their effective size (the reasoning for this is discussed by Fu, 2007).

In this project we also experimented a new approach for the aerosols input for the radiation. Usually NWP models either use climatology i.e. by Tanre (1983), or by Tegen (1997) which is a computationally cheap choice, or running a fully coupled aerosols-chemistry-atmosphere modules such as COSMO-ART, ICON-ART which are very costly. Here we proposed and realized a quasi-forecasted aerosols scheme. The forecasted aerosols by the full coupled models (in our case CAMS or ICON-ART) are interpolated in space and time into COSMO boundary files by *Int2lm* and are used by the radiation scheme. Of course that in cases of disagreement between COSMO and the aerosols model dynamics, the aerosols input is not ideal, i.e. when washout is present. Nevertheless, the performance is equal or better compared with monthly climatology option with only small computational price.

2 Tasks and achievements

This project was constructed of 12 tasks:

1. Testing and tuning of the new cloud-radiation scheme performance

2. Analysis/Revision of SGS cloudiness in the radiation scheme including LES simulations of cumulus clouds

3. Implementation of CAMS forecasted aerosols in the radiation scheme

4. Adapting switchable single/double precision to the radiation scheme

5. Implementation and testing of the MCSI method

6. Testing the radiation scheme against experimental datasets and benchmark models for clear/cloudy sky conditions

7. Implementation of new ice and water droplets optical properties in ICON-RRTM radiation scheme

8. Implementation and testing of ICON-ART forecasted aerosols in COSMO radiation scheme

9. Implementation and testing of CAMS forecasted aerosols in COSMO microphysical scheme

10. SAM LES utilization for parametrization of sub-grid scale shallow cumulus cloud cover and its testing

11. Updating the COSMO latest version - block structure and GPU compatible

12. Summary and documentations including web-app for cloud optics in COSMO webpage: http://www.cosmo-model.org/content/tasks/operational/ims/cloudOptics/.

The project lasted 4.5 years from September 2015 to March 2020. With the total amount of 10.77 FTEs in human resources coming from 5 institutions. The main achievements in this project are:

1. New optical properties for water and ice hydrometeors. The extinction coefficient, single scattering albedo and asymmetry factors were parametrized following Fu (1996, 1998) and Hu and Stamnes (1993). Extension of the effective size range allowing the inclusion of snow, graupel and rain. For the first time the asymmetry factor is defined as function of aspect ratio. The new parametrizations were applied in both COSMO and ICON models. Results published in Muskatel et al. (2021).

2. The Monte-Carlo Spectral Integration (MCSI) was realized in COSMO. A wise sampling technique that allows a reduction of calculations in the spectral space as an alternative to the usual time or space resolution reduction of the radiation scheme.

3. Implementation of CAMS forecasted aerosols as an input for the radiation (direct effect) and the microphysical processes (indirect effect). These aerosols fields can be used as input for droplet activation applying Segal and Khain (2006) scheme. Ice heterogeneous nucleation of these aerosols can be parametrized using Phillips (2008) or DeMott (2015) ice nucleation schemes.

4. Implementation of ICON-ART forecasted dust as an input for the radiation scheme. Global ICON-ART dust forecast runs semi-operationally twice a day in DWD. Now these 3 aerosols dust species can be used as an input for COSMO radiation scheme while other species of aerosols are taken from Tegen climatology.

5. Implementation of Kinne (2013) aerosols climatology as an input for radiation. This state-of-the-art climatology is based on observational data with finer resolution compared to the previous Tegen (1997) climatology.

6. A new parametrization of effective radius of shallow cumulus clouds using an adiabatic parcel model. As a result, a new sub-grid scale clouds LWC calculation is also applied.

7. A tuning procedure of the new radiation scheme. Around 30 new parameters were introduced in both $(RC)^2$ priority task and the following $T^2(RC)^2$ priority project. These parameters and switches were reduced to only 8 by a sensitivity analysis using the CALMO methodology and the IDEAL COSMO framework. These 8 parameters were fine-tuned by performing repeated 4-months period runs with many different name lists applying the CALMO method. A set of recommended default values is now available.

8. Massive testing of the new radiation scheme in Israel, Russia, Germany and Switzerland performed by IMS, RHM and MCH in many different atmospheric situations. All the mentioned new featured were tested against ground base measurements as well as benchmark models. Different aerosols inputs were compared and evaluated. In IMS the new scheme is semi-operational for two years.

9. The new radiation scheme, CLOUDRAD, with all its features is now available in the official COSMO release and is single/double precision as well as GPU compatible.

10. A web application for cloud optics is available for the public in COSMO webpage. It is suitable for any cloud-radiation modelling scheme in which the user can define the wavelengths intervals and calculate the optical properties parametrizations for both liquid and ice hydrometeors including dynamical graphics and text outputs.

3 New optical properties for water droplets and ice particles in COSMO model

(H. Muskatel, U. Blahak P. Khain)

3.1 Introduction

Radiation transfer through clouds is a key factor in earth's energy cycle and greatly effects the dynamics in the atmosphere. The numerical weather prediction model needs to forecast the amount of clouds, their thickness (LWC, IWC), the hydrometeors concentration and their effective size in order to calculate the amount of radiation transferred, absorbed and scattered by clouds. Having these parameters correctly described, the radiation module can calculate the clouds interaction with the radiation using three optical properties: the extinction coefficient, the single scattering albedo and the asymmetry factor (β_{ext}, ϖ, g). These properties needs to be defines for each hydrometeor separately (ice, liquid and aerosols) but also for each wavelength interval and each particle effective size. In this project we introduced a practical parametrization of both liquid droplets and ice particles optical properties

based on the single wavelength data of Fu (1996, 1998) and Hu and Stamnes (1993). We used an ensemble of 7500 particle size distributions (PSD) which enabled the effective size range to be extended to include larger hydrometeor categories such as rain, snow and graupel.

3.2 Ice Particles

The default COSMO optical properties parametrizations for ice hydrometeors, is based on IWC only. In more advanced models the effective size R_{eff} is used. We adopted the generalized effective size, D_{ge}. It quantities the ratio between the volume and the statistically averaged projected area $(\overline{A})$ of a randomly oriented needle particle (Fu, 1996):

$$D_{ge} = \frac{\int_{Lmin}^{Lmax} DDL \cdot n(L)dL}{\int_{Lmin}^{Lmax} \left[DL + \frac{\sqrt{3}}{4}D^2\right] n(L) dL} = \frac{2\int_{Lmin}^{Lmax} V(L) \cdot n(L)dL}{\sqrt{3}\int_{Lmin}^{Lmax} \overline{A}(L) \cdot n(L)dL} \quad (1)$$

Where D and L are the width and length of the particle, n(L) is the particles size distribution (PSD). In our case we used an ensemble of particles which is assumed to follow a four-parameter modified gamma distribution (MGD):

$$N(L) = N_0 L^{\mu} e^{-\lambda L^{\nu}} \quad (2)$$

$$M_i = \int_0^{\infty} L^i N(L) \, dL = \frac{N_0}{\nu} \frac{\Gamma(\frac{\mu+i+1}{\nu})}{\lambda^{\frac{\mu+i+1}{\nu}}} \quad (3)$$

$$\overline{L} = \frac{M_1}{M_0} = \frac{\Gamma(\frac{\mu+2}{\nu})}{\Gamma(\frac{\mu+1}{\nu})} \lambda^{\frac{-1}{\nu}} \quad (4)$$

where No is the scale parameter and μ, ν, λ control the shape of the distribution, M_i is the size distribution i^{th} moment, and $\overline{L}$ is the mean particle length. A simpler gamma distribution is obtained by setting $\nu = 1$ hence:

$$\overline{L} = \frac{\mu+1}{\lambda} \quad (5)$$

We compose 7500 PSD ensemble by a systematic variation of the PSD parameters within a wide range. We change $\overline{L}$ in the range of 5-3000 μm in 500 logarithmically equidistant steps, while μ is changed from 0 to 14 which resulted D_{ge} to be in the range of 5-600 μm.

The asymmetry factor, as proved from ray scattering simulations for many types of ice crystals, dependents less on size and shape rather on the particle's effective aspect ratio (Fu, 2007):

$$AR = \int_{Lmin}^{Lmax} (\frac{D}{L}) \cdot \overline{A} \cdot n(L) / \int_{Lmin}^{Lmax} \overline{A} \cdot n(L) \, dL \quad (6)$$

The optical properties can be parametrized as a function of D_{ge} and IWC which for hexagonal particles is:

$$IWC = \frac{3\sqrt{3}}{8} \rho_{ice} \int_{Lmin}^{Lmax} D \cdot D \cdot L \cdot n(L)dL \quad (7)$$

ρ_{ice} is the bulk ice density ($0.917 \, g \cdot cm^{-3}$). D_{ge} and AR can be evaluated from the mass-size relation used by the cloud microphysics scheme, for example, $m = aL^b$ where m is the particle mass. The raw data for the single particle extinction and scattering cross sections (σ_{ext}, σ_{sca}), asymmetry factor (g_p) and the forward scattering δ-function peak (f_{δ}) were taken from Fu (1996) and Fu et al. (1998).

The technique of spectral averaging over wide bands depends on the parameter one desires to compute the spectral integration technique is explained in details in Muskatel et al. (2021).

We parametrize $\overline{\beta'_{ext}}, \overline{\omega}, \overline{g}, \overline{f_d}$ as function of D_{ge} and AR by fitting rational functions division in the Padé approximation form:

$$f_{(x)} = \frac{\sum_i^N a_i x^i}{\sum_i^M b_i x^i} \tag{8}$$

Where x can be D_{ge} or AR and a_i, b_i are fitting coefficients. This requires a non-linear fitting algorithm like Levenberg-Marquardt, but it is very flexible and can reproduce nearly any asymptotic behaviour if N, M are chosen adequately. If $N = M$, an asymptotic convergence to a constant for $x \to \infty$ results. If $N < M$, the function converges to 0. For $\beta'_{ext}(D_{ge})$ we chose $N = 2$; $M = 3$, for $\omega(D_{ge})$ and $f_d(AR)$ we defined $N = 3$; $M = 3$ while for $g(AR)$ we put $N = 3$; $M = 2$. An example for the parametrization fit can be seen in Fig. 1 The asymmetry factor presented in Fig. 1 was calculated for particles with smooth surfaces, where the forward scattered peak (delta fraction f_d) is large because of the plane-parallel surfaces of the ice particles. However, real particles might have rough surfaces, where the forward scattering is smaller. The asymmetry factor for rough surfaces can be defined as (Fu 2007):

$$g_r = \frac{g - f_d}{1 - f_d} \tag{9}$$

An example for f_d and g_r parametrization fit can be seen in Fig. 2.

In the original RG92-formulation, the scattering phase function is approximated by the so-called δup-Eddington approximation, which is a sum of a general two-term Legendre-polynomial expansion of the phase function plus a delta-forward peak, weighted by the forward scattered fraction f (Joseph et al. 1976). This approximation is "tuned" to the original phase function by matching of g, which is the first moment of the phase function, and by requiring that $f = g^2$, which follows from the matching of the second moment of the phase function with that of the Henvey-Greenstein function.

For ice particles in the visible spectral range, we now allow the formulation in a way that f is an independent free parameter (Fu 2007):

$$f_{rough} = \frac{1}{2\omega(D_{ge})} \qquad and \qquad f_{smooth} = \frac{1}{2\omega(D_{ge})} + f_d \tag{10}$$

where f is limited so that it cannot be larger than g^2.
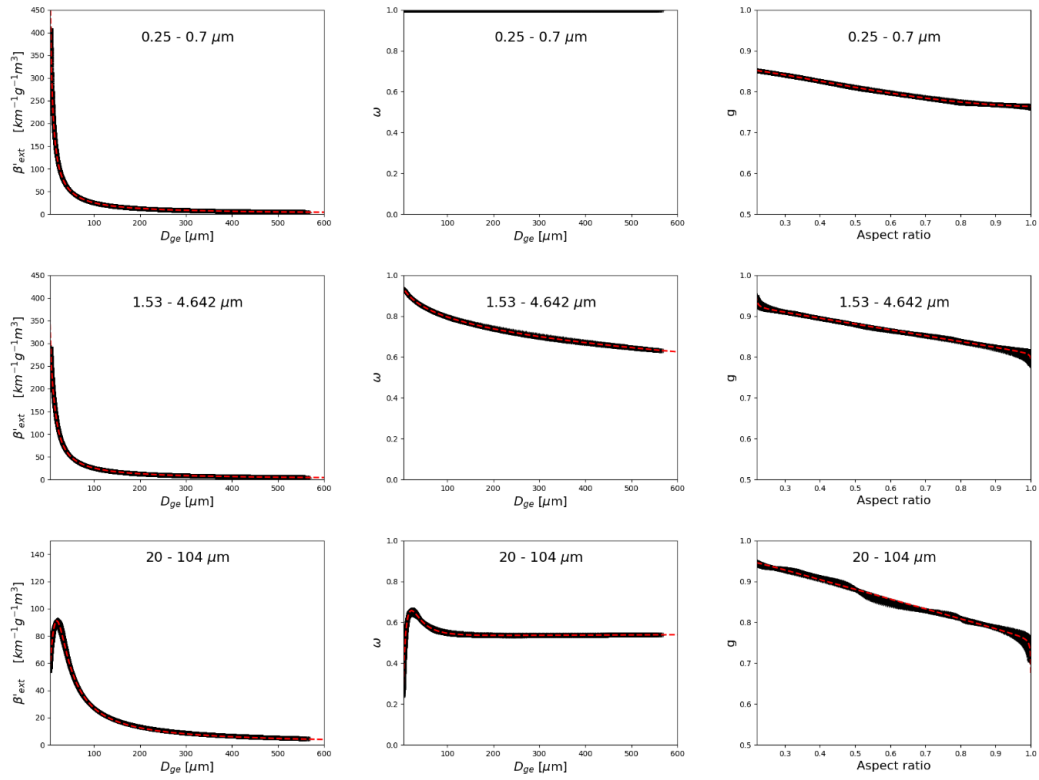
Figure 1: Parametrizations for β'_{ext} (volume extinction coefficient divided by IWC, i.e., mass extinction coefficient) (left column), single scattering albedo (centre column) and asymmetry factor (right column). The upper, middle and lower rows refers to wavelengths of 0.25-0.7 μm, 1.53-4.64 μm and 20-104 μm COSMO intervals respectively. The black line is composed of 7500 individual points, each represents a different PSD, and the red dashed line denotes the parametrization fit model.
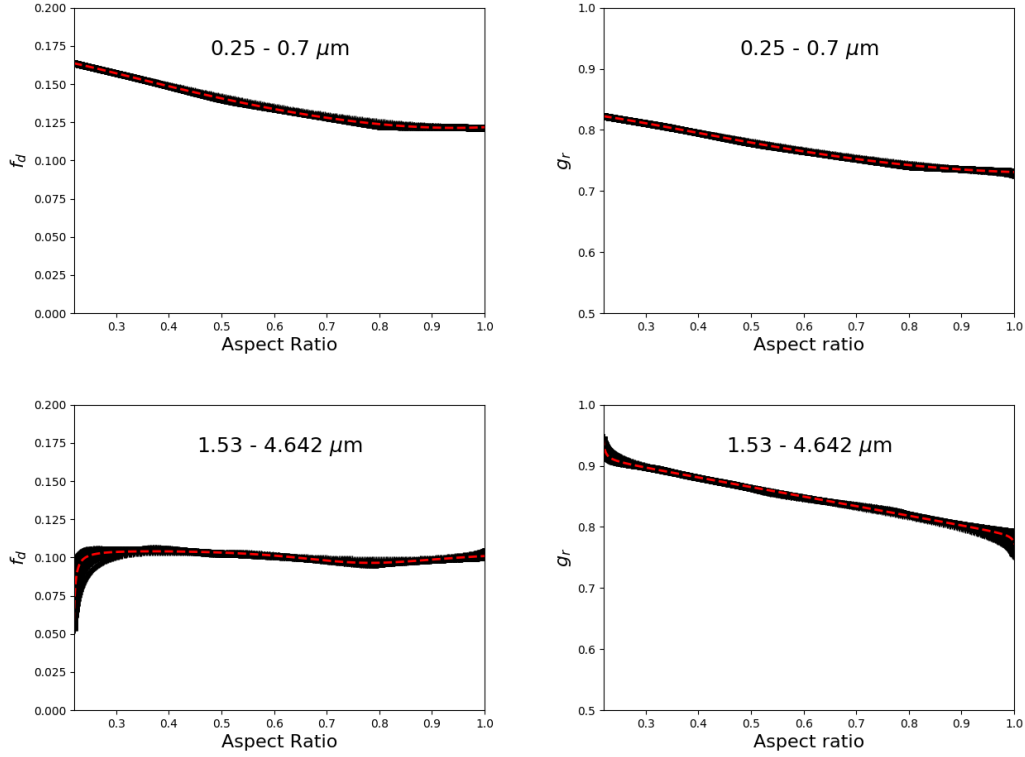
Figure 2: Parametrizations for delta fraction (left) and rough surface particle asymmetry factor (right). The upper and lower rows refers to wavelengths of 0.25-0.7 μm and 1.53-4.64 μm intervals respectively.

3.3 Water droplets

The default COSMO optical properties parametrizations are based on Mie calculations by Stephens (1989) and the parametrizations proposed by Slingo and Schrecker (1982) for water clouds. The effective radius for the quasi-spherical water droplets is define as:

$$R_e = \frac{1}{2} \int_0^\infty D^3 N(D) \, dD / \int_0^\infty D^2 N(D) \, dD = M_3/(2M_2) \tag{11}$$

This definition is motivated by the large-size limit where β'_{ext} is directly proportional to R_e^{-1}:

$$\lim_{D/\lambda \to \infty} \frac{\sigma_{ext}}{A_{geo}} \; ; \quad A_{geo} = \frac{\pi}{4} D^2 \tag{12}$$

$$\beta'_{ext} \equiv \frac{\beta_{ext}}{LWC} = \frac{2\frac{\pi}{4} M_2}{\frac{\pi}{6} \rho_w M_3} = \frac{3}{2\rho_w R_e} \tag{13}$$

$$R_e = \frac{1}{2} \frac{M_3}{M_2} = c_1 \left(\frac{LWC}{n_w} \right)^{c_2} \tag{14}$$

Where A_{geo} is the geometric cross section of a spherical droplet, LWC is the liquid water content, n_w, ρ_w are the number concentration and bulk density of water, respectively. The constant coefficients c_1, c_2 depend on the constant mass-size-relation parameters and on the size distribution parameters. Based on Mie calculations performed by Hu and Stamnes (1993) (HS93) and using the spectral averaging technique described in the previous section,

11

we applied the calculation to the 8 COSMO wavelength intervals. The same choices for $\rho_{w,max} = 1\ gm^{-3}$, $\Delta z_{min} = 100\ m$ and $\Delta z_{max} = 600\ m$ as was chosen for ice, are used here. We used the same fitting formula as for ice but with $N = 3$; $M = 4$, for $\beta'_{ext}(R_e)$ while for $\omega(R_e)$ and $g(R_e)$ we defined $N = 3$; $M = 3$. The three size sub-ranges of fitting used by HS93 where replaced with one formula that fits all ranges and is valid in the range $2.5\ \mu m \to \infty$. An example for the parametrization fit can be seen in Fig. 3.
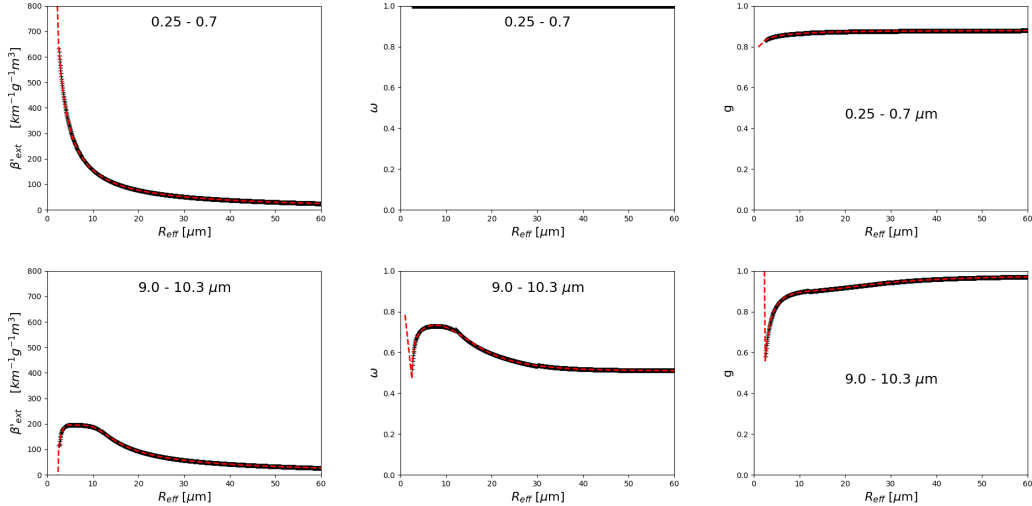
Figure 3: Parametrizations for volume extinction coefficient divided by LWC (left), single scattering albedo (centre) and asymmetry factor (right). The upper and lower rows refers to wavelengths of 0.25-0.7 μm and 9.0 - 10.3 μm intervals respectively. The black line is composed of HS93 original data spectrally averaged for our wavelength intervals and the red dashed line denotes the parametrization fit model. As can be seen from the plots, the fit is invalid for effective radius smaller than 2.5 μm. These fits showed asymptotic behaviour up to 7000 μm (not shown here).

3.4 Sensitivity Experiments

We examined the impact of the new optical properties parametrizations on the radiation transfer, and compare it with the default COSMO radiation scheme (RG92 thereafter) under different cloudiness situations. For that purpose, we have utilized the idealized version of the COSMO model to simulate radiation transfer through two types of clouds: warm stratus and cirrus. The characteristics of the simulated clouds are summarized in Table 1.

The implementation of new parametrizations generally influences the global radiation both directly and indirectly. The change in radiative heating leads to different evolution of the simulated cloud, which in turn influences the radiation transfer. For simplification, we ignored this feedback mechanism, namely removed the radiative heating term in the equation for temperature tendency. All the idealized COSMO simulations were performed between 10:00 and 16:00 UTC, while the zenith angle was fixed to 30°. The domain was chosen to be 100x100 km² around 30° N, with periodic boundary conditions and horizontal resolution of 0.025° (∼2.5 km). Both deep and shallow convection Tiedtke-type schemes were switched off. Each simulation was initiated with vertical profiles of temperature and humidity suitable for stratiform cloud formation at the chosen heights. During the run period the simulated clouds slightly changed due to evaporation, particles sedimentation, and other processes.

Experiment	Warm stratus	Cirrus
1	2.2-2.7km, 279.2-281.4K	9.5-10.75km, 230.8-218.8K
2	2.0-2.7km, 280.0-281.4K	7.5-10.75km, 250.0-218.8K
3	2.0-3.3km, 280.0-279.0K	7.5-12.20km, 250.0-214.8K
4	1.7-3.3km, 280.4-278.2K	
5	1.5-3.3km, 282.0-279.0K	
6	1.2-3.3km, 284.4-280.2K	
7	1.0-3.3km, 286.0-281.0K	

Table 1: Characteristics of the simulated clouds in sensitivity tests using ideal COSMO framework.

However, they continuously covered the entire simulation domain homogeneously. For each simulation, the output fields (global radiation, total water path, etc.) at 5 min steps were averaged over the domain. Ignoring the first 50 min stabilization period, we obtained 51 values for each field for each simulation. Fig. 4 compares the global radiation of default RG92 and new parametrization for the 7 experiments of warm stratus. The global radiation is shown versus liquid water path. Obviously, the global radiation is smaller for thicker clouds. One can see that in the new version the clouds are optically thinner than in RG92. The global radiation difference is larger for thicker clouds, reaching 20%.

As explained in Section 3, the new scheme parametrizes the effect of cloud water number concentration on the effective radius, which influences the optical properties and the global radiation. Thus, for warm stratus of experiment 5, six more runs were performed with various number concentrations. Fig. 4b shows the effect of cloud water number concentration on the global radiation in the new scheme. In contrast to RG92 where the effective radius was not dependent on number concentration, the new scheme shows significant effect of number concentration and effective radius on the global radiation. Having the same liquid water path, a pristine cloud (number concentration of 10 cm^{-3}) may double the global radiation compared to a polluted one (1000 cm^{-3}).
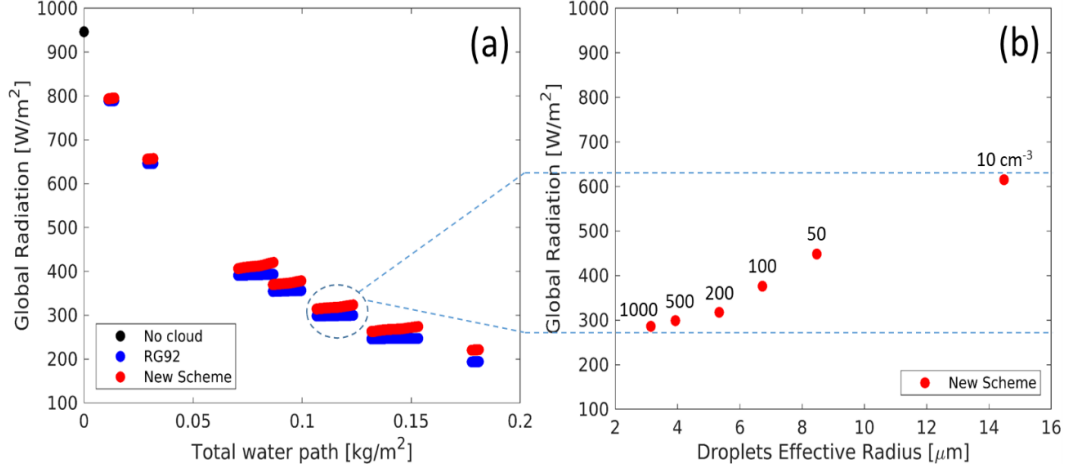
Figure 4: (a) Global radiation versus liquid water path for 7 experiments of warm stratus assuming cloud water number concentration of 500 cm-3. The clear sky reference is marked by black dot. The default COSMO radiation scheme RG92 (blue dots) and the new scheme (red dots) are presented. (b) Global radiation (red dots) in the new scheme versus cloud-averaged droplets effective radius for experiment 5 of warm stratus (see Table 1) marked by dashed circle. The red dots from left to right correspond to cloud water number concentrations of 1000, 500, 200, 100, 50, 10 cm^{-3}. The range of variation in global radiation due to change in effective radius is marked by dashed lines.

Similarly to warm stratus presented in Fig. 4a, Fig. 5a shows the global radiation versus ice water path for the 3 experiments of cirrus (see Table 1). In addition to the default RG92 (blue dots), four more versions of the new parametrization are presented (see Section 2 for details): First assumes rough ice particles surfaces (red dots), the second is similar to the first but adding snow particles into consideration (lime green), the third is similar to the second but assuming smooth surfaces (magenta) and the last is similar to the previous but using the forward scattered fraction approximation of f =g^2 instead of the Fu (2007) formulas (cyan). Obviously the global radiation is smaller for thicker clouds. In contrast to warm stratus, the cirrus cloud in the new versions is optically thicker than in RG92. The largest difference from RG92 occurs when assuming rough ice particles and considering snow effect on radiation, where the effect on the global radiation reaches 15% (for thick cirrus - experiment 3). Note that considering snow significantly reduces the global radiation (from red to lime green). Note also that assumption of smooth surfaces makes the clouds optically thinner (from lime green to magenta and cyan), and that there is no significant effect of the different assumptions for forward scattered fraction f (cyan and magenta).

As mentioned, D_{ge} is calculated in the model from ice water content and number concentration which is a function of temperature. In order to highlight the sensitivity of global radiation to D_{ge}, we artificially determine a constant D_{ge} value at all cloudy grid points. Thus, for cirrus of experiment 2, six more runs were performed with various D_{ge} values between 5 and 200 micron. The new version with the assumption of rough needles ignoring snow effect (red dots in Fig. 5a) was chosen for these runs. Fig. 5b shows the influence of D_{ge} on the global radiation in the new scheme. In contrast to RG92 where D_{ge} was not even introduced, the new scheme shows significant effect of D_{ge} on the global radiation. Having the same ice water path, a cirrus cloud with large particles (effective diameter of 200 micron) may yield 10% higher global radiation than an identical cloud with small particles (effective diameter of 5 micron).

14
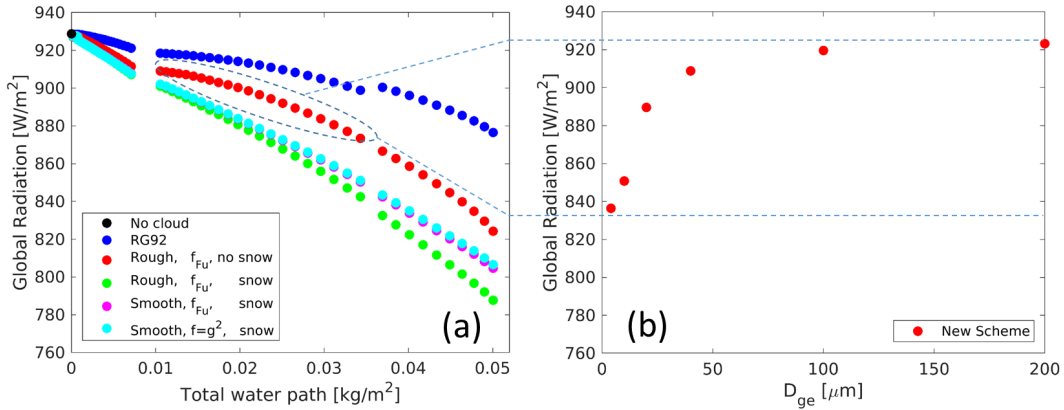
Figure 5: (a) Global radiation versus liquid water path for 3 experiments of cirrus. The clear sky reference is marked by black dot. In blue dots - the default COSMO radiation scheme RG92, red dots represents simulation which assumes rough ice particles surfaces and ignoring snow particles, lime grin dots is the result when snow particles are considered, the same but assuming smooth surfaces are in magenta and the last, in cyan, is similar to the previous but using the forward scattered fraction approximation of $f=g^2$ instead of the Fu (2007) formulas. (b) Global radiation in the Third version of the new scheme (red dots) versus cloud-averaged ice particles effective diameter for experiment 2 of cirrus (see Table 1) marked by dashed circle. The range of variation in global radiation due to change in ice particles effective diameter is marked by dashed lines.

The important quantity for climate applications is the net heating/cooling effect of the clouds. Usually during the day time the SW incoming radiation heats the atmosphere, which is then cooled down via LW outgoing radiation during night time. We cannot discuss this quantity here since our 6 hour long simulations. However, we can check the effect of the new scheme on the net radiation at top-of-atmosphere (incoming minus outgoing). Fig. 6 presents net top-of-atmosphere radiation difference between the new scheme and RG92 versus liquid water path for 7 experiments of warm stratus (Fig. 6a) and versus liquid water path for 3 experiments of cirrus (Fig. 6b). Positive (negative) values indicate warming (cooling) effect by the new scheme with respect to RG92. In Fig. 6b the differences (with respect to RG92) are calculated for the same 4 versions of the new scheme as described in Fig. 5. One can see that the new scheme has warming effect with respect to RG92 for warm stratus, and cooling effect for cirrus. Generally these effects are enhanced (in absolute values) for optically thicker clouds. Note that the assumptions regarding the roughness of the needles surfaces are of low importance for the net radiation (compare cyan, magenta and red dots on Fig. 6b). It is nicely seen that the consideration of snow enhances the net cooling, which can be explained by increase of the cloud albedo.
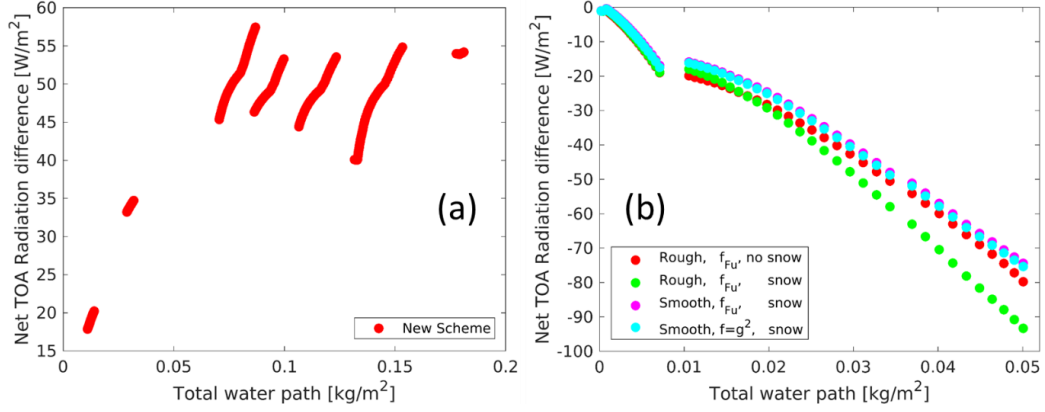
Figure 6: (a) Net (incoming minus outgoing) top-of-atmosphere radiation difference between the new scheme and RG92, versus liquid water path for 7 experiments of warm stratus. Positive values indicate warming effect by the new scheme with respect to RG92. (b) Net top-of-atmosphere radiation difference between the 4 versions of the new scheme and RG92, versus liquid water path for 3 experiments of cirrus (colours details are in the legend of Fig. 5a). Negative values indicate cooling effect by the new scheme with respect to RG92.

3.5   Conclusions and recommendations

The new cloud optics were tested not only in the ideal setup, as detailed in the previous section, but also tested in numerous test cases which will be described in the following sections. We recommend applying the new optics by using iradpar_cloud = 4 with minimal risk. We also recommend choosing lrad_ice_smooth_surfaces = .false. which means that the ice particles will be treated as having rough surfaces. The reasoning behind this recommendation is that rough surfaces ice particles better represents the shape variability. The net radiation on ground will be reduced by few percent having large amounts of ice and snow due to the reduction of forward scattering.

Other recommendation for the new cloud-optics would be: lrad_ice_fd_is_gsquared = .false. which means calculating the forward scattering peak using Fu (2007) formula, lrad_incl_qrqsqg=.true. to include rain, snow and graupel in the radiation scheme and using the large-size approximation by choosing lrad_use_largesizeapprox=.true. Other namelist recommendations can be seen in the appendix of section 3 (upper Air) in COSMO Newsletter No. 19 (October 2019).

A web application for ice and liquid hydrometeors optical properties parametrizations based on this work was created and available for the use of radiation models developers in COSMO webpage. In this web application (www.cosmo-model.org/content/tasks/operational/ims/cloudOptics) developers can insert model spectral integrals and produce parametrizations for ice and liquid hydrometeors including editable graphics.

4 Monte-Carlo Spectral Integration

(H. Muskatel)

4.1 Radiation scheme call-time temporal resolution

Radiation transfer schemes are one of the most computational expensive components in numerical weather prediction (NWP) models. In COSMO model, with only eight spectral intervals, a full radiation calculation costs as much as eight times the cost of the entire COSMO model run. Most of NWP models compromise on the spatial and/or temporal resolution of the radiation scheme. In the operational setup of COSMO-2.8 km, with a full spatial resolution and with a temporal resolution of 15 minutes, the computational cost of radiation is only 3% of the entire model (see Fig. 7).
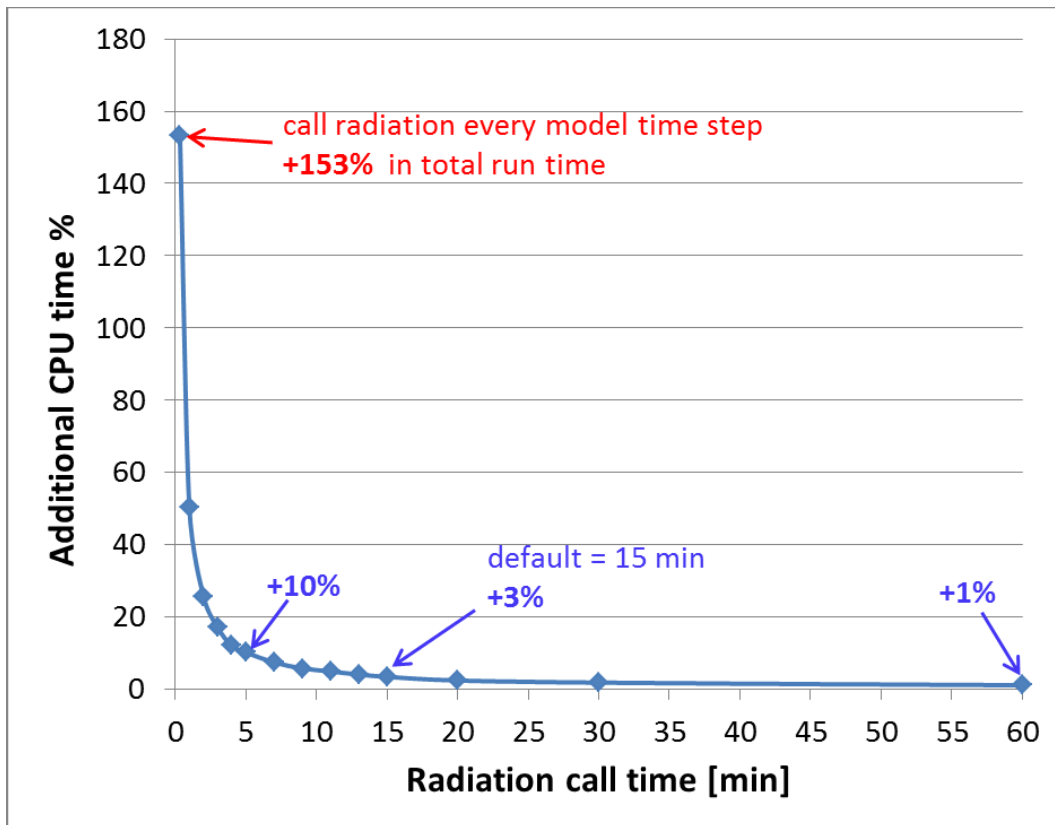
Figure 7: The additional COSMO-2.8km model runtime as function of radiation scheme call temporal resolution. I.e. calling the radiation scheme every 60 minutes adds 1% to total runtime, default resolution of 15 minutes costs 3% increase and calling evry model time step will result more than a double runtime compared with running COSMO with no radiation calculation.

This compromise can lead to local biases in net downward radiation and surface temperatures. To evaluate the magnitude of this effect we chose the 23-25 of April 2015 test case in the IMS-COSMO-2.8km domain. At this period, partial cloudiness and high wind speeds were experienced. The multiple model runs were performed with different radiation temporal resolutions from every model time step (20 seconds) up to 60 minutes. We treat the model

17

highest temporal resolution as the control run. The model's net downward radiation (global radiation) and 2m temperatures biases for three temporal resolutions: 60, 15, 5 minutes are displayed in Fig. 8. It is clear that the biases appears in the presence of clouds. Also, the biases grow larger in area and magnitudes when the radiation calls separation is larger. In Fig. 9 a domain average of the same experiment are presented. The three lines represents different lead time. It is shown here that there is almost a linear dependency of radiation (left panel) and temperature (right panel) biases as function of temporal resolution and that the biases grow larger for longer runtime. Notice that the line for the 34 hours lead time (blue) is almost flat meaning that there is very weak dependency on temporal resolution at this time. The reason is the clear skies conditions in the second day compared with the cloudiness in the first and third day of the simulation.
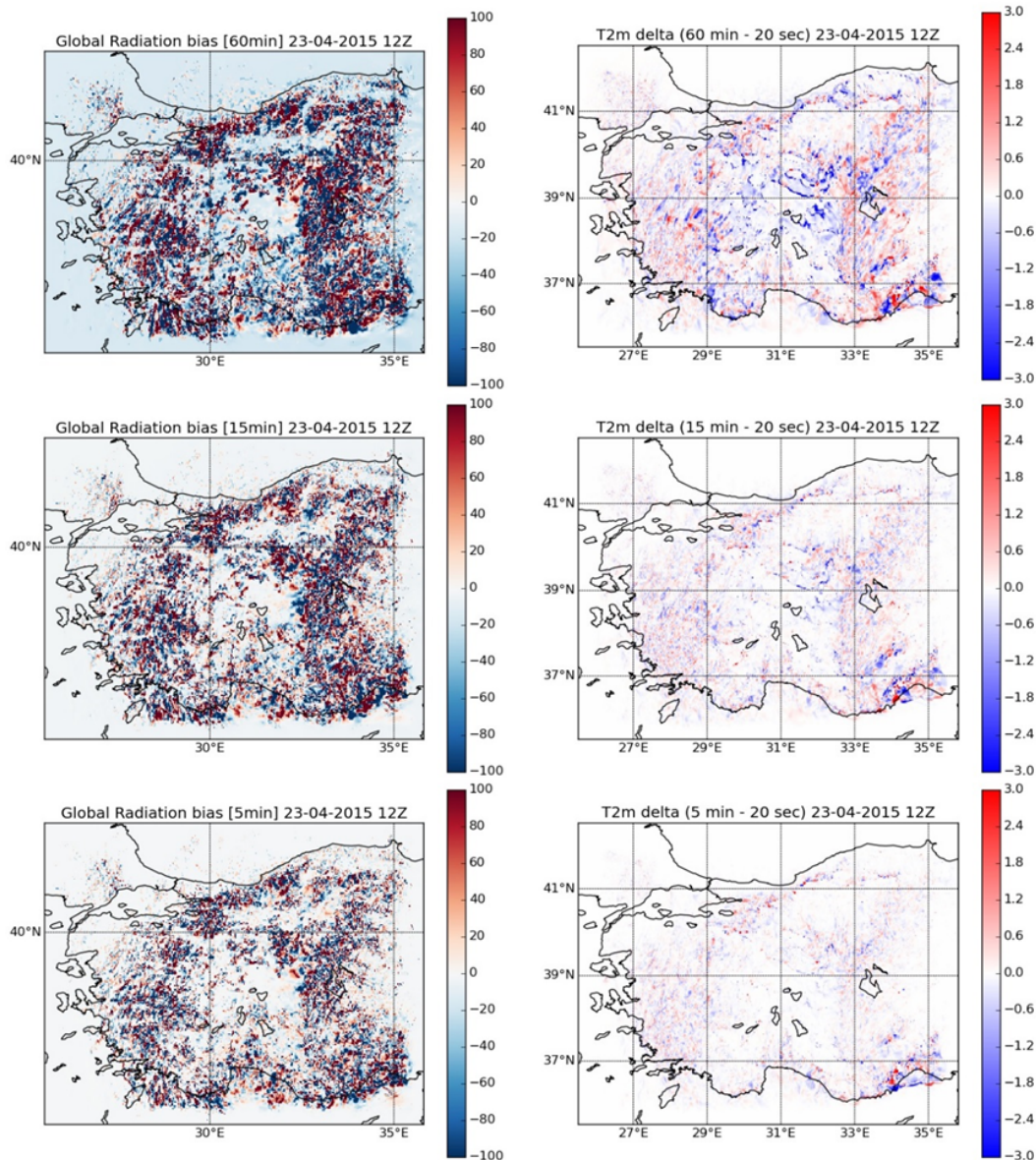
Figure 8: Global radiation (left panels) and 2m Temperature biases (right panels) for three different radiation scheme temporal resolutions 60 min. (upper), 15 min. (middle) and 5 min. (lower) compared with a full temporal resolution (every model time step of 20 seconds). A three days simulation of COSMO-2.8km in IMS domain 23-25 April 2015.
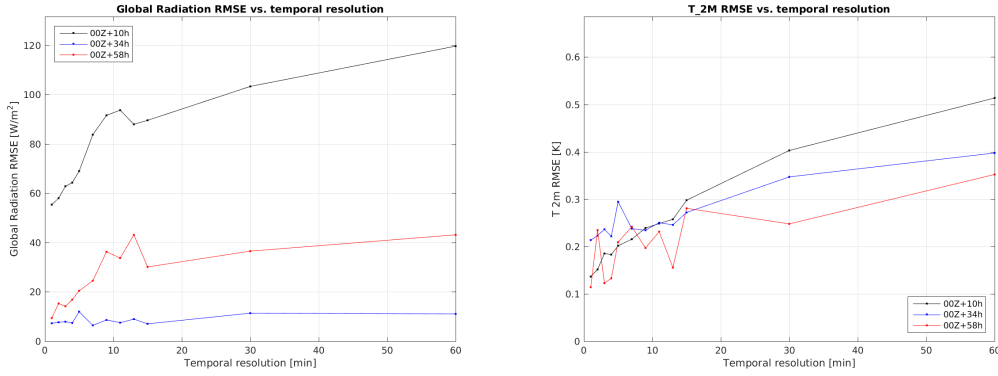
Figure 9: Domain average global radiation (left panel) and 2m temperature (right panel) biases (compared with a control run of full temporal resolution). Three lead times are presented: 10 hours (black), 34 hours (blue) and 58 hours (red). Results plotted as function of radiation call time temporal resolution. The black line represents the lead time with cloudy conditions and the blue line for clear skies conditions. The red line is intermediate conditions.

4.2 The Monte-Carlo Spectral Integration method

In an attempt to both reduce errors and to decrease the run-time we implemented a different approach which is to decrease the spectral resolution by a wise sampling technique, a method known as Monte Carlo Spectral Integration (MCSI). Many radiative transfer schemes and also COSMO RG92 scheme, uses the k-distribution method for the gases-radiation interaction calculations (Fu & Liou 1992). In this method the spectrum is transferred from wavelength space to cumulative probability space. This space is divided to intervals named *g-points*. In COSMO for each gas and for each spectral interval there are between two to eight g-points. In the operational mode of COSMO the Fast Exponential Sum Fitting Technique (FESFT) is used to fully calculate all of the mentioned g-points (Ritter & Geleyn 1992). In MCSI only one g-point is calculated in each time step according to its probability. In COSMO we used a softer version of MCSI where a g-point is selected in each of the spectral intervals which increases the computational cos but does neglect either of the spectral intervals in every time step. In the basic most expensive COSMO radiation scheme, the Exponential Sum Fitting Technique (ESFT), the fluxes calculation subroutines are called for each g-point which belong to the 8 COSMO bands and each of their combinations at each time step, a total of 301 times. In the FESFT, these subroutines are being called only 87 times for each of the g-points in the COSMO radiation scheme. This only are supposed to reduce the CPU effort by a factor of 3. If the radiation scheme is called every 15 minutes only (45 20-seconds time steps) as in the default setup, the runtime for radiation is ∼45 times faster. If the soft-MCSI method is used, only one g-point is selected for each spectral interval at each time step meaning only 8 times (∼ 37 times faster). But using this method needs much frequent call time than the default 15-minutes temporal resolution. Since the radiation is by definition miscalculated at each time step, but the frequent call to the radiation scheme cancels out the errors on the long run since the g-point selection was based on their probability weights. We found out the using the MCSI with full temporal resolution (calling the radiation scheme every time step) in COSMO-2.8km setup can increase runtime by 33% with only slight reduction of global radiation and 2-meter temperature biases compared to FESFT. But using MCSI with a 100 seconds temporal resolution (every 5 time steps) can give the same benefits but

with only 4% increase in runtime. In the upper panel of Fig. 10, the 2m Temperature RMSE of different setups for the same experiment as explained for Figs. 8 and 9 are plotted against the model runtime divided by the model runtime for the default scheme (FESFT with 15 minutes temporal resolution). The RMSE is calculated against a full radiation scheme calculation (ESFT for every model time step) which serves as the control run. We see that the RMSE decreases for the MCSI method (red dots) when the temporal resolution is increased but with the price of CPU runtime. One can clearly see that the default setup (magenta) gives law RMSE values but with minimum model runtime compared with other methods and temporal resolutions seems like the ideal setup as was correctly assumed by previous COSMO model experts. Using the default setup but with a course resolution spatial resolution gives a slightly larger RMSE and slightly reduced model runtime. The lower panel of Fig. 10 shows the T2m bias as function of model runtime differences. As expected the bias is very small for all MSCI experiments and steady even for lower temporal resolutions. Nevertheless, the default setup is at least comparable to the best MCSI set up with 100 seconds resolution but with better runtime.
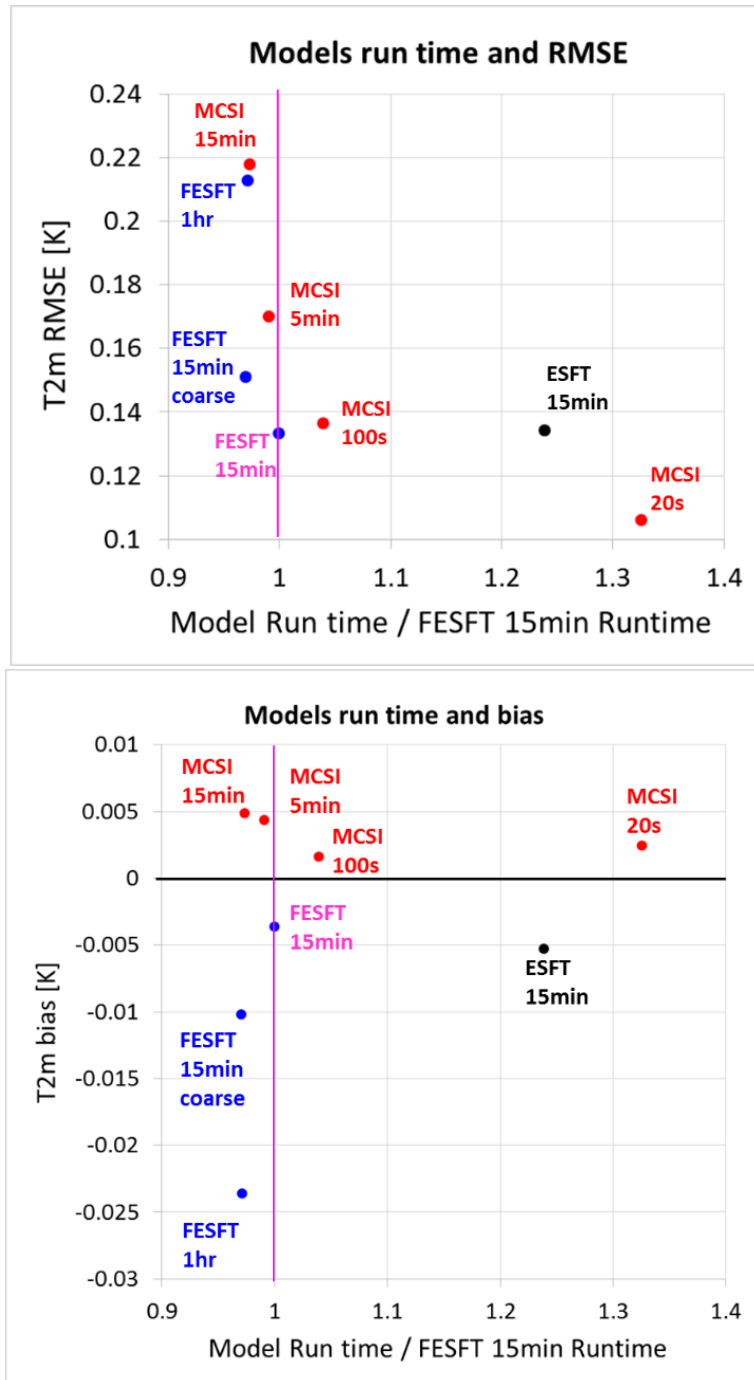
Figure 10: 2m-temperature domain average RMSE (upper panel) and bias (lower panel) compared with a control run of full temporal resolution using ESFT method (see text). The x-axis represents the model runtime compared with the default setup runtime (FESFT method with 15 minutes temporal resolution). Red dots is associated with MSCI method runs with different temporal resolutions, Blue dots represents the FESFT method run and black dot stands for the ESFT method.

4.3 Conclusions and recommendations

A new radiation solver for the scattering and absorption of the radiation by gases (H_2O, CO_2, O_3) was implemented. The new solver based on a soft version of the Monte-Carlo Spectral Integration, that was originally written by Bodo Ritter in a private version, is now fully implemented and tested in the official release of COSMO. To use it one should choose the name list parameter itype_mcsi = 1 with a recommended radiation temporal resolution of 100 seconds (i.e. for a model time step of 20 seconds one should set nincrad = 5). Still, the default scheme using itype_mcsi = 0 with a 15 minutes temporal resolution (nincrad = 45 for the previous example) is still the recommend setup for an ideal combination between performance and runtime. This recommendation is valid for the COSMO-2.8km setup. It is recommended to evaluate the MSCI option for different spatial resolutions (i.e. LES) or different applications like climate models.

5 New parametrization for vertical microphysical profiles in shallow cumulus

(P. Khain, H. Muskatel, U. Blahak)

5.1 Overview

Shallow convection is a sub-grid process in cloud-resolving models for which their grid-box is larger than the size of small cumulus clouds (Cu). At the same time such Cu substantially affect radiation properties and thermodynamic parameters of the low atmosphere. The main microphysical parameters used for calculation of radiative properties of Cu in cloud resolving models are liquid water content (LWC), effective droplet radius (r_e) and cloud fraction (CF). In this study, these parameters of fields of small warm Cu are calculated using large-eddy-simulations (LES). We performed it using the System for Atmospheric Modelling (SAM) with spectral bin microphysics. Despite the complexity of microphysical processes, two fundamental properties of Cu were found. First, is that despite of the high variability of LWC and droplet concentration (N_d) within clouds and between different clouds, the volume mean and effective radii per specific level vary only slightly; Second is that the values of r_e are close to those forming during adiabatic ascent of air parcels from cloud base. These findings allow characterizing a cloud field by a specific vertical profiles of r_e and of mean LWC, which can be calculated using the theoretical profile of adiabatic LWC and N_d at cloud base. Using the results of these LES, a simple parametrization of cloud-field averaged vertical profiles of r_e and of LWC is proposed for different aerosol and thermodynamic conditions. These profiles parametrization is implemented in COSMO to be used for calculation of radiation properties of subgrid Cu fields. For more details, the reader is referred to (Khain et al., 2019).

5.2 Theoretical background

5.2.1 Calculation of shallow cumulus LWC and R_e in NWP models

Large–scale models with grid spacing of tens of kilometres do not resolve clouds and require the use of convective parametrization schemes. The values of r_e and LWC that are usually prescribed in such models, inevitably leads to errors in calculation of related quantities.

The treatment of clouds in meso-scale cloud-resolving models (CRM) with grid spacing of a few kilometres is complicated since only the largest, grid scale, clouds are resolved in such models. Small clouds and especially shallow warm Cu, with a typical size smaller or similar to the grid spacing of CRM remain a sub-grid phenomena.

In CRM calculations of effective drop radii at resolvable scales are performed when the relative humidity (RH) in the grid point exceeds 100%. When the grid spacing is larger than the size of shallow Cu, the conditions for small clouds formation can be suitable even when the calculated mean grid relative humidity (RH) is lower than 100%. These clouds may, however, affect the radiative budget substantially, and the knowledge on r_e, LWC and CF values is necessary for such calculations.

In the limited area NWP r_e of unresolved clouds is a tuning parameter. For instance, in COSMO r_e=5 μm by default. Since on average over the grid box there is sub-saturation, the LWC in these shallow cumuli is crudely parametrized as a function of temperature (reduces with a decrease in temperature), mimicking the reduction of available water vapour for condensation with height. Recently, a new cloud radiation scheme was developed for COSMO (Blahak and Ritter, 2013), and is currently under evaluation. Among other developments, r_e of unresolved clouds is calculated in this scheme from the ratio of LWC and N_d. While LWC is evaluated using the parametrization described above, N_d is determined using the assumed aerosol concentration and the effective (unresolved) vertical velocity at cloud base. The large uncertainty in LWC causes r_e to be highly uncertain as well. As a result, such parametrizations may lead to significant errors in evaluation of effects of shallow convection on radiation and on other thermodynamic atmospheric properties.

5.2.2 Utilization of LES for simulation of small Cu

Large Eddy Simulations (LES) is an efficient method to simulate fields of small Cu and investigate Cu dynamics and microphysics, or to develop new parametrizations for those. To simulate cloud microphysical processes we use the detailed microphysical approach of the bin microphysics, which solves the microphysical equations for determining the droplet size distributions (DSD). In LES simulations the bin-microphysical approach is often used for investigation of thermodynamic factors and aerosols on the parameters of droplet size distributions, drizzle formation and on cloud dynamics (e.g., Jiang et al., 2008). Such parameters as LWC, N_d and r_e are determined directly from the calculated DSD. In addition to simulation of cloud fields, LES are used to develop parametrization schemes for the large scale models. In the present study we use LES results to investigate the behaviour of microphysical properties of non-precipitating and slightly precipitating shallow Cu fields under different aerosol conditions. The goal of the study is twofold. First, we will check the variability of r_e in clouds of different sizes and the robustness of utilization of one mean vertical profile of $\overline{r_e}(z)$ to characterize all the clouds within the field. We explore the reasons for the comparatively low horizontal variability of r_e despite of the high variability of LWC both within each cloud and between different clouds. Second, using the results of the LES we propose a simple parametrization of the mean vertical profiles of r_e and LWC that uses adiabatic LWC profile and N_d at cloud base. This parametrization is implemented in COSMO model to be used for calculation of radiation properties of subgrid Cu fields.

5.3 LES set-up

In this study LES were performed using System for Atmospheric Modelling (SAM) (Khairout-dinov and Randall, 2003) with Spectral Bin Microphysics (SBM, Khain at al. 2004, 2013) (for

details see: http://rossby.msrc.sunysb.edu/~marat/SAM.html). SAM is a non-hydrostatic, inelastic model with cyclic boundary conditions in the horizontal direction. The SBM is based on solving kinetic equations for size distribution functions of water drops and Aerosol Particles (AP). Aerosols and droplet size distribution functions are defined on the doubling mass grids containing 33 bins. The drops radii range between 2 μm and 3.2 mm. The size of AP serving as cloud condensation nuclei (CCN) ranges between 0.005 μm and 2 μm. Using the values of supersaturation with respect to water, the critical CCN radius is calculated (using the Köhler theory) and APs larger than the critical size are nucleated to droplets as described by Khain et. al (2000). The rest of APs are advected with air motion. Diffusional growth and evaporation of droplets are calculated basing on the changes in the supersaturation during a model time step. The time steps are chosen to be smaller than drop relaxation time. This is the physical condition of accurate calculation of diffusion growth/evaporation. Collision-coalescence is solved by the stochastic collision equation using the accurate method of Bott (1998). The collision kernels were calculated using an exact method described by Pinsky et al. (2001). Drop sedimentation is calculated using fall velocities determined by Beard (1976). Fields of small trade Cu were simulated within a domain of 12.8 km x 12.8 km x 5.1 km using horizontal resolution of 100 m, and vertical resolution of 40 m with a dynamical time step of 1 s. As a case study, small Cu observed during BOMEX were chosen for simulation (Siebesma et al., 2003). The vertical profiles of temperature and dew point used in simulations are shown in Fig. 11. The original BOMEX profile is that with the inversion at 1500m, the other two profiles with the inversions at 1000 m and 2000 m were used for analysing the effect of the inversion height on the microphysical properties of simulated cloud fields.
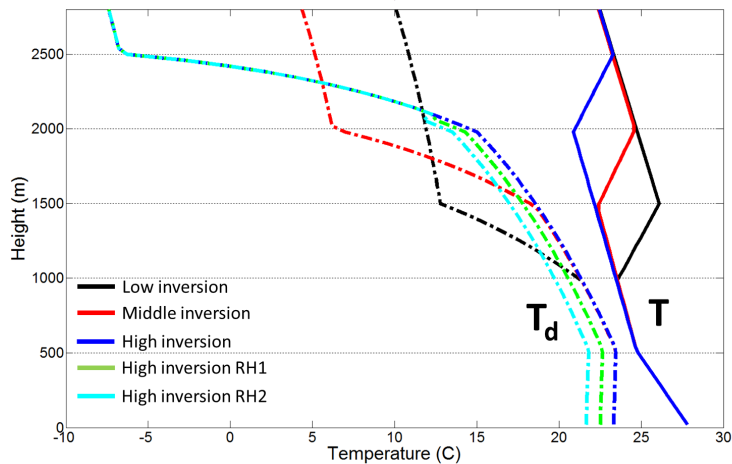
Figure 11: Initial vertical profiles of temperature (solid) and dew point (dashed) used in simulations: low inversion at 1000 m (black), high inversion at 2000 m (blue), middle inversion at 1500 m (red- the original BOMEX profile). Green and cyan profiles denote sensitivity tests with decreased relative humidity (by 5% and 10%, respectively) with respect to high inversion profile.

In the simulations we used concentrations of CN within the range from 500 cm^{-3} to 5000 cm^{-3} which lead to mean N_d at cloud base of $\sim 50\ cm^{-3}$ to $\sim 500\ cm^{-3}$. According to the accepted definition, this range of N_d includes three cloud types: clean (maritime), intermediate (clean continental) and polluted (continental) (Ghan et al. 2011). Note that comparatively small mean cloud N_d at cloud base at such CN concentration is determined by low vertical velocities at cloud base and by prescribed initial CN size distributions containing large fraction of

small CN, which cannot be activated at such vertical velocities. We do not consider clouds developing in the extremely clean atmosphere, and producing drizzle immediately after their formation. We will refer the simulations according to the CN concentration and inversion height: H-high, M-medium and L-low, e.g. E5000H, where E denotes "experiment" and 5000 shows CCN concentration. The list of simulations is presented in Table 2.

Name of experiment	Height of inversion (m)	Aerosol concentration (cm^{-3})	Main results				
			total CF (%)	STD of total CF (%)	$<N_d>$ (cm^{-3})	$<CWC>$ max (gm^{-3})	$<r_e>$ max (μm)
E5000L	1000	5000	20.1	1.8	403	0.52	7.7
E5000M	1500	5000	17.9	1.0	371	0.54	8.2
E5000H	2000	5000	19.7	1.6	372	0.47	8.4
E3000L	1000	3000	20.5	1.6	248	0.58	9.4
E3000M	1500	3000	18.7	1.7	222	0.52	9.8
E3000H	2000	3000	20.4	1.7	221	0.47	10.2
E2000L	1000	2000	20.8	1.1	164	0.58	10.7
E2000M	1500	2000	18.8	1.1	149	0.51	11.3
E2000H	2000	2000	20.6	1.5	148	0.48	12
E1000L	1000	1000	21.9	1.0	81	0.55	13.6
E1000M	1500	1000	19.4	1.3	82	0.49	14.9
E1000H	2000	1000	21.7	1.6	83	0.42	15.5
E500L	1000	500	24.2	1.8	47	0.43	16.7
E500M	1500	500	21.5	1.3	49	0.37	18.2
E500H	2000	500	23.1	1.8	48	0.32	18.3

Table 2: List of simulations. Notations: "total CF" – time averaged total cloud fraction, "STD of total CF" – standard deviation of total CF, "$<N_d>$" – time and space averaged N_d, "$<CWC>$ max" – maximum (over height) value of the mean profile of CWC, "$<r_e>$ max" – maximum (over height) value of the mean profile of r_e.

In addition to simulations listed in Table 2 three supplemental simulations were performed. The simulation E2000H-50 is similar to E2000H but has horizontal grid spacing of 50 m. It was performed to analyse effects of model resolution on cloud thermodynamics and microphysics. Two other simulations E2000H-RH1 and E2000H-RH2 have air relative humidity within the layer from the surface to the inversion base by 5% and 10% lower than in E2000H, respectively. The profiles of Td(z) in these simulations are shown in Fig. 11. These simulations aim to investigate effects of environment humidity on cloud properties and to check universality of the parametrization proposed (see below) under different thermodynamic characteristics of the boundary layer. Convection is triggered by random temperature perturbations at the beginning of the simulations. For isolating the aerosol effect on the thermodynamic conditions, the radiative effects (as included in the large scale forcing) as well as the surface fluxes were prescribed in all simulations (see Dagan et al., 2016 for detail). The surface fluxes and the large scale forcing of BOMEX have been used for this study following Siebesma et al. (2003). All simulations were performed for 8.3 hours.

5.4   Results

In order to give an idea of how the cloud field simulated by SAM looks like which can simplify further interpretation of the results, we present in Fig. 12 3D snapshots of the LWC, Nd and r_e in E5000H. In this particular case rain water content is negligible, so LWC is equal to cloud water content (CWC), determined by cloud droplets with radii below 25 μm. This is the approximate maximum drop radius that can be reached by diffusion growth and non-intense collisions between small cloud droplets (Pinsky and Khain, 2002). The cloud field consists of clouds of different sizes and shapes. The smallest clouds rapidly evaporate by mixing with surrounding, while few largest clouds penetrate the inversion layer. The largest clouds contain cores with high CWC. As expected, the CWC increases with height, reaching its maximum near the cloud top, while Nd is nearly constant with height. Hence, the drop size r_e is increasing with height, as can be seen in Fig. 12c. It is possible to see that r_e changes in horizontal direction within the range 9-11 μm in the upper parts of clouds, i.e. the relative changes of r_e are much lower than those of CWC and N_d.
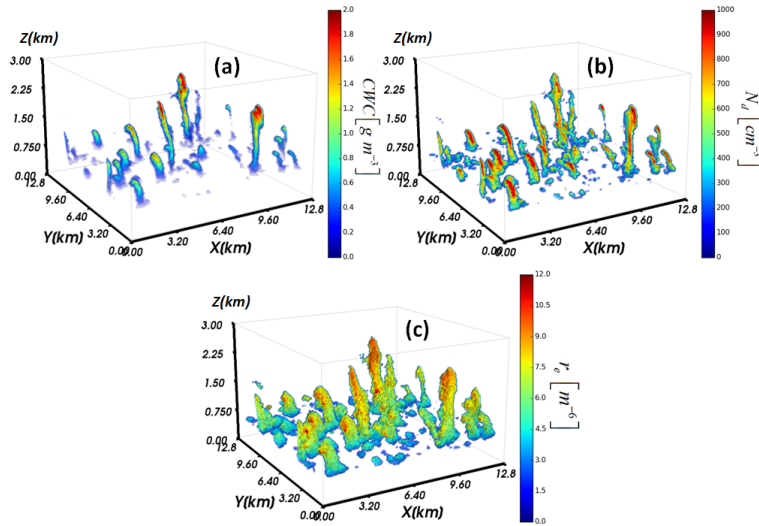
Figure 12: A snapshot of (a) CWC, (b) N_d, and (c) r_e fields for E5000H experiment: inversion is at 2 km, the CN concentration is 5000 cm^{-3}, t = 208 min. The impression of "noodle" shape clouds and not the usual "cotton balls" shape, are just due to the difference between the horizontal and vertical scales.

For more details regarding the performed simulation results the reader is referred to Khain et al., 2019. Here we continue with analysing r_e profile. The volume mean (r_v) and effective droplet (r_e) radii are among the most important microphysical characteristics of clouds. In several studies the mean volume and effective radii are related as $r_e \approx k r_v$. According to our simulations $k \approx 1.15 - 1.17$. The lowest values of coefficient k take place for polluted clouds in which DSD are the narrowest. Accordingly, the largest values of k take place for clean clouds, where DSD width is largest, and the existence of large cloud droplets increases r_e. Main properties of r_e in cloud field of small Cu can be derived from Fig. 13 showing height vs. re scattering diagrams for selected simulations with different inversion layer heights and different aerosol concentrations. These simulations reflect the basic properties of r_e. Purple lines in Fig. 13 denote the profiles of "adiabatic" effective radius of cloud droplets r_{e_ad}, which could be observed in adiabatically ascending cloud volume with droplet concentration N_{d_ad} calculated at cloud base. In Fig. 13 r_{e_ad} is calculated as:

$$r_{e\_ad}(z) = 1.15 \cdot r_v = 1.15 \cdot \left(\frac{LWC_{ad}(z)}{\frac{4}{3}\pi\rho_w N_{d\_ad}} \right)^{1/3} \tag{15}$$

where $LWC_{ad}(z)$ is adiabatic LWC that can be calculated as described, for example, by Pontikis (1996) or Pinsky et al. (2012). The adiabatic cloud number concentration N_{d_ad} is the concentration in an adiabatic cloud core. The cloud cores are adiabatic only at the first few hundreds of meters above the cloud base. Hence, in these levels $r_e(z)$ in the cloud cores should be equal to $r_{e\_ad}(z)$. We have chosen N_{d_ad} so that $r_{e\_ad}(z)$ will nearly coincide with $r_e(z)$ in the cloud cores. N_{d_ad} can be calculated in large scale models using, for instance, lookup tables as a function of aerosol concentration and cloud base vertical velocities (Segal and Khain, 2006) as it is done in COSMO, theoretical formulas (Pinsky et al. 2012) or other approaches (Ghan et al. 2011). The cloud base vertical velocities in the COSMO model are calculated as a sum of gridscale updraft, vertical component of turbulent fluctuations using turbulent kinetic energy (with isotropy assumption), radiative cooling effect (Khvorostyanov and Curry, 1999), and the convective velocity scale (Deardorff, 1970). Because of some uncertainties in evaluation of N_{d_ad}, we will refer r_{e_ad} to as "modelled" adiabatic effective radius. Although the Nd and LWC in cloud cores become smaller with height compared to N_{d_ad} and LWC_{ad}, but r_{e_ad} still represents well the effective radius in cloud cores. The advantage of r_{e_ad} is that it can be calculated in any model knowing the LCL (together with the cloud base temperature and pressure) and N_d at cloud base.
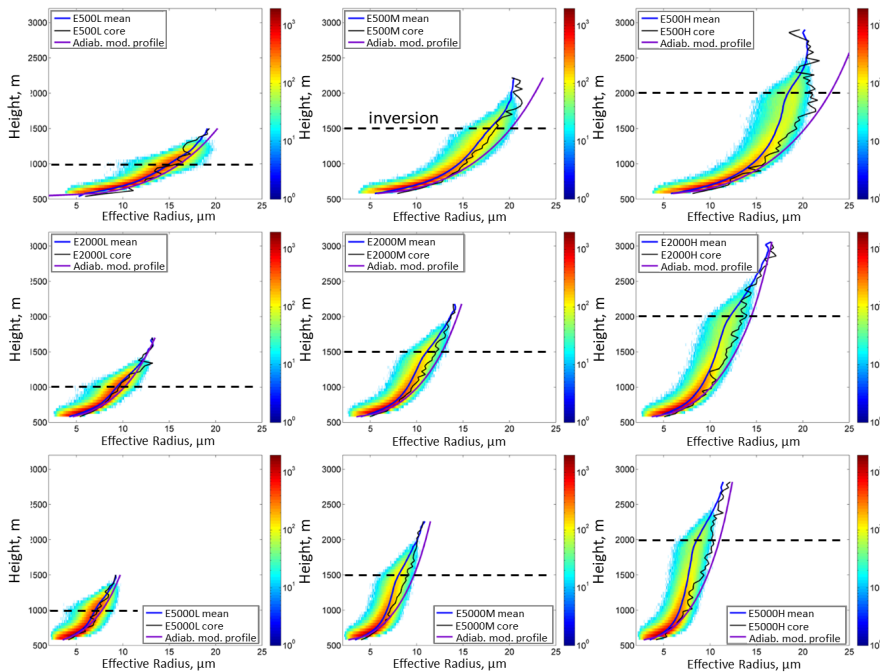
Figure 13: The height-r_e scattering diagrams for simulations with different CN concentrations. Left, middle and right columns show the cases with low (base at 1000m), middle (base at 1500m) and high (base at 2000m) inversion, respectively. Notations: The colour-scale reflects the number of cloudy grid points with specific r_e in logarithmic scale; black curves denote effective radii in clouds cores; purple curves denote the modelled approximation to adiabatic r_e profiles; blue curves denote profiles of horizontally averaged r_e; black dashed lines denote the inversion base heights.

An analysis of Fig. 13 shows several important features of r_e in clouds forming in cloud fields:

a. Strong effect of aerosols

A well-known effect is the faster r_e growth with height in case of low CCN concentrations. In case of clean environment, N_d is small, therefore the fewer droplets that form near cloud base have little competition on the available supersaturation (S_W) (Pinsky et al. 2012, 2014; Dagan et al. 2016). As a result, S_W remains relatively high and the droplets grow rapidly with height. At CN concentration of 5000 cm^{-3}, the maximum of the r_e remains below 13-15 μm, so these clouds do not produce neither raindrops nor drizzle. At CN concentration of 2000 cm^{-3}, the maximum r_e reaches 14-15 μm at z = 2000 m and light drizzle arises above this level (not shown here). In E500 the maximum of r_e exceeds 15 μm and raindrops arise (not shown here).

b. Low horizontal variability of effective radius

A fundamental property of r_e is low horizontal variability. This variability is much lower than that of LWC. Generally, the averaged (over all heights) relative variability varies between 10-15%. Our results show low variability of r_e. We partially attribute this insensitivity to the following. The mean volume radius is proportional to $(LWC/N_d)^{1/3}$. As the incloud nucleation leads to the formation of the smallest droplets, the LWC is defined by the first mode of droplets activated at cloud base. Because of the 1/3 power, the in-cloud nucleation cannot change N_d strongly enough to significantly affect the mean volume radius (as well as r_e). Low variability of r_e indicates that cloud field can be characterized by robust vertical profile of r_e that is close to the adiabatic one and depends on the aerosol loading.

c. The maximum effective radius is in cloud interior

The important feature is that the r_e is maximal in cloud interior (black lines), where LWC are maximum. In cloud cores the profiles of $r_e(z)$ almost coincide with the adiabatic values (purple lines) calculated according Eq. 15. This fact shows that cloud droplets reach maximum size in cloud cores, together with the maximum LWC and the maximum N_d.

d. Limiting value in case of raindrop formation

As seen in Fig. 13, r_e in cloud core in simulations with $CN = 500\ cm^{-3}$ is maximum in cloud cores and close to the adiabatic value. Formation of raindrops is seen by termination of the r_e growth with height. In case of rain drop formation, r_e determined within the range of cloud droplet radii ($< 25\ \mu m$) does not exceed about 22 μm and remains height independent (Figure 5.3, E500H). Such regime is known as rainout (Rosenfeld and Lensky, 1998). The reason of low dependence of r_e on height in case of raindrop formation is that raindrops collect cloud droplets of all sizes that leads to decrease in N_d, but does not change r_e of the cloud droplet mode.

According to the results, in case of rain formation, the maximum r_e of cloud droplets can be calculated as:

$$r_{e_{max}} = \min(22\mu m, r_{e\_ad}) \tag{16}$$

Because of low variability of r_e, the values of r_e are concentrated around $\overline{r_e}$ which is slightly smaller than r_{e_ad}. The physical reasons of low variability of r_e were analysed by Pinsky et al. (2016b), Pinsky and Khain (2018a) and by Magaritz-Ronen et al. (2016b). Relative humidity in cloudy volumes, even well diluted ones, remains high which does not allow r_e to decrease anyhow significantly. Small decrease in r_e reflects the contribution of air volumes

newly penetrating clouds and located near cloud edges. In such volumes partial evaporation of drops penetrating from cloudy volumes leads to formation of DSD with lower effective radii. Rapid increase of relative humidity in such volumes with time leads to termination of evaporation of largest droplets penetrating from the cloudy volumes. As a result, the r_e in the volumes penetrating clouds rapidly reaches values typical of cloudy volumes, while LWC and N_d remain much lower than in the cloud core. The mixing with humid air, which entrains clouds, does not cause strong changes in drop sizes near cloud edge.

5.5 Parametrization of microphysical parameters of cloud ensembles

For practical goals, it is desirable to characterize cloud field by some mean vertical profile $\overline{r_e}(z)$. Analysis of results presented in Fig. 13 shows that $\overline{r_e}(z)$ is smaller than the maximum value $r_{e\_ad}(z)$ only by $\sim$10-15%. The difference between $\overline{r_e}(z)$ and $r_{e\_ad}(z)$ reaches its maximum at the inversion base level. This increase is related to the fact that cloud ensemble contains clouds of different size and clouds of lower width experience stronger effects of mixing because the interface zone affected by mixing in such clouds occupies a significant fraction of the cloud volume. Above the base of inversion the difference $r_{e\_ad}(z)$-$\overline{r_e}(z)$ decreases again, since only largest clouds remain. This behaviour retards a simple approximation of $\overline{r_e}(z)$ via $r_{e\_ad}(z)$. We will approximate dependence between these two quantities (as well as other approximation of averaged values) ignoring the upper part of clouds within inversion layer, for which the contribution to the optical depth of cloud layer is less than 5% (not shown). Within the layer below inversion base the cloud averaged r_e can be approximated as

$$\overline{r_e}(z) = \alpha(z) r_{e\_ad}(z) \tag{17}$$

$$\alpha(z) = 0.95 - 1.2 \cdot 10^{-4}(z - z_{cb}) \tag{18}$$

Where z is in meters, z_{cb} is the cloud base level, determined by the minimal distance from the surface where supersaturation for the first time becomes positive and droplet nucleation takes place. In order to take into account the effect of raindrops, the values of $r_{e_{ad}}(z)$ in Eq. 17 were replaced by $r_{e,max}(z)$ calculated using Eq. 16. Vertical profiles of the cloud averaged r_e are calculated directly from LES and parametrized using Eqs. 15-17 are shown in Fig. 14.

Figure 14: Vertical profiles of the cloud averaged r_e calculated directly from LES (solid lines) and parametrized using Eqs. 15-17 (dashed lines). Each panel is plotted for different inversion base height: low, medium and high, respectively.

One can see a good agreement of parametrized $\overline{r_e}(z)$ with those calculated directly in the LES within entire range of aerosol loadings and different levels of the inversion. The standard deviation is of 0.39 μm.

The next step is the parametrization of the mean droplet concentration as a function of N_d at cloud base. N_d, as was mentioned above, can be determined using different approaches in different kinds of atmospheric models, including NWP models. The concentration at cloud base can be referred to as adiabatic concentration N_{d_ad}, which being formed at cloud base does not change with height within ascending adiabatic parcels. In small Cu the changes of air density with height are small. Profiles of $\overline{N_d}(z)$ depend on whether clouds produce raindrops or not. In case of non-precipitating clouds $\overline{N_d}(z)$ and N_{d_ad} are equal to the maximum value N_{d_max}, which can be considered as constant with height. Analysis (not shown here) shows that the maximum N_d in clouds producing raindrops can be approximated as a constant till the level at which $r_{e\_ad} = 12\ \mu m$ and linearly decreasing above this level. Statistical analysis shows that the profile of maximal N_d can be written in the form

$$N_{d\_max}(z) = \begin{cases} N_{d\_ad}, & z < z_{12}\ , where\ r_{e\_ad} = 12\ \mu m \\ N_{d\_ad}\left[1 - \gamma\left(z - z_{12}\right)\right], & z > z_{12} \end{cases} \tag{19}$$

where $\gamma = 0.45 m^{-1}$ and z is in meters.

$$\overline{N_d}(z) \approx \beta N_{d\_max}(z) \tag{20}$$

where on average (over all heights and simulations) $\beta = 0.38$ with standard deviation of 0.03. The parameters in expressions 17-19 are obtained minimizing the root mean square over all the simulations. Expressions 18 and 19 allow to calculate the averaged concentration profiles using N_d at cloud base and the height of the level where $r_{e_{ad}}$ reaches the precipitating threshold. Fig. 15 shows profiles of cloud averaged N_d obtained in LES and using expressions 19 and 20. One can see a good agreement between the approximations and profiles directly calculated using LES.
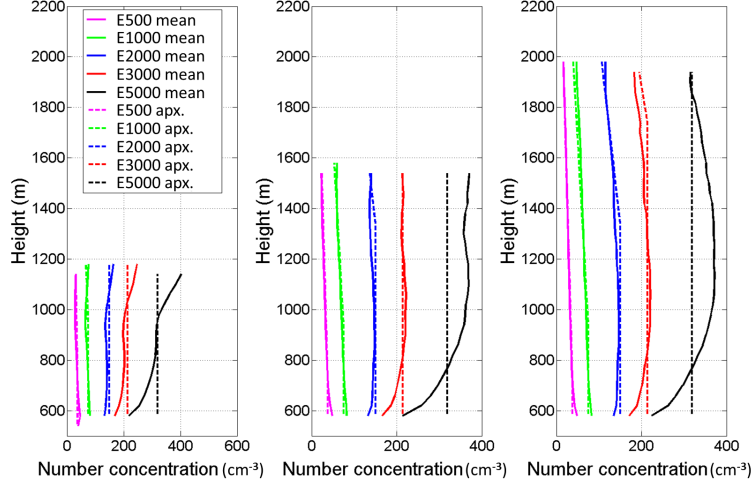
Figure 15: Profiles of cloud averaged N_d obtained in LES (solid lines) and using expressions 18 and 19 (dashed lines). Each panel is plotted for different inversion base height: low, medium and high, respectively.

In addition to $\overline{r_e}(z)$, the parametrizations of radiation transfer through unresolved cloudiness in many NWP and climatic models require a prognostic calculation of $\overline{LWC}(z)$. As mentioned in the introduction, the $\overline{LWC}(z)$ of unresolved clouds in the default version of the COSMO model is crudely parametrized as a function of the temperature. Now, using the parametrization of $\overline{r_e}(z)$ and $\overline{N_d}(z)$ as mentioned above, we are able to parametrize $\overline{LWC}(z)$ as well. Strictly speaking, the practically required values of $\overline{LWC}(z)$ should be determined as:

$$\overline{LWC}\,(z) = \overline{\frac{4}{3}\pi\rho_w N_d(z) r_v^{\;3}(z)} = \overline{\frac{4}{3}\pi\rho_w N_d(z)\left(\frac{r_e(z)}{1.15}\right)^3} \qquad (21)$$

However, since variability of r_e is low, the last equality can be rewritten as:

$$\overline{LWC}\,(z) \approx \frac{4}{3}\pi\rho_w \overline{N_d}(z)\left(\frac{\overline{r_e}(z)}{1.15}\right)^3 \qquad (22)$$

which is substantially simpler than Eq. 21. Fig. 16 presents the vertical profiles of $\overline{LWC}(z)$ calculated directly from the results of the LES simulations and the profiles of $\overline{LWC}(z)$ calculated using Eq. 22.

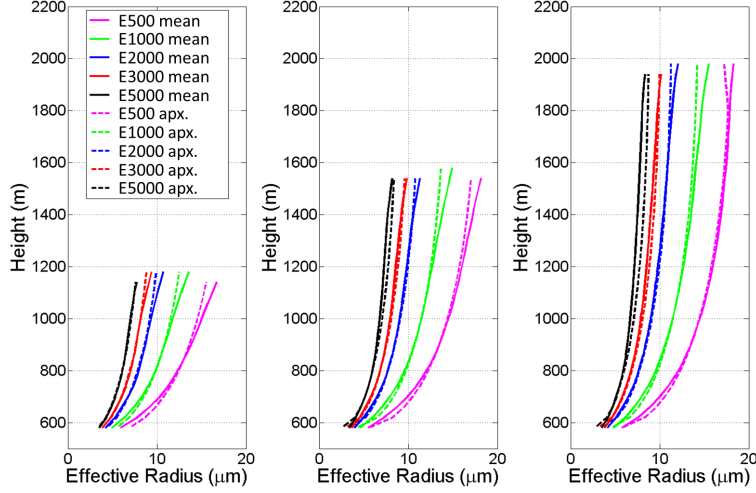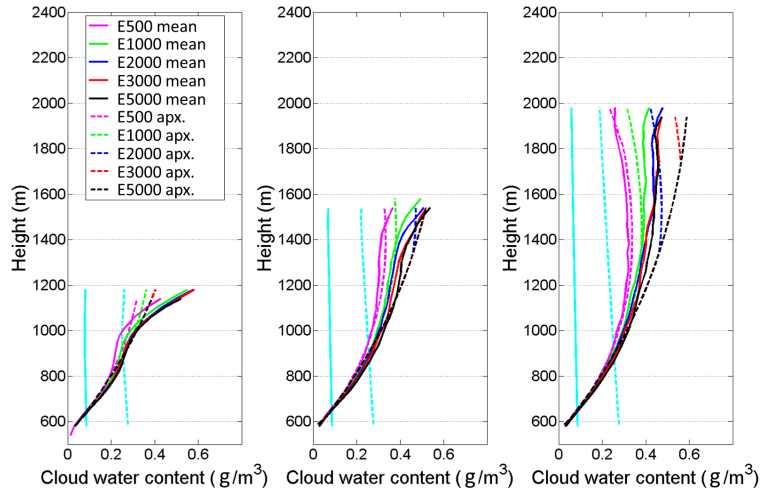Figure 16: Vertical profiles of the cloud averaged CWC calculated directly from LES (solid lines) and approximation (Eq. 22) (dashed lines) for different aerosol loadings and for different inversion levels: low (left), medium (middle) and high (right). Cyan solid and dashed lines indicate the profiles obtained using different options within the default parametrization in COSMO.

One can see that Eq. 22 allows reproducing the LES profiles of $\overline{CWC}(z)$ quite accurately, especially in comparison with COSMO approximations (cyan solid and dashed lines). Deviations of CWC calculated using Eq. 22 from that calculated directly in LES seen at higher levels are not of high importance for calculation of radiation fluxes because CF of these clouds at such altitudes are low.

5.6 Implementation of the parametrization in the COSMO model

The new parametrization for $\overline{LWC}(z)$ and $\overline{r_e}(z)$ was implemented in COSMO for calculation of the optical properties of subgrid shallow cumulus. The main logical switch for activating the parametrization is luse_qc_adiab_for_reffc_sgs. Additional logical switch luse_qc_con_sgs allows calculating the subgrid scale LWC of shallow cumulus using either $\overline{LWC}(z)$ parametrization or the LWC(z) derived from the shallow convection parametrization (lconv = T). alpha1_adiab_rad and alpha1_adiab_rad parameters describe $\overline{r_e}(z)$ above cloud base z_{cb} according: $alpha1_{adiab_{rad}} - alpha2_{adiab_{rad}} * (z - z_{cb})$. The parameter beta_adiab_rad describes the ratio of cloud-average N_d of SGS shallow convection with respect to the cloud core value obtained by the Segal-Khain parametrization. The parameter gamma_adiab_rad describes the linear deviation with height ($r_e > 12 \ \mu m$ level) of SGS shallow convection LWC from the "pseudo-adiabatic" value. The list of parameters of the new parametrization is presented in Fig. 17. It includes the meaning of each parameter, its type, default value, available range and recommended value.

Parameter	Meaning	Type	Def	Range	Recom
luse_qc_adiab_for_reffc_sgs	Use "adiabatic" parametrization for SGS shallow convection effective radius	LOG	F	T/F	T
luse_qc_con_sgs	Effective if luse_qc_adiab_for_reffc_sgs=F: use "adiabatic" parametrization for SGS shallow convection LWC. T: use LWC from shallow convection parametrization (if lconv=T)	LOG	F	T/F	T
alpha1_adiab_rad	Linear deviation with height (above cloud base) of SGS shallow convection effective radius from the adiabatic value alpha1_adiab_rad-alpha2_adiab_rad*(z-zcb). [-]	REAL	0.95	[0.7-1]	0.95
alpha2_adiab_rad	Linear deviation with height (above cloud base) of SGS shallow convection effective radius from the adiabatic value alpha1_adiab_rad-alpha2_adiab_rad*(z-zcb). [1/m]	REAL	1.2 E-4	[1-2] E-4	1.2 E-4
beta_adiab_rad	Ratio of cloud-average number concentration (of SGS shallow convection) with respect to the cloud core value (obtained from Segal-Khain)	REAL	0.38	[0.2-1]	0.38
gamma_adiab_rad	Linear deviation with height (above reff=12micron level) of SGS shallow conv. qc from the "pseudo-adiabatic" value. [1/km]	REAL	0.45	[0.2-0.7]	0.45

Figure 17: List of parameters of the new adiabatic parametrization for LWC and r_e in shallow cumulus. The Table includes the meaning of each parameter, its type, default value, available range and recommended value.

6 New shallow convection shutdown scheme

(P. Khain)

6.1 Overview

Global Numerical Weather Prediction (NWP) models use convection parametrization to describe both deep and shallow convection. Convection permitting models with grid spacing below ∼4 km usually describe deep convection on grid scale, but still parametrize the shallow convection, being sub-grid scale process. Many of these parametrizations are based on the mass-flux approach. The artificial combination of resolved and parametrized convection often negatively influences the model forecast skill and particularly precipitation. In this task we used COSMO 2.5 km resolution over the Eastern Mediterranean region to analyse the effect of the mass-flux shallow convection parametrization (SCP) on model forecasts. We show that SCP entrainment rate as well as restrictions on the shallow convection development height and maximum updraft speed have crucial effect on the forecasts of precipitation, temperature and moisture. Physically motivated tuning of these parameters can improve the model forecasts significantly. Finally, we estimate the climatic zones and seasons where SCP is expected to be particularly important for NWP.

6.2 COSMO shallow convection parametrization

COSMO mass flux Tiedtke type SCP (Tiedtke, 1989) calculates the grid scale feedback of subgrid-scale vertical fluxes of mass, heat, moisture and momentum in updrafts. The convective-scale eddy transports of dry static energy, moisture and momentum from cumulus updrafts are not described in terms of contributions from the individual ensemble components, but are represented by their average values using a one dimensional bulk cloud

model after Yanai et al. (1973). The updraft of the cloud ensemble is assumed to be in steady state, and the budget equations for mass, heat, moisture and momentum for the ascending air (the "updraft equations") are integrated. For their integration the possibility for shallow convection at a grid point is diagnosed. At the first model level above the surface an air parcel is defined with the grid-scale values of temperature (plus a small excess value representing subgrid scale perturbation), specific humidity and horizontal momentum. Lifting the parcel adiabatically allows to compute its condensation level. This level defines the cloud base or the level of free convection, if the parcel becomes buoyant with respect to the environment. The parcels values of temperature, mixing ratio, water content, and horizontal wind components at cloud base are then used as boundary conditions to integrate the updraft equations. In the updraft, entrainment is assumed to occur via turbulent exchange of mass and is parametrized as proportional to the updraft mass flux with a proportionality constant $entr_{sc}$. This constant is treated as a tuning parameter in the model with a default value of 0.0003 m^{-1}. The vertical integration of the updraft equations from cloud base to cloud top, where the parcel is no more buoyant, yields the values of the variables within the updraft. These values are then used to calculate the convective tendencies in the prognostic equations for the grid-scale variables of dry static energy (related to temperature), specific humidity and the horizontal wind components. During the ascent, the supersaturated parcel is assumed to condensate all the excess water vapour immediately. Since it is assumed that SCP should not produce precipitation, the resulting liquid water content is neglected by the model in autoconversion and other microphysical processes. This assumption may lead to an underestimation of light precipitation in the model. Besides, subgrid-scale vertical mixing by SCP tends to stabilize the CBL and thus to postpone or even cancel potential grid scale updrafts which produce precipitation. These drawbacks led to the necessity to limit the SCP in the model by turning it off. I.e. cancelling the subgrid-scale vertical mixing, in cases when the test parcel described above remains buoyant and rises too high in the atmosphere. Therefore, a second tuning parameter $thick_{sc}$ was introduced with a default value is 25000 Pa. This is the maximal pressure difference between the top and the bottom of the convection, and for higher values the scheme is turned off.

Fig. 18 schematically shows the typical options occurring at the model time step in SCP in case the test parcel is buoyant at the cloud base. In case 1 the entrainment $entr_{sc}$ is chosen to be high, causing the parcel to stop being buoyant (top of the convection) already at level k2. In case 2 $entr_{sc}$ is chosen to be lower, and the convection top occurs at level k3. In case 3 the parcel remains buoyant till the level k4 and the resulting convection vertical extent exceeds the threshold $thick_{sc}$. At that time step the SCP is turned off in the entire grid column, keeping the unstable profile unmixed and allowing grid scale updrafts to develop. In case 4 the SCP is turned off while the grid scale updrafts lead to grid scale supersaturation and activation of in-cloud microphysical processes and precipitation. This schematic picture shows that $thick_{sc}$ may have an influence in weakly unstable conditions, or unstable ones topped by an inversion. On contrast, during the peaks of the cyclones passage, the instability usually extends up to height of several kilometres. In these situations SCP is turned off and one would not expect any influence of $thick_{sc}$.
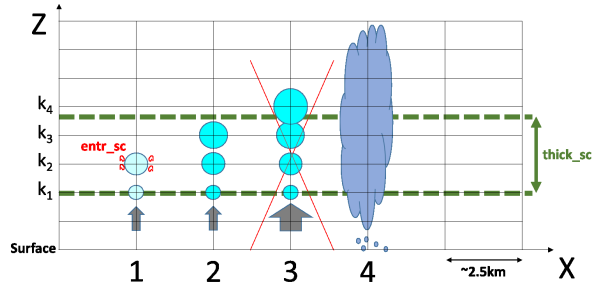
Figure 18: Schematic description of COSMO SCP. Case 1: $entr_{sc}$ is high, the top of the convection is at level k2. Case 2: $entr_{sc}$ is lower, the convection top occurs at level k3. Case 3: the convection vertical extent exceeds the threshold $thick_{sc}$. At that time step the SCP is turned off in the entire grid column. Case 4: the SCP is turned off, grid scale updrafts lead to grid scale supersaturation and activation of in-cloud microphysical processes and precipitation.

6.3 The effect of shallow convection parametrization on model forecast

At this section, cyclonic test case is used to explain the influence of the SCP on forecasts of precipitation. The selected test case occurred between December 30, 2015 and 2nd of January, 2016. Fig. 19 presents the synoptic situation over the EM during these days using mean sea level pressure (MSLP) and geopotential height at 500 hPa from IFS analyses. One can see that the 500 hPa geopotential height over central Israel gradually drops from ∼5600 to ∼5500 m and then climbs back towards ∼5580 m.

35
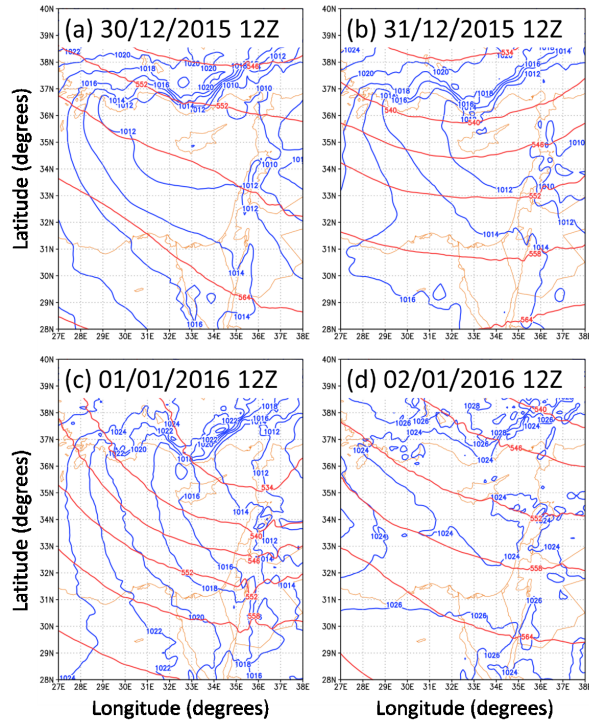
Figure 19: Cyclonic test case occurred during 30/12/2015-02/01/2016. The panels a-d show the IFS analyses of the mean sea-level pressure contours (blue lines) and the geopotential height (divided by 10) contours (red lines) for noon times (12Z) during the period.

It is a typical example of extratropical cyclones - the Cyprus Lows, which are responsible for most of the annual rainfall over the EM (Sharon and Kutiel, 1986; Alpert et al., 1990; Shay-El and Alpert, 1991; Ziv et al., 2006). The rain is formed within cold air masses of European origin that enter the region from the north-west. While moving over warmer Mediterranean waters, the air masses gain moisture and become conditionally unstable. The dynamics associated with the cyclone itself, together with that implied by the intersection of the westerly flow with the shoreline and, later on, with the mountain ridges, results in intensive rainfall over the Levant (Sharon and Kutiel, 1986). The concurrent upper-level system consists of a pronounced trough extending toward south-western Turkey. The upper trough over the EM induces cold advection aloft into the Cyprus Low region. Fig. 20 presents the initial (left panels) and the decay (right panels) stages of the cyclone evolution over the EM. The presented COSMO simulations were initiated on 30/12/2015 00 UTC (left panel) and on 01/01/2016 00 UTC (right panel).
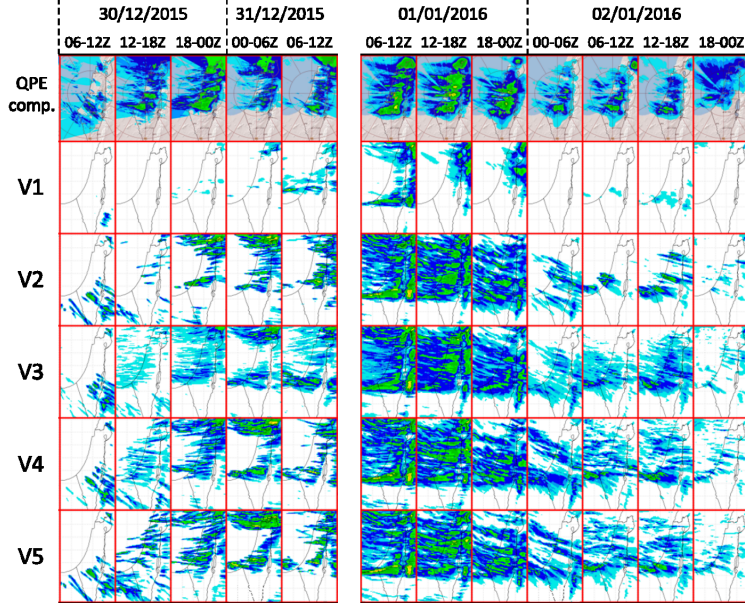
Figure 20: Initial (left panels) and the decay (right panels) stages of the Cyprus Low evolution over the EM (30/12/2015-02/01/2016). The QPE composite (first row) and five different COSMO SCP versions (see Table 3) forecasts are shown in 6hAP frames (rows 2-6). The peak of the cyclone evolution lasted for 18 hours during 31/12/2015 12Z – 01/01/2016 06Z and is not shown.

As explained in the previous section, the forecast for the peak of the cyclone evolution is not influenced by the SCP significantly. In this test case it lasted for 18 hours during 31/12/2015 12Z – 01/01/2016 06Z and is not shown. Fig. 20 (first row) presents the Quantitative Precipitation Estimation (QPE) composite evolution divided into 6 hourly accumulation periods (6hAPs). This QPE composite is compiled operationally at IMS using data from C-Band Doppler radar located in Bet Dagan and automatic rain gauges as described in Khain et al. (2020). The next five rows in Fig. 20 present 6hAP forecasts of the five COSMO versions (Table 3).

Version	$thick_{sc}$ [hPa]	$entr_{sc}$ [m^{-1}]	W_{max} [m/s]	Rain strength	Rain Cover
V1 (default)	25000	0.0003	-	Low	Low
V2	10000	0.0003	-	High	Low
V3	10000	0.003	-	Low	High
V4	10000	0.003	0.1	High	High
V4a	10000	0.003	0.3		
V4b	10000	0.003	0.15		
V4c	10000	0.003	0.05		
V5	SCP off	SCP off	SCP off	High	High

Table 3: Details of the five analysed versions of the COSMO SCP.

We begin the analysis of the five COSMO versions from comparing the "edge" versions V1 and V5, namely with very "active" SCP versus SCP turned off, respectively. Fig. 21 shows

the occurrence frequency of maximal over grid column wind speed and Convective Available Potential Energy (CAPE). The occurrence frequency was calculated for the period presented in Fig. 20 (30/12/2015-02/01/2016 without the 18 hours of the peak) over the sub domain 32-37E/29-34N.
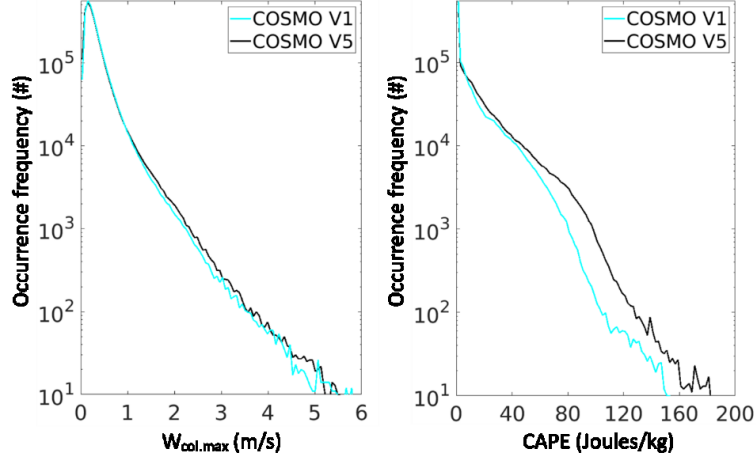
Figure 21: Occurrence frequency of (a) maximal over grid column wind speed and (b) CAPE. COSMO V1 (cyan) and V5 (black) are presented (see Table 3). The occurrence frequency was calculated for the period presented in Fig. 20 (30/12/2015-02/01/2016 without the 18 hours of the peak) over the sub domain 32-37E/29-34N. Note the logarithmic scale of y-axis.

As explained in the previous section, active SCP often weakens (or prevents) the evolution of grid scale convection and precipitation. Fig. 21 nicely shows that when the SCP is turned off, the updrafts are generally stronger and there are significantly more occurrences of high CAPE. As described in the previous section, COSMO SCP includes two tuning parameters. The first, $thick_{sc}$ (default value 25000 Pa), is the maximal vertical extent of the convection or the pressure difference between the top and the bottom, above which the scheme is automatically turned off. The second $entr_{sc}$ (default value 3×10^{-4} m^{-1}) is the entrainment rate, which defines the mixing intensity of the rising parcel with the surrounding. As will be reasoned below, we added a third parameter, W_{max} (default value 0.1 m/s) which is the maximal grid scale updraft speed in a grid column above which the SCP is automatically turned off. Using the selected test case (see Fig. 6.3) we analyse five versions of the COSMO SCP (Table 3). Versions 1-3 differ by the values of $thick_{sc}$ and $entr_{sc}$ parameters, while the effect of W_{max} is turned off. In version 4 we added changes in W_{max}. In version 5 we switch off the SCP so that convection may occur at grid scale only.

Spatial analysis of 6hAP precipitation which is presented in Fig. 20 (at the area covered by the radar) for QPE composite and precipitation forecast of various COSMO SCP versions yields the occurrence distributions (Fig. 22). The occurrence at each distribution bin, having width of 0.33 mm, reflects the average (over twelve 6hAP frames shown on Fig. 20) number of grid points which experienced 6hAP precipitation falling into that bin.

Figure 22: Occurrence distributions of precipitation over EM during a passage of Cyprus Low (30/12/2015-02/01/2016). The QPE composite (magenta) and five different COSMO SCP versions (see Table 3) forecasts are shown, respectively.

As can be seen from Fig. 20 and Fig. 22 (cyan compared to magenta), version 1 (see Table 3) strongly underestimates precipitation int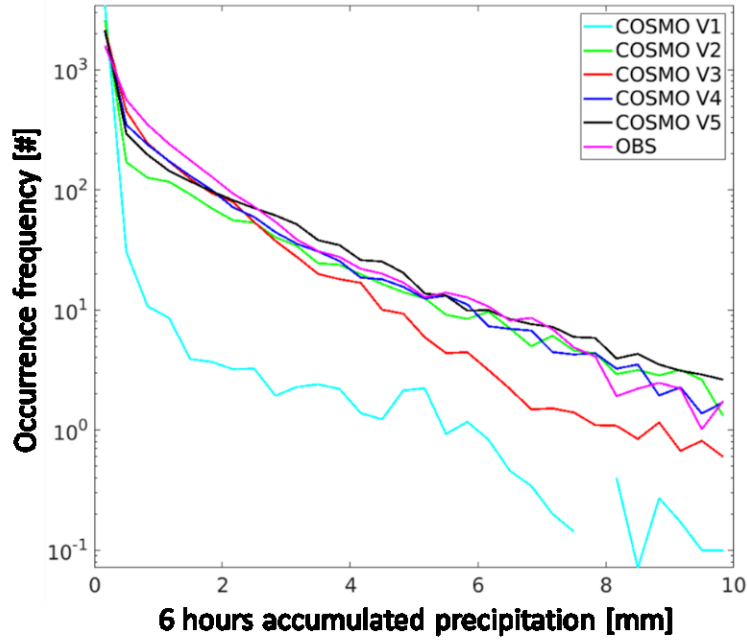ensity and area. Having nearly adiabatic parcels and high permitted vertical extension (low $entr_{sc}$ and high $thick_{sc}$, respectively), the SCP strongly mixes the lower atmosphere in vertical. This mixing ascends the water vapour from near the CBL top upwards into the free troposphere above the CBL. With less water vapour the grid-scale motions have lower potential producing grid-scale updrafts and precipitation.

Version 2 (V2) (green compared to magenta), performs better than V1, producing sufficiently strong precipitation. However, these strong precipitation spots are localized. Large areas still suffer from underestimation of weak precipitation. V2 differs from V1 by lower permitted vertical extension $thick_{sc}$. In strongly unstable areas the nearly adiabatic parcels (low $entr_{sc}$) can develop far above $thick_{sc}$. In these areas the SCP is turned off yielding proper grid scale updrafts and precipitation. In contrast, in weakly unstable areas the nearly adiabatic parcels do not reach the limit of $thick_{sc}$, the SCP is not turned off yielding strong vertical mixing and suppression of potential weak grid scale precipitation.

Version 3 (V3 - red compared to magenta), also shows positive results compared with V1, producing sufficiently wide precipitation cover. However it still suffers from underestimation of strong precipitation spots. V3 differs from V1 by lower permitted vertical extension $thick_{sc}$ and higher entrainment of the ascending parcels $entr_{sc}$. The physical motivation for increasing $entr_{sc}$ and the choice of its value are explained in the next section. Similarly to V2, in weakly unstable areas the diluted parcels (high $entr_{sc}$) do not reach the limit of $thick_{sc}$ and the SCP is not turned off. However, here the vertical mixing is weak and the potential weak grid scale precipitation is not suppressed. Since SCP is rarely turned off, in strongly unstable areas these diluted parcels still cause significant vertical mixing partially suppressing potentially strong grid scale updrafts and precipitation.

Hence, in the framework of COSMO mass-flux SCP having two parameters for maximal

permitted vertical extension and the entrainment rate it seems impossible to reproduce the precipitation spatial distribution (magenta in Fig. 22) correctly. There is underestimation of either the cover by weak precipitation (version 2) or the strong precipitation values (version 3). Following the physical motivation behind version 3 (see Appendix), this version is chosen for further improvement. As mentioned above, in this version the SCP is rarely turned off even in strongly unstable situations. To solve this issue we added a third parameter (W_{max}, default value 0.1 m/s) which is the maximal grid scale updraft speed in a grid column above which the scheme is automatically turned off (version 4). The physical motivation is obvious – in grid column with sufficiently strong updraft, there is a potential for initiation of grid scale convection. In such column, switching off subgrid scale mixing by the SCP allows further CAPE development, followed by grid scale convection and precipitation. As can be seen from Fig. 20 (V4) and from Fig. 22 (blue compared to magenta), version 4 (Table 3) shows better results than versions 1-3, producing not only sufficiently wide precipitation cover but also sufficiently strong precipitation spots. The optimal value for W_{max} will be chosen following the tuning over ten test-cases (see next section).

A question arises, whether SCP is essential to the model, or it can be continuously turned off over the entire model domain. This test is conducted in version 5 (Table 3). As can be seen from Fig. 20 (V5) and from Fig. 22 (black compared to magenta), version 5 is of similar quality to version 4 producing sufficiently wide precipitation cover and sufficiently strong precipitation spots. However, SCP is essential in slightly unstable areas not covered by precipitation. In such areas lack of vertical mixing, which does occur at nature, may yield to concentration of heat and moisture at lower levels, causing wrong vertical profiles of temperature and humidity.

6.4 The entrainment rate parameter $entr_{sc}$

As explained in Sec. 6.2, the entrainment parameter $entr_{sc}$ plays an important role in the SCP. Higher $entr_{sc}$ values reduce both the intensity and the vertical extent of the mixing by the SCP. During the ascent, a parcel becomes saturated, yielding a condensation of water vapour to cloud water, resulting a profile of liquid water content LWC(z). This profile is closely related to $entr_{sc}$. For higher $entr_{sc}$ values, the ascending parcel saturation is postponed, yielding smaller values of LWC. For $entr_{sc} = 0$ the parcel is raised adiabatically resulting in the highest possible value of LWC (hereafter, $LWC_{ad}(z)$). Both $LWC_{ad}(z)$ and the expected vertical profile of LWC in shallow Cu (hereafter, $LWC_{cu}(z)$) are discussed in Khain et al., 2019. Obviously, COSMO mass flux SCP cannot reproduce the exact $LWC_{cu}(z)$ produced by large-eddy-simulations and compared with observations. Still, comparison of LWC(z) with $LWC_{cu}(z)$ may help setting up the correct value of $entr_{sc}$. For that purpose, we define LWC normalized adiabatic ratio averaged over height (z) above cloud base:

$$\text{LWC}_{\text{ratio}} = \overline{\frac{LWC(z) - LWC_{cu}(z)}{LWC_{ad}(z) - LWC_{cu}(z)}} \tag{23}$$

Positive (negative) values of $\text{LWC}_{\text{ratio}}$ indicate too large (small) LWC(z) and too small (large) $entr_{sc}$. The optimal value of $entr_{sc}$ is obtained for $\text{LWC}_{\text{ratio}} \approx 0$. In order to estimate the optimal $entr_{sc}$, several values were selected: $3 \cdot 10^{-6}$, $3 \cdot 10^{-4}$, 10^{-3}, $3 \cdot 10^{-3}$ and 10^{-2}. For each of these values, we have performed COSMO forecasts for two events, one in winter and one in summer, dominated by shallow convection. The first COSMO forecast was initiated on 23/02/2018 00 UTC, and the second – on 03/06/2018 00 UTC. For each 78 hours range forecast, all the grid columns with active shallow convection were analysed and the LWC(z) was plotted versus height above cloud base. Fig. 6.6 presents the vertically, horizontally and

time-averaged LWC_{ratio} versus $entr_{sc}$ for winter case (red) and summer case (blue). One can see, that for negligible value of $entr_{sc}=3\times10^{-6}$ m^{-1} LWC_{ratio} is close to one, meaning that COSMO shallow convection scheme describes adiabatically ascending parcels. For default COSMO value of $entr_{sc}=3\times10^{-4}$ m^{-1}, LWC_{ratio} is around 0.5, meaning strong overestimation of vertical mixing by the SCP. Note that for $entr_{sc}=3\times10^{-3}$ m^{-1}, $LWC_{ratio}\approx0$, and therefore this value was chosen for further tuning of the SCP in Sec. 6.6.
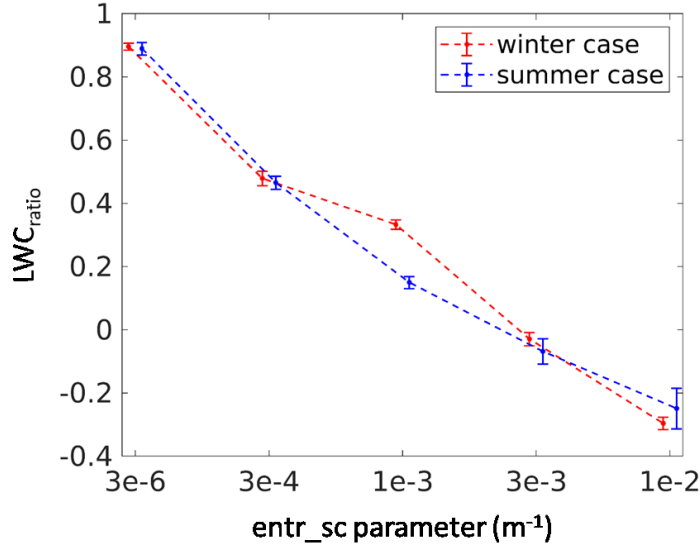
Figure 23: Vertically, horizontally and time-averaged LWC_{ratio} versus $entr_{sc}$ for winter case (23/2/2018 00 UTC run - red) and summer case (03/06/2018 00 UTC run - blue).

6.5 Evaluation of forecast quality

In order to analyse the forecasts quality two scores were chosen: precipitation verification score ΔFSS and temperature and humidity verification score T_RH_PROF.

6.5.1 Precipitation verification score $\mathbf{\Delta FSS}$

Due to the high variability of precipitation in space and time, it is common to verify it using Neighbourhood Methods. Here we use the Fractional Skill Score (FSS) (Roberts and Lean, 2008; Ebert, 2009; Mittermaier and Roberts, 2010). Besides FSS, additional neighbourhood methods of verification exist in the literature. These include extension of FSS to time dimension (Duc et al., 2013), scale-separation, object-based, and field deformation approaches (Davis et al. 2006a,b; Davis et al. 2009; Gilleland et al., 2009, 2010; Ben Bouallègue and Theis, 2014; Schwartz and Sobash, 2017). For each 6hAP forecasted and observed map, FSS was calculated for 30 km smoothing radius (see Khain et al. 2019 for the motivation) and for the thresholds of 0.01, 0.1, 0.5, 1, 2, 5, 10, 20 mm per 6h. The resulting FSSs were averaged over these thresholds, assuming double weight for the thresholds 0.5, 1, 2, 5 mm per 6h. The last are usually more important for the public than the negligible 0.01 and 0.1 mm per 6h and occur much more often than 10 and 20 mm per 6h. These averaged FSS were calculated both for COSMO and IFS and denoted as FSS_{COS} and FSS_{IFS}, respectively. Finally the precipitation verification score ΔFSS for each COSMO run was defined as:

$$\Delta FSS = \overline{FSS_{COS} - FSS_{IFS}} \tag{24}$$

where the average is over forecast ranges from +6h till +60h. ΔFSS varies in the range [-1,1], where $\Delta FSS > 0$ ($\Delta FSS < 0$) means COSMO precipitation forecasts are better (worse) than of IFS. As can be seen, IFS forecasts are of similar quality to those of COSMO, and it is convenient to use it as a reference.

6.5.2 Temperature and relative humidity score T_RH_PROF

The SCP is intended to vertically mix the CBL, and as such has a major influence on the temperature and relative humidity in the BL. In order to tune the scheme, we introduce the T_RH_PROF score which combines the verification of 2m-temperature and relative humidity versus stations measurements with the verification of the vertical profiles of temperature and mixing ratio versus radio-sounding data.

For each forecast initialized at 00 UTC the forecast ranges of +12h till +72h were verified at 12 hour steps. For 2-meter variables each forecast was verified versus 81 IMS stations over Israel, yielding RMSE for 2m-temperature and relative humidity (RMSET2m and RM-SERH2m, respectively). For profiles verification we used the radio-sounding launched from Bet-Dagan (34.814E/32.007N) twice daily (at 00 and 12 UTC). Each model profile was interpolated on the radio-sounding measurements heights, and the RMSE was calculated giving five times larger weight to heights below 2 km above surface. The resulting RMSEs were averaged over the various forecast ranges yielding verification score for temperature profile (RMSETprof) and mixing ratio profile (RMSEQprof). These four scores were calculated for each COSMO (RMSET2m_cos, RMSERH2m_cos, RMSETprof_cos, RMSEQprof_cos) and IFS (RMSET2m_ifs, RMSERH2m_ifs, RMSETprof_ifs, RMSEQprof_ifs) forecast. Similarly to precipitation score described above, we normalize COSMO scores with respect to IFS and define $Skill_{field} \equiv 1 - \frac{RMSE_{field\_cos}}{RMSE_{field\_ifs}}$, where $field$ can be T2m, TH2m, Tprof or Qprof. Finally, temperature and relative humidity verification score T_RH_PROF for each COSMO run is defined as:

$$T\_RH\_PROF = \frac{1}{4}\left(Skill_{T2m} + Skill_{RH2m} + Skill_{Tprof} + Skill_{Qprof}\right) \tag{25}$$

T_RH_PROF varies in the range $[-\infty, 1]$, where $T\_RH_{PROF} > 0$ ($T\_RH_{PROF} < 0$) means COSMO precipitation forecasts are better (worse) than of IFS.

6.6 Tuning the shallow convection scheme

At this section we use ten typical rainy events first to show that turning off the SCP in cases of too strong grid scale updrafts (larger than W_{max}) improves the forecast, and second, to define the optimal W_{max}. Brief characteristics of the chosen events are summarized in Table 4. The chosen events are typical to rain season over EM. Usually during these 3-days long events significant parts of the simulation domain and the verification area are characterized by fair weather alongside unstable cyclonic areas. Therefore the following verification is not limited to rainy areas.

For each of the COSMO versions V1-V5 (see Table 3) a simulation was performed over the 10 chosen events (Table 4). In order to reveal the optimal W_{max}, three additional simulations V4a, V4b, V4c were performed using W_{max} values of 0.3, 0.15, 0.05 m/s, respectively. For

42

Chosen rainy events	Model initiation time	Max. accum. precipit. (mm)	Peak time Bet-Dagan sounding	m.s.l pressure (hPa)	850 hPa temp. (C)	500 hPa geopot. height (m)	500 hPa temp. (C)
12-14/ 12/2016	12/12 00 UTC	116	14/12 12UTC	1007	1.6	5510	-18.3
23-25/ 12/2016	23/12 00 UTC	76	25/12 00UTC	1011	1.6	5540	-19.3
11-13/ 02/2017	11/02 00 UTC	44	13/02 12UTC	1010	2.4	5530	-26.1
14-16/ 02/2017	14/02 00 UTC	68	16/02 00UTC	1112	0.0	5520	-21.9
12-14/ 04/2017	12/04 00 UTC	27	14/04 00UTC	1007	7.6	5650	-17.3
20-22/ 11/2017	20/11 00 UTC	47	22/11 00UTC	1011	4.6	5610	-18.9
05-07/ 12/2017	05/12 00 UTC	30	06/12 12UTC	1010	4.6	5600	-16.5
05-07/ 01/2018	05/01 00 UTC	66	05/01 12UTC	1001	3.6	5510	-22.3
18-20/ 01/2018	18/01 00 UTC	49	19/01 00UTC	1001	2.0	5420	-27.3
16-18/ 02/2018	16/02 00 UTC	66	17/02 12UTC	1007	3.0	5500	-25.3

Table 4: Characteristics of 10 selected rain events over EM. The columns from left to right represent: dates of each event; initiation time of COSMO run; maximum accumulated precipitation during the entire event at specific location; the time of sounding representing the peak of the event; Mean-sea-level pressure from the sounding; 850 hPa temperature from the sounding; 500 hPa geopotential height from the sounding; 500 hPa temperature from the sounding.

each simulation, the T-RH-PROF and ΔFSS scores were calculated. Fig. 24 presents ΔFSS (red dots) and T_RH_PROF (blue dots) for the various versions, calculated for the 10 chosen events. The dots were connected by straight lines to make the comparison of different versions more convenient.
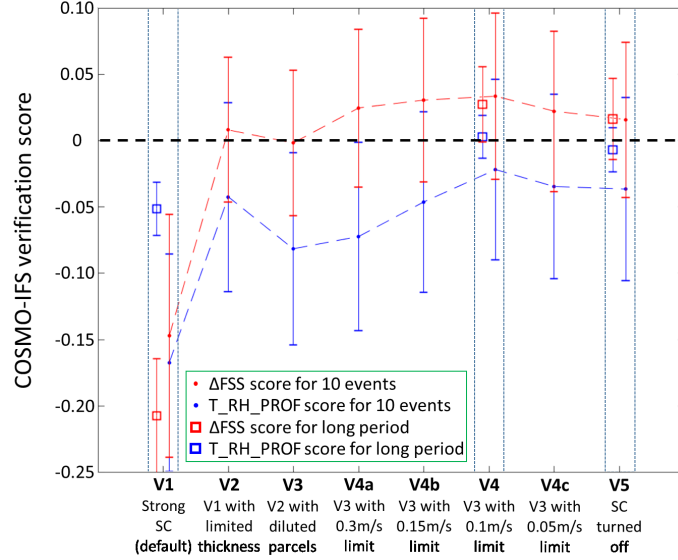

Figure 24: ΔFSS (red dots) and T_RH_PROF (blue dots) verification scores for the various versions (Table 3), calculated for the 10 chosen rain events (Table 4). The dots were connected by straight lines to make the comparison of different versions more convenient. The verification scores ΔFSS and T_RH_PROF for the entire winter season 01/11/2017-31/03/2018 are presented by red and blue squares, respectively.

One can see that reduction of the maximum allowed thickness for the shallow convection ($thick_{sc}$ parameter) significantly improves the forecast (V2 vs. V1). As mentioned above, this limitation is crucial as it allows the grid scale convection to develop. The increase of the entrainment rate ($entr_{sc}$ parameter), which is physically motivated in the appendix, slightly worsens the forecast (V3 vs. V2). As discusses in the previous section (Figs. 20 and 22), V3 improves the weak precipitation coverage at the expense of deterioration of strong precipitation. Introduction of maximum allowed updraft (W_{max} parameter) for the shallow convection further improves the forecast. One can see a pronounced optimum at W_{max}= 0.1 m/s (version V4). At first glance, such low value seems too weak for realistic shallow convection. However, this grid scale value represents an averaged updraft over the model grid box of about $(2.5\ km)^2$. For higher horizontal resolutions W_{max} has to be retuned, and higher values are expected. Back to the current resolution, reduction of W_{max} towards 0.05 m/s (version V4c) slightly worsens the forecast. In this configuration the SCP switches off too frequently even in fair weather conditions, and is not replaced by grid scale vertical mixing. Such configuration mistakenly keeps the lower atmosphere unmixed, yielding in slight degradation of the verification scores. Finally, continuous switching off the SCP over the entire domain (V5) shows additional slight degradation of the performance.

At last, we show that the above tuning based on 10 rainy events indeed improves the wintertime forecasts over the EM. Versions V1 (default – strong SCP), V4 (optimum) and V5 (no SCP) were used to perform simulations over an entire winter season 01/11/2017-31/03/2018 (in total 151 72h-long simulations for each version). The verification scores T_RH_PROF

and ΔFSS were calculated for the entire period and are presented on Fig. 24 designated by blue and red squares, respectively. One can see that V4 is indeed optimal. However, the advantage over V5 (no SCP) is not significant. In rainy days switching off SCP might indeed be as good as V4 version, and definitely much better than activating the default SCP (version V1). On contrast, in fair weather days switching off SCP deteriorates the forecast. To prove it we performed similar analysis over all the fair weather forecasts, total of 75 cases, during the period 01/11/2017-31/03/2018. To isolate the main effect of the SCP, we focused on temperature verification part of 25 i.e. $T\_PROF_T = \frac{1}{2}(Skill_{T2m} + Skill_{Tprof})$ during day times of each forecast (three 12 UTC values). It turns out that $T_{PROF_T} = -0.0001 \pm 0.0204$ for version V4 (optimal) which is significantly better than $T_{PROF_T} = -0.0472 \pm 0.0227$ for V5 (no SCP).

6.7   Discussion and conclusions

NWP models in convection permitting resolution often resolve deep convection but parametrize the shallow convection. This combination may have negative effect significantly influencing the model forecast. Majority of SCPs used in NWP convection permitting models are based on the mass-flux approach. In this work we analysed the effect of the widely used mass-flux SCP on COSMO model forecasts in convection permitting resolution of 2.5 km. On one side, the default configuration of the SCP turns out to be too active, causing decay of precipitation. On the other side, in fair weather without SCP the vertical mixing in the PBL is underestimated yielding degradation of temperature profiles. It turns out that even within the framework of regular mass-flux SCP, one can still find a delicate compromise by limiting the SCP activity. This compromise can be achieved by limiting the vertical extent, the entrainment rate and the updraft speed of the parametrized SC. The effect of each of the limitations thoroughly analysed using a test case of cyclone passage over the eastern Mediterranean (EM). Physically motivated tuning of the related parameters was performed using ten rainy events showing significant forecast improvement, which was validated based on entire rain season over the EM.

We now address the question whether SCP is important in other climatic zones except of EM. Although this question can be a topic of a different study, we provide a rough estimate below. As was shown, SCP significantly influences the forecast in unstable stratifications topped by an inversion around 800 to 500 hPa, as well as in weakly unstable situations. It is, however, not influencing severe situations with strongly unstable stratification reaching the upper troposphere. It is also not playing role in stable stratification dominated by stratiform precipitation. Although there are exceptions related to local climate, generally the central European climate is characterized by stratiform precipitation during wintertime and strongly convective during summertime. The Mediterranean climate is generally characterized by moderate convective precipitation during wintertime, strong convective events during autumn and spring, and dry summer. These weather types can be reasonably distinguished by CAPE values. In order to demonstrate these characteristics, we analysed the CAPE climatology in 8 sounding locations (Table 5) - 4 characterized by Mediterranean climate (hereafter "Mediterranean") and 4 more characterized by central European climate (hereafter "European").

For each location, twice daily (00 and 12 UTC) sounding data was retrieved for 20 years period 1/1/2000-31/12/2019 (www.weather.uwyo.edu/upperair/sounding.html). At each location at least 6000 available records exist allowing calculation of CAPE. Moreover, each of these stations provides 6 hourly precipitation measurements. In order to focus on rainy events, we selected only those CAPE values where there was non zero precipitation during

Sounding station	Station number	Location	Latitude (deg.)	Longitude (deg.)	Climate
Bet-Dagan	40179	Bet-Dagan (central Israel)	32.00	34.81	"Mediterranean"
LIRE Pratica di Mare	16245	Rome (central Italy)	41.65	12.43	"Mediterranean"
LIBR Brindisi	16320	Brindisi (south east Italy)	40.65	17.95	"Mediterranean"
LFKJ Ajaccio	07761	Ajaccio (Corsica, France)	41.91	8.80	"Mediterranean"
Praha-Libus	11520	Prague (Czech Republic)	50.00	14.45	"European"
EHDB De Bilt	06260	De Bilt (Netherlands)	52.10	5.18	"European"
LSMP Payerne	06610	Payerne (Switzerland)	46.81	6.95	"European"
LIML Milano	16080	Milan (North Italy)	45.43	9.28	"European"

Table 5: Sounding stations selected for CAPE analysis.

the last 6 hours. Fig. 25 shows the 90th percentile of monthly CAPE values at 4 "Mediter-ranean" locations (solid lines) and 4 "European" locations (dashed lines). Monthly CAPE values based on sample sizes below 30 were neglected.
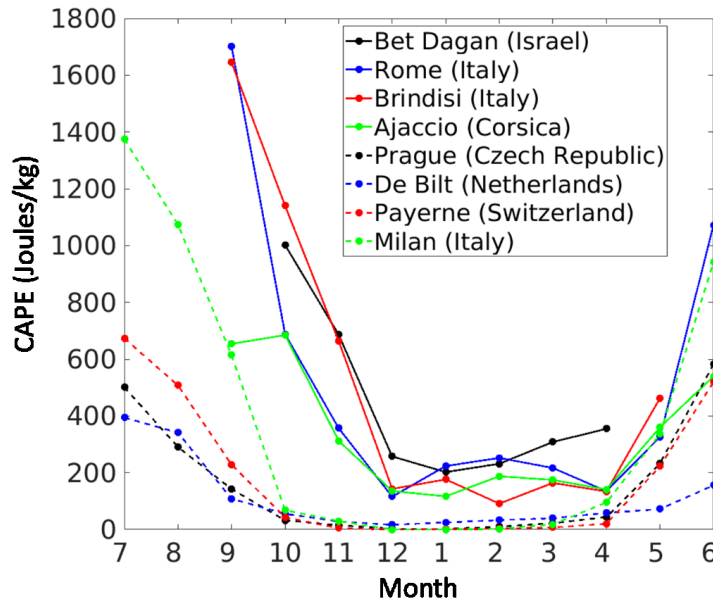

Figure 25: 90th percentile of monthly CAPE values at 4 "Mediterranean" locations (solid lines) and 4 "European" locations (dashed lines). The sample contains twice daily (00 and 12 UTC) sounding data for the period 1/1/2000-31/12/2019. Only CAPE values with non-zero precipitation during the last 6 hours were selected. Monthly CAPE values based on sample sizes below 30 were neglected.

As expected, during wintertime the "Mediterranean" locations are characterized by moderate CAPE around 100-300 J/kg. These are the values where SCP is expected to play an important role. However, wintertime at "European" locations is characterized by stratiform precipitation and hence negligible CAPE (below 50 J/kg). Consequently, we do not expect SCP to play an important role during European winter. Generally, the autumn and spring at the "Mediterranean" locations and summertime at the "European" locations are characterized by strong convective precipitation with high values of CAPE (300-1700 J/kg). SCP is automatically turned off in these cases and is not expected to influence the forecast. We do expect the SCP to influence the forecast during European autumn and spring where the CAPE values are moderate. The above statements are general and there are many exceptions. For example, De Bilt (Netherlands) shows moderate CAPE also during summer, so that SCP might be important there as well. Hence, in order to estimate whether and during which seasons the SCP is an important factor in NWP, one has to look at local climatology of CAPE.

To conclude, nowadays many weather forecasting centres run convection permitting NWP models, and often face difficulties obtaining satisfactory forecasts, particularly of precipitation. As mentioned, majority of these models resolve deep convection and use mass-flux approach to parametrize the shallow convection. This study shows that SCP configuration might be of crucial importance to the model forecasts. We believe that it sheds light on the numerical processes through which SCP affects the model forecasts, and most importantly, it provides a recipe to improve them.

7 Implementation of CAMS forecasted aerosols in COSMO radiation and microphysics schemes

(H. Muskatel, U. Blahak, P. Khain)

7.1 Introduction

Operational NWP models requires assessment of aerosols loads for both radiation transfer calculations (direct effect) and for microphysical parametrizations of liquid droplets activation and ice particles heterogeneous nucleation processes (indirect effect). Two approaches are often chosen for aerosols evaluation. First is using climatology values where yearly fixed values are chosen for each aerosol species as in Tanre climatology (Tanre et al., 1984, itype_aerosol = 1) or monthly means as in Tegen (Tegen et al., 1997, itype_aerosol = 2) and MACv2 (Kinne et al. 2013, itype_aerosol = 3) climatologies. All the three options mentioned above are available in the latest COSMO-CLOUDRAD version. In this approach the computational effort is minimal but air pollution events are neglected and sometimes severely degrade forecast skills (i.e. in dust outbreaks or volcanic eruptions events). The second approach is online-coupling of NWP models with aerosols and reactive trace gasses forecast. In these models (i.e. COSMO-ART and ICON-ART) the aerosols are treated as additional tracers and processes like emissions, wet and dry deposition, sedimentation and transport need to be explicitly calculated. This approach is usually expensive in terms of CPU consumption. As a result, it is operationally used as parallel modules to operational run with lower spatial resolution (i.e. ICON-ART-dust runs in DWD) or non-operationally upon demand (i.e. COSMO-ART). In this project we offered a third approach where the offline low resolution fully-coupled aerosols models forecast outputs are used as an input for the operational non-coupled LAM model. In this chapter we describe the use of CAMS-ECMWF forecasted aerosols as input for COSMO radiation and microphysics schemes while in chapter 8 we will discuss the use of ICON-ART-dust forecast. In this new approach the advantages compared to aerosols climatology is obvious since synoptic scale events including aerosols are included while being neglected in aerosols climatology approach. Since COSMO boundary and initial conditions are taken from global models (i.e. IFS or ICON), using the forecasted global aerosols based on these forecasting systems is a natural choice. The difference between interpolating atmospheric fields such as temperature and pressure from the driving model to the use of aerosols fields is that the data is updated in time, as for boundary conditions data, but for applied to the entire domain. The values of aerosols mixing ratios in 3D between two snapshots of aerosols fields are interpolated in space and time by INT2LM. The computational cost during runtime is minimal, since most calculations are performed in the pre-processing stage. Technically, INT2LM needs double run: once for the regular driving model and once for the aerosols. The initial and boundary files are later combined. The disadvantage of such method is that the aerosols are not coupled with COSMO dynamics but being advected, washed-out etc., only by the offline global aerosols model (i.e. CAMS). Differences in dynamics between the aerosols model and COSMO may lead to errors. Nevertheless, in the everlasting conflict between model realism and computational cost, we show that this is a fair compromise for operational NWP applications.

7.2 CAMS aerosols forecasting system

The Copernicus Atmosphere Monitoring Service (CAMS, formerly series of MACC projects) is an ECMWF project that provides near-real-time analysis and forecast of atmospheric

composition: aerosols, reactive gases, greenhouse gases, ozone, UV radiation and more. The aerosols 5-days ahead forecast is available twice a day with a 1-hour resolution. CAMS is based on IFS model with additional prognostic aerosols which are interactive with the dynamics and physics of the parent model (Morcrette et al. 2009). The processes treated are: emissions sources (some are updated in near-real-time), horizontal and vertical advection, dry and deposition, sedimentation and hygroscopicity. CAMS includes aerosols data assimilation using MODIS Terra and Aqua aerosols optical depth (AOD) and verified against AERONET AOD. The forecasted aerosols are mineral dust (MD) divided to three size bins, sea salt (SS) also with three size bins, black carbon (BC) and organic matter (OM) which both includes hydrophilic and hydrophobic species and Sulfate (SU). In Fig. 26 CAMS aerosols size limits, mode radius r_{mode} and geometric standard deviation σ of the log-normal distributions used to describe particle size distribution are presented. The mean volume particle masses of each species was numerically calculated using the formula:

Aerosol type	Size limits [µm]	r_{mode} [µm]	σ	modes weights	ρ [kg/m³]	Particle mean mass [kg] at RH=80%	Soluble fraction
Sea salt	[0.03, 0.5]	0.1992, 1.992	1.9, 2.0	0.959, 0.041	1183	$7.50 \cdot 10^{-17}$	1
Sea salt	[0.5, 5]	0.1992, 1.992	1.9, 2.0	0.959, 0.042	1183	$3.33 \cdot 10^{-15}$	1
Sea salt	[5, 20]	0.1992, 1.992	1.9, 2.0	0.959, 0.043	1183	$9.34 \cdot 10^{-15}$	1
Dust	[0.03, 0.55]	0.29	2.00	1	2610	$2.87 \cdot 10^{-16}$	0.1
Dust	[0.55, 0.9]	0.29	2.00	1	2610	$4.73 \cdot 10^{-16}$	0.1
Dust	[0.9, 20]	0.29	2.00	1	2610	$1.56 \cdot 10^{-15}$	0.1
OM Hydrophilic	[0.005, 20]	0.0212	2.24	1	1800	$4.00 \cdot 10^{-18}$	0.59
OM Hydrophobic	[0.005, 20]	0.471, 0.0118	2.51, 2.0	$4.3 \cdot 10^{-5}$, 0.999952	2000, 1000	$4.91 \cdot 10^{-19}$	0
BC Hydrophilic	[0.005, 5]	0.0118	2.00	1	1000	$1.78 \cdot 10^{-19}$	1
BC Hydrophobic	[0.005, 5]	0.0118	2.00	1	1000	$5.98 \cdot 10^{-20}$	0
Sulfate	[0.005, 20]	0.0355	2.00	1	1760	$9.38 \cdot 10^{-19}$	1

Figure 26: CAMS aerosols size limits, mode radius r_{mode} and geometric standard deviation σ of the log-normal distributions used for particle size distribution. Sea salt and hydrophobic organic matter are described by a bimodal log-normal distributions with mode weights given in the third column from the right. ρ is the particle density. The particles mean masses were numerically calculated using Eq. 26.

$$\overline{m_v} = \frac{4\pi}{3} \rho \int_{r_{min}}^{r_{max}} r^3 \frac{1}{\sqrt{2\pi} ln\sigma \cdot r} \exp\left\{ -\frac{1}{2} \left[\frac{\ln(r/r_{mode})}{ln\sigma} \right]^2 \right\} dr \qquad (26)$$

7.3 CAMS aerosols direct effect on radiation

7.3.1 CAMS aerosols optical properties

CAMS aerosols optical properties namely the extinction coefficient, the asymmetry factor and single scattering albedo, were originally calculated for IFS radiation RRTM scheme. This model has 16 wavelength intervals in the long-wave range (LW) and 14 intervals in the short wave (SW) range (A. Bozzo, private communication, 2016). In COSMO RG92 scheme there are only 5 intervals for LW and 3 intervals in the SW. Therefore, a special spectral averaging similar to the averaging procedure performed for ice particle as explained in Muskatel et al. (2021), was used to transfer the IFS high spectral resolution data to COSMO radiation scheme. The calculation includes weighting of the solar irradiance intensity at each wavelength according to Planck's function and layer thickness. The optical properties of the sea salt, sulfate and hydrophilic organic matter depend on relative humidity (RH) due to their growth factor in presence of water vapour. Larger RH usually results in

larger single-scattering albedo, extinction coefficient and asymmetry factor but these properties also depend on wavelength. An example for sea salt asymmetry factor for different RH for four COSMO spectral intervals are shown in Fig. 27. For the first time in COSMO radiation scheme, the optical properties of aerosols at each grid point is RH dependent.
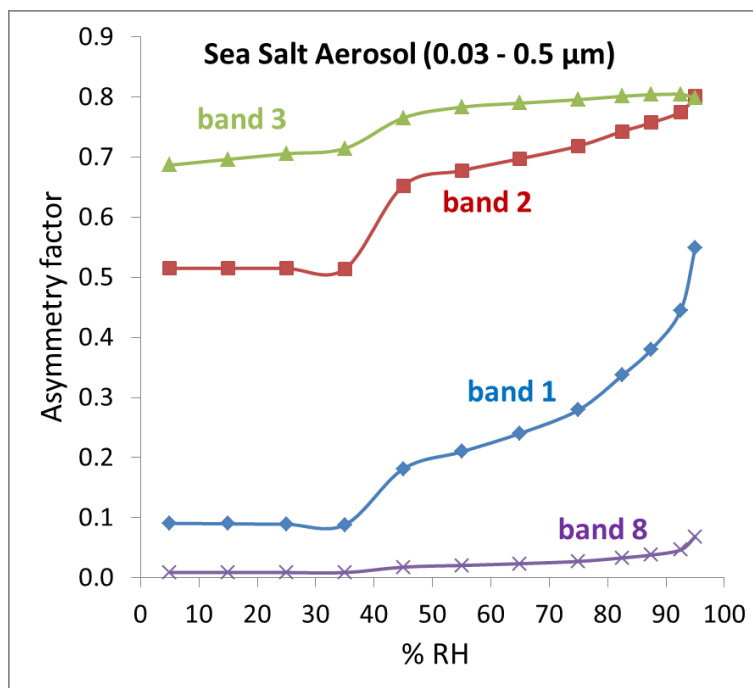
Figure 27: An example for CAMS aerosols asymmetry factor values of sea salt as function of relative humidity for COSMO bands 1 (1.53 $\mu m - 4.64$ μm), 2 (0.7 $\mu m - 1.53$ μm), 3 (0.25 $\mu m - 0.7$ μm), 8 (4.64 $\mu m - 8.33$ μm) data adapted from IFS RRTM radiation scheme (A. Bozzo, private communication, 2016) to COSMO RG92.

7.3.2 Testing the direct effect of CAMS aerosols on COSMO radiation

Direct effect of CAMS aerosols load in COSMO radiation scheme compared to other aerosols inputs were tested in several frameworks. The first is a using data from 10 selected radiation stations in Israel and two AERONET stations AOD measurements in Sede-Boker and Technion (see Fig. 28).

50

Figure 28: Israel satellite image with the locations of 10 IMS radiation (red dots) and 2 AERONET (blue dots) measurements stations. The data sets from these stations were used for the verification of COSMO aerosols inputs scenarios.
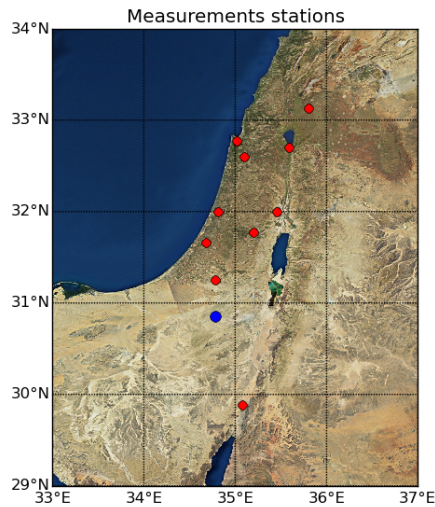
In the first verification, 29 selected test cases for mixed weather situations in the years 2015-2016 were chosen. The forecast range was either 30 or 42 hours using COSMO 5.0 version with spatial resolution of 2.8 km on IMS domain (see Fig. 37). Four versions were compared: the operational COSMO version with Tanre climatology, the new CLOUDRAD scheme with Tanre climatology, Tegen climatology and CAMS forecasted aerosols. The observational AOD data was taken from the AERONET station in Sede-Boker. In Fig. 29 one can see the models setup results for clear skies conditions. The cloudiness was defined by the model cloud cover. The points from all stations and hours of the day appear in one plot, model vs. observation. The 1:1 (black) line represents the ideal forecast. One can see that in both operational and the new CLOUDRAD versions, if Tanre climatology is used, the radiation is underestimated, which indicates an AOD overestimation. The negative bias almost disappears when using the new CLOUDRAD with both Tegen climatology or CAMS forecasted aerosols due to smaller error in AOD estimation (see Fig. 30). The AOD and global radiation bias and RMSE of climatology/model against 10 radiation stations and AERONET measurements in Sede-Boker for 7 test cases are presented in Fig. 30. The average RMSE and bias for these 7 clear skies cases and another 22 cloudy skies days are summarized in Fig. 26. The advantage of Tegen and CAMS over Tanre seems to vanish in cloudy skies condition probably due to the model tuning which was adapted to the operational setup.

51
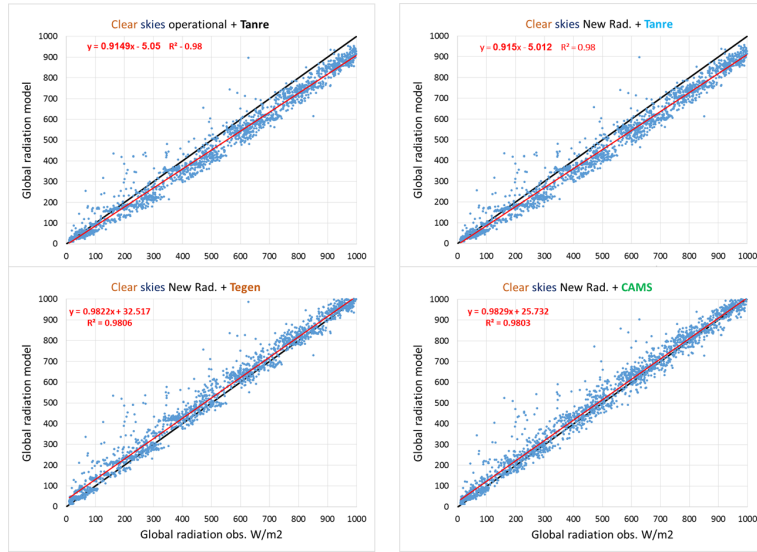
Figure 29: Clear skies conditions results for four radiation setups: operational COSMO version with Tanre climatology (upper left), new CLOUDRAD scheme with Tanre climatology (upper right), new CLOUDRAD with Tegen climatology (lower left) and new CLOUDRAD with CAMS forecasted aerosols (lower right) against measurements from 10 radiation stations in Israel. The 1:1 black line is the ideal match and red line is the linear fit between model and observation.
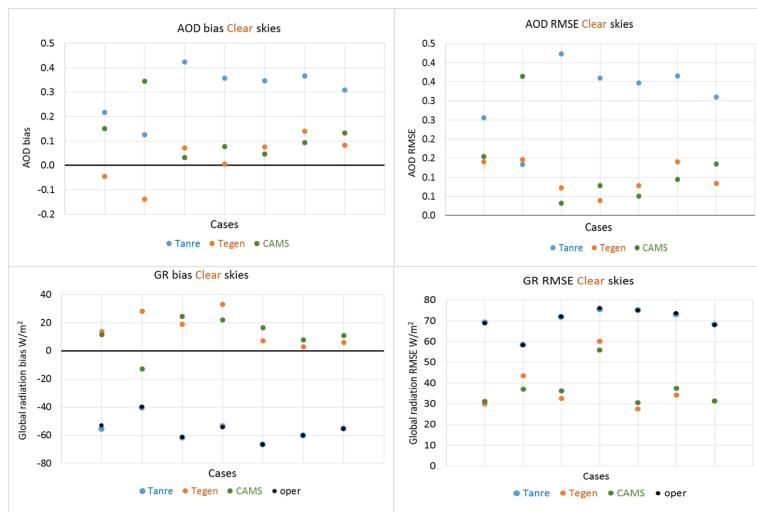
Figure 30: Clear skies conditions results for 7 test cases (17-18 May 2015, 14 and 26 February 2016, 18 April 2016, 19 and 24 June 2016) for four radiation setups: operational COSMO version with Tanre climatology (black), new CLOUDRAD scheme with Tanre climatology (Azure), new CLOUDRAD with Tegen climatology (orange) and new CLOUDRAD with CAMS forecasted aerosols (green). Upper panels show the AOD bias (left) and RMSE (right) climatology vs. measurement in AERONET station in Sede-Boker. Lower panels display the bias and RMSE of global radiation against measurements in 10 radiation stations in Israel.

Model	Clear skies (7 test cases)				Cloudy skies (22 test cases)			
	AOD		Global Radiation W/m^2		AOD		Global Radiation W/m^2	
	bias	RMSE	bias	RMSE	bias	RMSE	bias	RMSE
Tanre	0.31	0.31	-56.2	70.1	0.20	0.28	-11.1	131.5
Tegen	0.03	0.10	15.6	37.0	-0.12	0.17	54.2	140.5
CAMS	0.12	0.13	11.4	37.1	0.11	0.14	40.7	140.4

Figure 31: Clear skies (7 test cases) and cloudy (22 test cases) conditions results for three aerosols models input for COSMO-CLOUDRAD radiation scheme. AOD bias and RMSE calculated against AERONET data in Sede-Boker. Global radiation bias and RMSE are against measurements in 10 radiation stations in Israel (see Fig. 28).

Proper tuning of the CLOUDRAD version improves the scores even for cloudy skies conditions as can be seen in Fig. 32. In this Fig. the global radiation results for three models are presented: ECMWF-IFS with CAMS climatology (red), COSMO operational scheme with Tanre climatology and CLOUDRAD with CAMS forecasted aerosols. The period is July-August 2019 in IMS operational domain and verified against 17 ground based stations. Cloudy/clear skies definition was made by using CMSAF cloud cover product (https://www.cmsaf.eu) where clear/cloudy skies situations are defined when all models and satellite observation CLC is lower/larger than 5/95 % respectively. The RMSE for CLOUDRAD-CAMS version is the lowest compared to IFS and operational COSMO-Tanre version which has the largest RMSE for the entire period (Fig. 32 Upper-left). In the upper-right panel of Fig. 32 we see that the occurrences of errors larger than 50 W/m^2 (fiascos) in global radiation forecast is smallest in CLOUDRAD-CAMS compared to other models. Nevertheless, the mean bias of CLOUDRAD-CAMS is comparable to IFS in cloudy conditions (lower-left) and slightly higher than IFS. The bias of operational COSMO-Tanre is in the order of $\sim$50 W/m^2 in both cloudy and clear skies. COUDRAD-CAMS improved the bias also in cloudy skies conditions, indicates that the tuning procedure (see Sec. 10) significantly improved model skill.
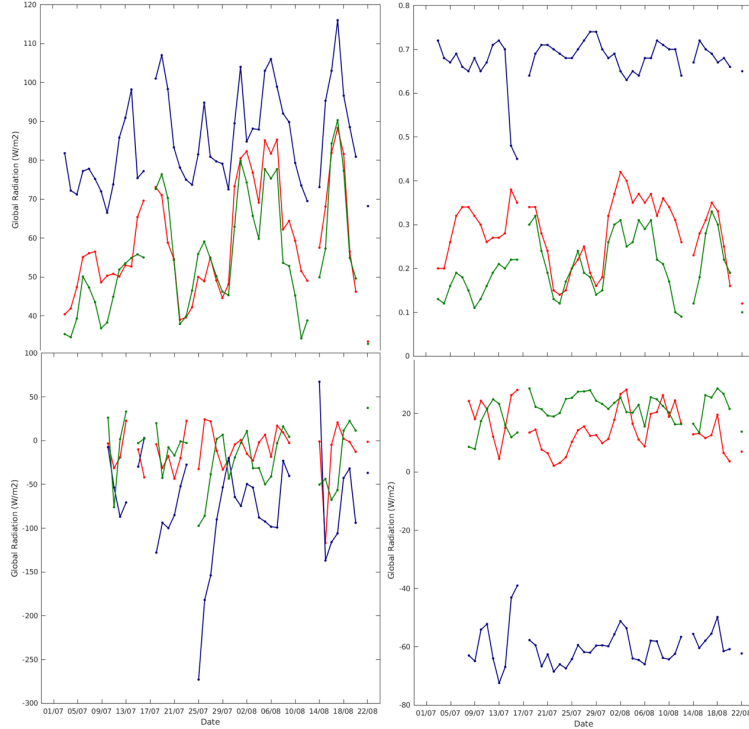
Figure 32: Global radiation results for three models: ECMWF-IFS with CAMS climatology (red), COSMO operational scheme with Tanre climatology (blue) and CLOUDRAD with CAMS forecasted aerosols (green). For the period July-August 2019 in IMS operational domain and is verified against 17 ground based stations in Israel. Upper left: global radiation RMSE [W/m^2], upper right: occurrences of fiascos where model error was larger than 50 W/m^2, lower left/right: cloudy/clear skies global radiation bias [W/m^2].

7.4 CAMS aerosols indirect effect on radiation

7.4.1 Water droplets number concentration and effective radius

The effective size and number concentration of water droplets significantly affect the cloud optical thickness. Fig. 4a shows that for the same total water path, changing droplets number concentration (tuning parameter cloud_num_rad) from 500 cm^{-3} ($R_{eff} \approx 4\ \mu m$) to 50 cm^{-3} ($R_{eff} \approx 9\ \mu m$) can change the global radiation on the surface from ~300 W/m^2 to ~450 W/m^2. In the operational radiation scheme (iradpar_cloud = 1) the effective size is defined by the formula: $R_{eff} = c_7 + c_8 LWC$ (Ritter and Geleyn 1992) without an explicit dependency on number concentration. The effective radius in the new CLOUDRAD scheme (iradpar_cloud = 4) is calculated from the number concentration following the formula:

$$R_{eff} = c_1 \left(\frac{LWC}{n_c} \right)^{c_2} \tag{27}$$

Where n_c is the cloud droplets number concentration and $c_{1,2}$ are coefficients related to the particle size distribution used by the microphysical scheme.

Formula 27 is used for grid scale clouds. For sub-grid scale (SGS) clouds, LWC is by definition zero. In the default radiation scheme, a tuning parameter (luse_reff_ini_x_as_reffx_sgs) is used

to define a fixed effective radius for SGS clouds and the tuning parameter for this background effective radius is reff_ini_c (default 5 μm). In the new CLOUDRAD scheme we added the option of calculating SGS effective radius in the same way done by grid scale clouds by setting luse_reff_ini_x_as_reffx_sgs=.FALSE.. In this case, formula 27 will be used with a special treatment to LWC as was discussed in Sec. 5.

Unlike the default radiation scheme where the chosen value for cloud_num_rad is effective at each cloudy grid box (default value 200 cm^{-3}), the new CLOUDRAD scheme (iradpar_cloud = 4, cloud_num_type_rad = 1) the number concentration is defined by setting cloud_num_rad as the value for cloud base and decreasing according to the vertical profile formula:

$$\mathrm{n}_c = \mathrm{n}_{c0} \cdot exp\left(-\frac{z - z_0}{\Delta z_{1/e}}\right) \tag{28}$$

Where z_0 is the cloud base height (tuning parameter zref_cloud_num_rad, default value 2000 m) and $1/\Delta z_{1/e}$ is the rate constant (tuning parameter dz_oe_cloud_num_rad , default 6000 m). n_{c0} is defined by the tuning parameter cloud_num_rad.

7.4.2 Water droplets activation using Segal and Khain (2006) scheme

In numerous studies it was shown that cloud droplets number concentration depends on aerosols concentrations (Segal and Khain, 2006, SK2006 hereafter) since the aerosols serve as condensation nuclei according to Kohler theory. In pristine atmosphere (i.e. in the Pacific Ocean) the aerosols number concentration is relatively small hence the cloud droplets number concentration is small and the cloud droplets effective radius is large. In a polluted atmosphere, cloud number concentration is higher. The limited humidity is spread on more particles resulting smaller droplets and optically thicker clouds. Using a simplistic estimations of cloud number concentrations based on fixed values at cloud base is unrealistic in most cases. In the new CLOUDRAD scheme we added the SK2006 activation scheme for cloud formation parametrization even in the 1-moment microphysical scheme (cloud_num_type_rad = 2). Segal and Khain (2006) used LES simulations with 2000-bin microphysics to parametrize cloud number concentrations as function of both vertical velocity at cloud base and aerosols size distribution. SK2006 is suitable for both stratiform and cumulus clouds in maritime, continental or extreme continental environments. They showed that the aerosols soluble concentration is the dominant factor in the resulted CCN concentrations. the realization of SK2006 in COSMO is by using 4D LUT to define n_c at cloud base using 4 parameters:

$$\mathrm{n}_{c,CB} = \mathrm{f}(\mathrm{N}_{CN,CB}, \; log\sigma_{CN}, \; r_{CN}, \; w_{CB}^{eff}) \tag{29}$$

where σ_{CN} and r_{CN} are the geometric standard deviation and mode radius of the aerosols lognormal distribution (see Eq. 26), N_{CN} is the aerosols number concentration at cloud base which can be taken from CAMS (itype_aerosol = 4) or Tegen climatology (itype_aerosol = 2). w_{CB}^{eff} is the effective updraft speed for nucleation at cloud base.

When Tegen aerosols are used, the lognormal distribution parameters are fixed to the values $\sigma_{CN} = 0.3$ and $r_{CN} = 0.0335 \; \mu m$. Aerosols number concentration for each of the species in Tegen climatology (dust, organic matter, sulfate and sea salt) are computed from optical depth assuming vertical exponential profile confined in the space between COSMO topography and 12 km height (the original Tegen topography is unavailable). The total N_{CN} is a summation over all species but with the soluble fraction consideration where dust soluble fraction is 0.9 and organic matter 0.9. Sulfate and sea salt are considered 100% soluble.

If CAMS aerosols are chosen as input for SK2006 activation scheme (cloud_num_type_rad = 2; itype_aerosol = 4), effective parameters for the lognormal distributions for the mixture of aerosols need to be calculated at each grid point. Weighted soluble particles number concentration $\overline{N}$, effective mode radius $\overline{r}$ and standard deviation $\overline{\sigma_g}$ are calculated according the formulas:

$$\overline{N_{CN}} = \sum_i N_i s_i \tag{30}$$

$$\overline{r} = \frac{1}{\overline{\overline{N}}} \sum_i N_i s_i r_i \tag{31}$$

$$\overline{\sigma_g} = \sqrt{\frac{1}{\overline{\overline{N}}} \sum_i N_i s_i \left[\sigma_{g,i}^2 + (r_i/\overline{r})^2 \right]} \tag{32}$$

where r_i, $\sigma_{g,i}$, s_i are the mode radius, geometric standard deviation and the soluble fraction of each aerosol specie i detailed in Table 26. N_i are the number concentrations at each grid point for each species which are calculated from the 3D mixing ratios, $w_{a,i}$ $[kg \cdot kg^{-1}]$, provided by CAMS for each time step and each grid point:

$$(7.8) N_i(x, y, z) = w_{a,i}(x, y, z) \cdot \rho_{air}(x, y, z) / \overline{m_{v,i}}$$

where $\overline{m_{v,i}}$ are the mean (volume) particle masses of each aerosol tracer (see Eq. 26 and Table 26).

The appropriate vertical velocity for aerosol activation should be representative of adiabatic and diabatic cooling within updraft regions to parametrize supersaturation build-up during cloud condensation:

$$w_{eff} = \overline{w} + 0.7 \sqrt{\frac{2TKE}{6}} - \frac{c_p}{g} \frac{\partial T}{\partial t} \tag{33}$$

Where $\overline{w}$ is the vertical velocity at cloud base, the middle term is the turbulence term and the third is the equivalent adiabatic updraft speed from radiative cooling.

For convective clouds, the option for imposing surface-based convective velocity scale as a lower limit diagnosed from convective cloud cover and theta-profile is implemented (name list parameter lincl_wstar_in_weff = .true.):

$$w_{CB}^{eff} = \max(w_{eff}, \ w^*) \tag{34}$$

$$w^* = \left(-g z_{topcon} \frac{\overline{w'\Theta'_{v,s}}}{\overline{\Theta'_{v,s}}} \right)^{1/3} \tag{35}$$

where z_{topcon} is the upper boundary of the convective PBL, Θ is the virtual potential temperature at PBL height (Deardorff, 1970).

As mentioned before, the cloud droplets number concentration is calculated at cloud base height which is diagnosed by scanning each column from bottom to top for first grid box with positive LWC or positive convective cloud cover. From this point and higher an exponential

profile decay is imposed using formula 28. If the effective updraft above cloud base is larger than the updraft calculated at cloud base (not a common situation), in-cloud nucleation is considered and the procedure detailed above is repeated but imposing the profile from half height between the cloud base and the actual height.

7.4.3   Using Segal and Khain (2006) scheme in the 1-moment microphysics

So far we discussed the direct and indirect effects of aerosols on radiation. In reality, the first and most important impact of aerosols is on cloud nucleation and dynamics. Clouds are the first factor effecting the radiation fluxes in the atmosphere covering roughly half of earth's surface. On the other hand, the very existence of clouds depends on the presence of aerosols. In pristine environments the cloud number concentration is usually low and the droplets are large. This will allow precipitation in the early stages of the cloud life which may suppress further development of the clouds to sever thunderstorms. In such situations, stratiform precipitation is expected and in cold temperatures, snow. In polluted environments higher cloud number concentrations are expected. In a humid environment, the droplets will grow slowly and can delay cloud formation and allow energy build up with stronger updrafts at later stages of cloud life (Rosenfeld et al., 2008). As a result, thunderstorms can develop with liquid and ice (graupel and hail) precipitation is possible. Nevertheless, extremely polluted environments results very high cloud number concentrations results in very small droplets which evaporate hence cloud formation is prevented (Rosenfeld et al., 2008).

In COSMO 1-moment microphysical scheme a size distribution is assumed and the mass fraction q^x can be predicted. The microphysical processes are determined by q^x. Cloud number concentration n_c is explicitly used only in the autoconversion rate parametrization (Seifert and Beheng ,2001)

$$\text{S}_{au} = \alpha \cdot q_c^4 / n_c^2 \tag{36}$$

$$\alpha = \frac{k_c}{20x^*} \frac{(\nu + 2)(\nu + 4)}{(k_c + 1)^2} \tag{37}$$

Where S_{au} is the transfer rate due to autoconversion of cloud water, x^* is the separating mass between cloud and rain, k_c is the kernel coefficient for autoconversion and ν is the gamma exponent for cloud distribution. In the default COSMO 1-moment scheme n_c is a constant tuning parameter (default cloud_num = 500 cm^{-3}). In the new CLOUDRAD scheme n_c can be calculated as was described in details for the radiation in the previous section using the name list parameter icloud_num_type_gscp = 2. Here again, n_c will be calculated with SK2006 parametrization with Tegen climatology (itype_aerosol = 2) or CAMS forecasted aerosols (itype_aerosol = 4) as input aerosols for SK2006.

7.4.4   Case study - April 25-27, 2018

We examined the new CLOUDRAD radiation and microphysical scheme with CAMS aerosols and Segal & Khain droplet activation scheme using the event of 25-27/04/2018. In these three days of stormy weather in Israel, massive storm cells developed causing flush floods which caused the death of 14 people. Among them, 10 teenage hikers in the Eastern Negev on April 26, 2018. A low pressure system evolved in the Sinai Peninsula moving east (see

Fig. 33). Hot and humid air in lower layers along with cold air in the upper atmosphere caused extreme unstable atmosphere.
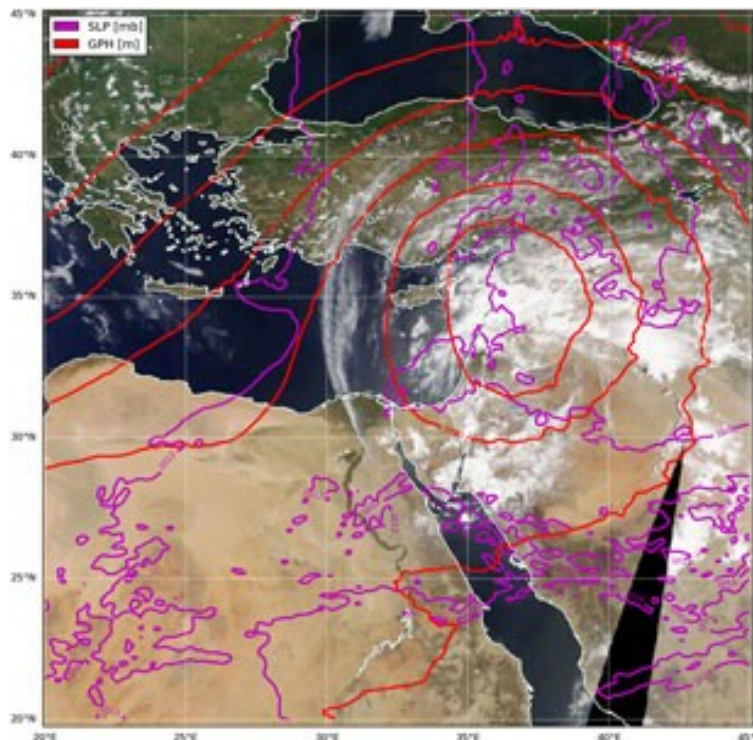

Figure 33: Synoptic analysis 26 April 2018 at 12:00 UTC, MODIS True Color RGB over Eastern Mediterranean. Red lines represents ECMWF analysis. Courtesy of Elyakom Vadislavsky.

The examination of CAMS aerosols cross sections for this highly convective event, reveals a diurnal cycle. The aerosols in all three days of the event are drifted upward by the convection at noon and descend at nights in a breath-like motion. A single snapshot of the event at April 25, at 14:00 UTC will be analysed here. Fig. 34 shows a cross section at 32N from 34E to 36 E from the Mediterranean Sea near Tel-Aviv to Amman in Jordan. The total hydrophobic aerosols concentration at cloud base heights (1000 m - 2000 m) reached 15000 cm^{-3} (Fig. 34 upper left panel) which is a typical number for polluted continental areas (Hess et al. 1998) especially in highly convective weather. Most of these hydrophobic aerosols are sulfate particles (lower right panel).
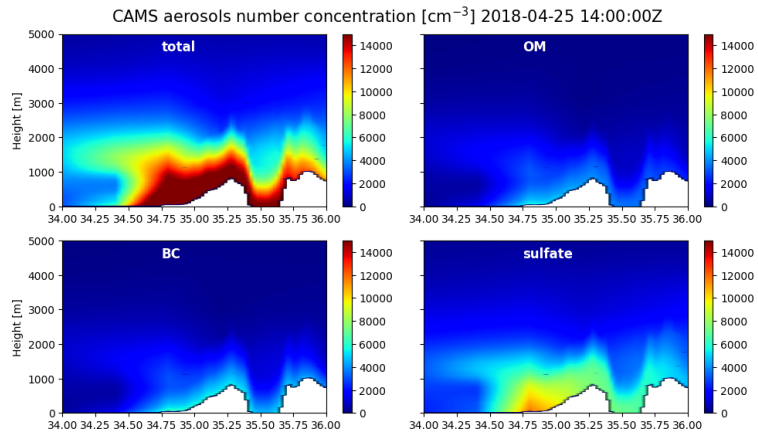
Figure 34: CAMS forecast for the 25th of April 2018 at 14:00 UTC. A cross-section at 32N going from 34E to 36E. Top left: total hydrophilic CAMS aerosols number concentrations, top right: organic matter, bottom left: black carbon and bottom right: sulfate concentrations.
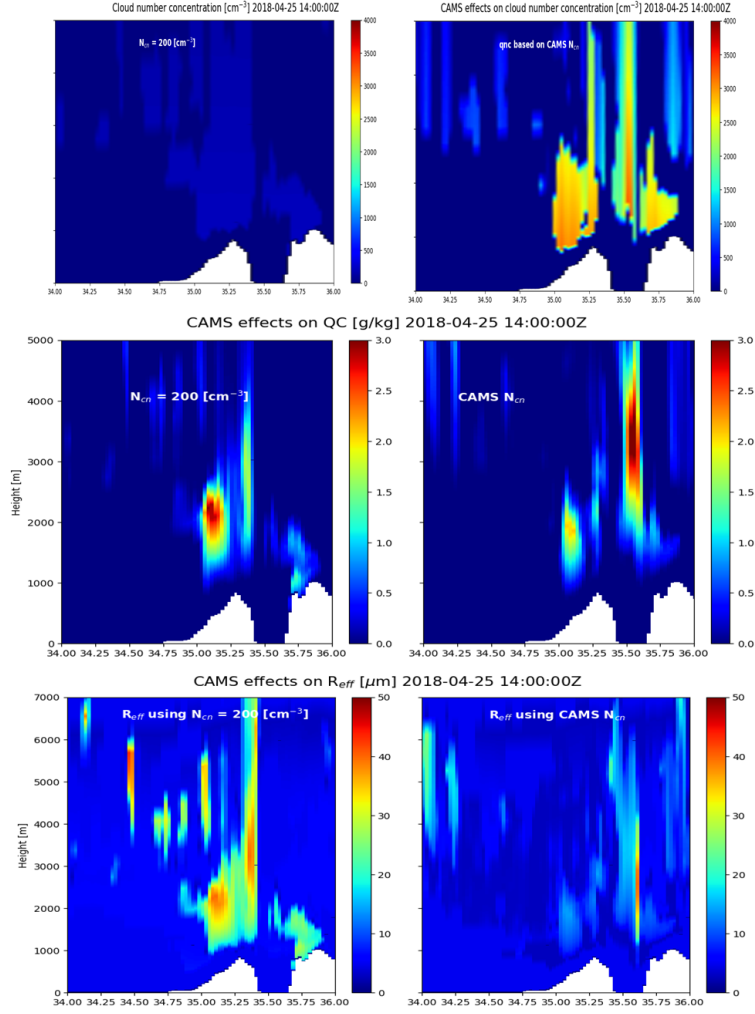
Figure 35: profiles for the 25th of April 2018 at 14:00 UTC. Left panels: cloud number concentration using fixed value (cloud_num_rad = 2.0E+08) at cloud base and an assumed vertical profile. Right panels: CAMS forecast aerosols as input for Segal & Khain 2006 cloud activations scheme. Upper row: cloud number concentration profile $[cm^{-3}]$, midle row: LWC $[g/kg]$, lower row: droplets effective radius $[\mu m]$. The "noodle" shape of cloud is a result of the horizontal and vertical scales.

Fig. 35 shows the results for two model setups. The left panels represents the fixed number concentration at cloud base of 200 cm^{-3} and using a profile as described in formula 28 (cloud_num_type_rad = 1, cloud_num_rad = 2.0E+08). On the right panels SK2006 droplets activation scheme with CAMS aerosols are displayed (cloud_num_type_rad = 2; itype_aerosol = 4). The upper panels display cloud number concentrations profiles. One can see that the number concentrations of cloud droplets above Judea and Jordan mountains when using prognostic aerosols and SK2006 activation scheme are significantly higher than other areas and also compared to the default scheme (left panel). It is a result of both high aerosols densities at this hour and large updraft speeds due to deep convection and high instability of the atmosphere. The cloud number concentrations are diagnostic and are effective only at grid boxes with positive LWC. The middle panels of Fig. 35 show the LWC profiles for these two models. The clouds location and water load are significantly different. For example, the massive clouds above the Dead Sea at 36E are not present in the default scheme and can cause extreme flash floods in this area. Lower panels show results for the effective radius.

The prognostic scheme results in much smaller droplets.

The lower panels of Fig. 35 explain the immense effect of using forecasted aerosols and realistic cloud activation on the radiation. The clouds droplets are much smaller and with much larger densities which lead to a significant increase in cloud optical thickness (see Fig. 4). In Fig. 36 the results for the entire domain is presented. The colours indicates the points occurrences in the domain. The first row shown the cloud number concentration as a function of aerosols concentrations when SK2006 scheme is used in all grid points (left) and at cloud base (right). The cloud number concentrations can reach numbers as high as $3000\ cm^{-3}$ which may seem too large. Nevertheless, close inspection reveals that most points at cloud base have cloud number densities less than $1000\ cm^{-3}$ with an average of $621\ cm^{-3}$, a reasonable value for highly convective and polluted environments. As expected, the high $n_{c,CB}$ numbers are achieved when effective updraft speeds w_{nuc} are high as can be seen in the middle row of Fig. 36. The effective vertical wind speeds at cloud base can reach $\sim 3m/s$ (middle row right figure) while in the rest of the domain, at higher altitudes, the updraft can climb to much higher values (middle row, left panel).

The first two rows of Fig. 36 associate only with the CAMS and SK2006 configuration while the third raw shows the results of the two models setups described in Fig. 35. The effective radius as function of LWC is plotted enlightening the conclusion drafted from the lower panels of Fig. 35. We can clearly see that using forecasted aerosols combined with parametrized droplets activation can lead to more realistic droplet sizes of $\sim 7\mu m$ for continental clouds (see i.e. Fig. 6 in Reid et al. 1999) while using a fixed cloud number concentrations can cause large mistakes in cloud effective size and as a result, large errors in cloud optical thickness.
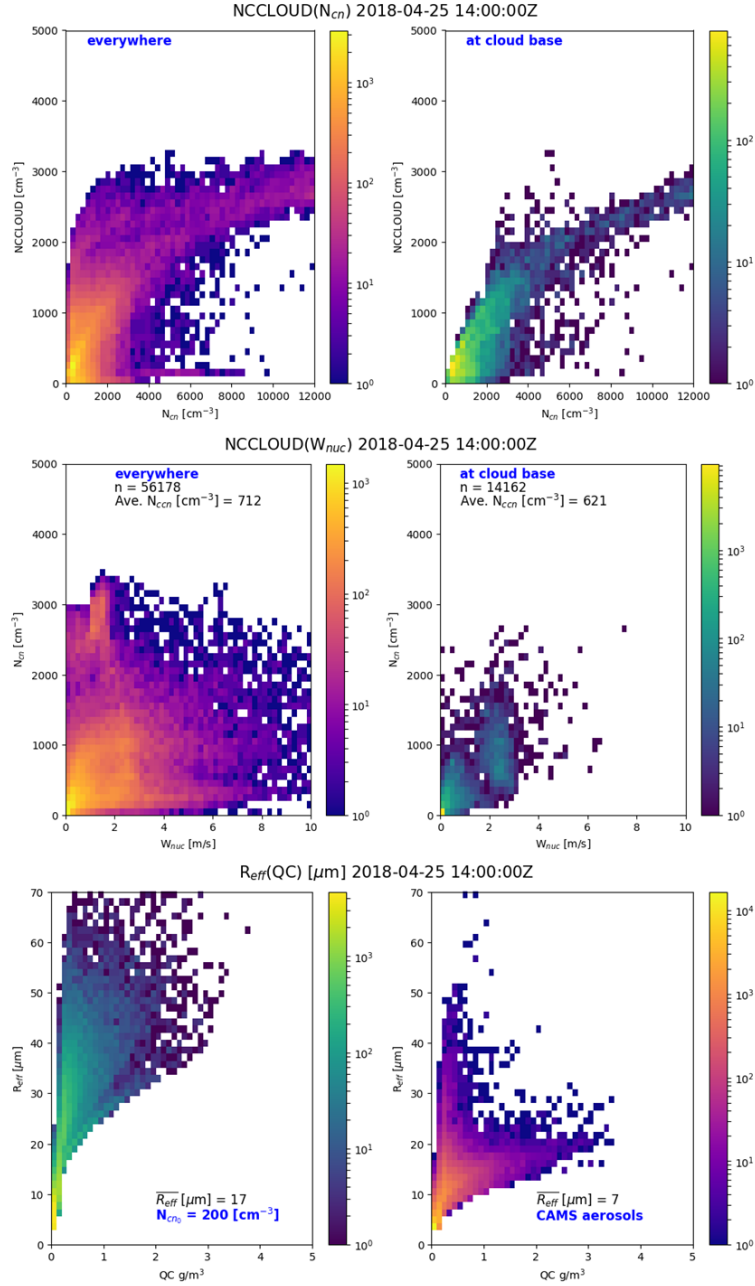
Figure 36: Upper row: droplet concentration as a function of aerosols number concentration $[cm^{-3}]$, middle row: droplet concentration as a function of effective updraft speed for nucleation $[m/s]$ (left: all points, right: at cloud base). Lower row: droplets effective radius $[\mu m]$ as a function of LWC [g/kg] (left: fixed droplet number concentration at cloud base, right: SK2006 activation scheme with CAMS forecasted aerosols.

In the previous sections we discussed the direct and indirect effects of the new SK2006 activation scheme radiation. While in Sec. 7.4.3 we discussed the influence of aerosols on the 1-moment microphysics scheme (on the auto-conversion rate). It can be done by using the name-list parameters icloud_num_type_rad/gscp in which setting each to the value of 2 will turn on the SK2006 activation scheme with the chosen aerosols input (Tegen or CAMS). The sensitivity of the model to each of these effects is presented in Fig. 37. For all four model configurations shown here, the aerosols input was CAMS (itype_aerosol =

4). The same test case was chosen but now the 11:00 UTC snapshot is taken to examine the effects on the maximum radiation at noon time. The upper four figures show incoming shortwave downward radiation on surface (global radiation) while the lower four show the 2m-Temperature. In each of these pair of four figures the upper left is for the new radiation scheme using fixed droplet number concentration (cloud_num_rad = 200 cm^{-3}) at cloud base icloud_num_type_rad/gscp = 1. In this configuration only the direct aerosols effect is activated. This setup will serve as a control run for which the absolute values are visualized. The other three figures shows the biases to the control run when we activate the indirect effects. Upper right panel represent the resulted bias due to turning SK2006 on but effective only in radiation (icloud_num_type_rad = 2). Lower left panel is the same but effective only in the microphysics (icloud_num_type_gscp = 2) and results when both effects are turned on icloud_num_type_rad/gscp = 2 are shown in lower right panel. The numbers on each of the three models are calculated over all model surface grid points compared to the control run in Wm^{-2} for the upper figures and K in the lower figures.

Analysis of these figures show that the indirect effect cloud droplets activation scheme on both radiation and microphysical schemes is significant. The biases of radiation/temperature can be as large as 300 Wm^{-2} / 3 K respectively. Although the RMSE and bias numbers appearing in each Fig. are a result of the average on all grid points where most of them are cloudless, these averages are unneglectable (bias ~ -7 Wm^{-2}, -0.04 K, RMSE ~ 70 Wm^{-2}, 0.35 K). As expected, the use of CAMS aerosols which have larger number concentrations in this test case, reduced the droplet effective radius compared to the default scheme which in turns reduced the radiation on surface and the 2m-temperature. Surprisingly, the use of realistic aerosols and cloud activation scheme effected the microphysics (auto-conversion rate) in a way that caused significant changes in radiation but with smaller absolute values (RMSE ~ 40 Wm^{-2}, 0.2 K). In this case, the radiation and temperature bias is almost zero since the effective radius of droplets was unaffected.
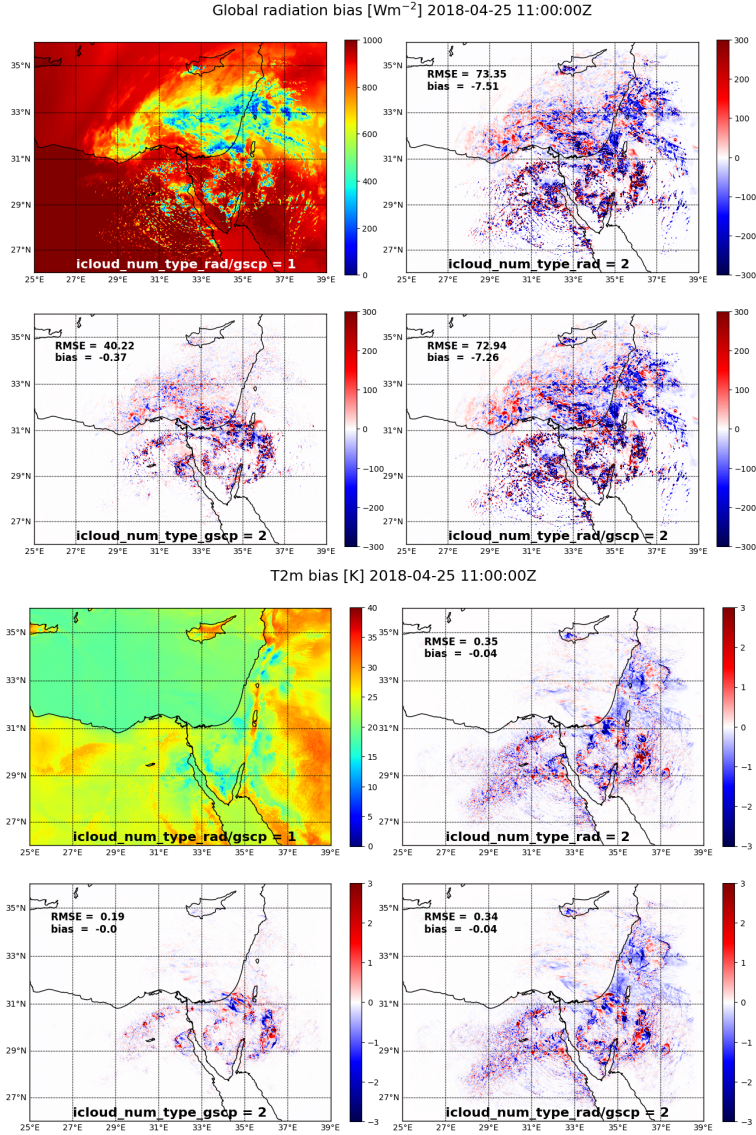
Figure 37: Global radiation (upper four figures) and Temperature (lower four figures) biases as a result of the indirect effects of SK2006 cloud activation scheme using CAMS forecasted aerosols. See text for details.

7.4.5 Ice nucleation scheme model inter-comparison using a case study

In Sec. 7.4.4, we showed the model results for the case study of 25-27-April-2020. In this chapter we will show the model sensitivity to the ice nucleation scenarios. The four models described in the previous section: the 1-moment scheme using Cooper (1986) parametrization (default), 1-moment microphysics using DeMott (2015) parametrization with CAMS dust forecasted fields, 2-moment microphysics with Phillips (2008) parametrization using fixed aerosols number concentrations and 2-moment scheme using CAMS 3D forecasted aerosols input. An example result of an atmospheric cross-section of IN concentrations for the 25-Apr-2020 14:00 UTC is presented in Fig. 38. We can see that the default Cooper (1986) scheme (upper left panel) underestimates IN concentrations compared with other models having no aerosols data as input. Fig. 39 presents the dust aerosols cross section for the same snapshot. The dust number concentration at ice cloud heights can reach a few tens

of dust particles per litter. As a result, high IN umber concentration can be seen in the DeMott (2015) parametrization (upper right) – the highest amongst all models. Since both ice supersaturation and the updraft speeds are not taken into account, high concentrations of ice cannot be seen in the cumulonimbus cloud formed at longitude 35°E. The 2-moment microphysics with Phillips (2008) ice nucleation scheme did simulate the formation of ice in this cloud at heights 4000-8000 meters where high vertical speeds and supersaturation values were found. Smaller number concentration were achieved using fixed aerosols concentration (lower left) compared to the forecasted CAMS input (lower right). The Phillips (2008) scheme also underestimated the IN concentration at cold temperatures ($< 240K$) compared to DeMott (2015) scheme. Fig. 40 displays the four models output of IN as a function of temperature for the same hour where brighter colours means higher occurrences in the domain for grid points with LWC > 0.03 g/m^3. The numbers inserts are the domain averages. The DeMott parametrization result at this snapshot has an average IN concentration of 401 $[1/L]$ which is a factor of 4 larger than the default Cooper scheme and a factor of 7-10 larger than the averages of the Phillips (2008) nucleation scheme. The effect of the IN concentrations on the effective ice particle size can be seen in Fig. 41 where the average ice particle size for the DeMott scheme is $18\mu m$ while the default 1-mom scheme using Cooper is $24\mu m$, Phillips (2008) default 2-mom scheme resulted averaged size of $74\mu m$ and the same scheme using CAMS aerosols average is $56\mu m$. The effects on the IWC itself can be seen in Fig. 42.
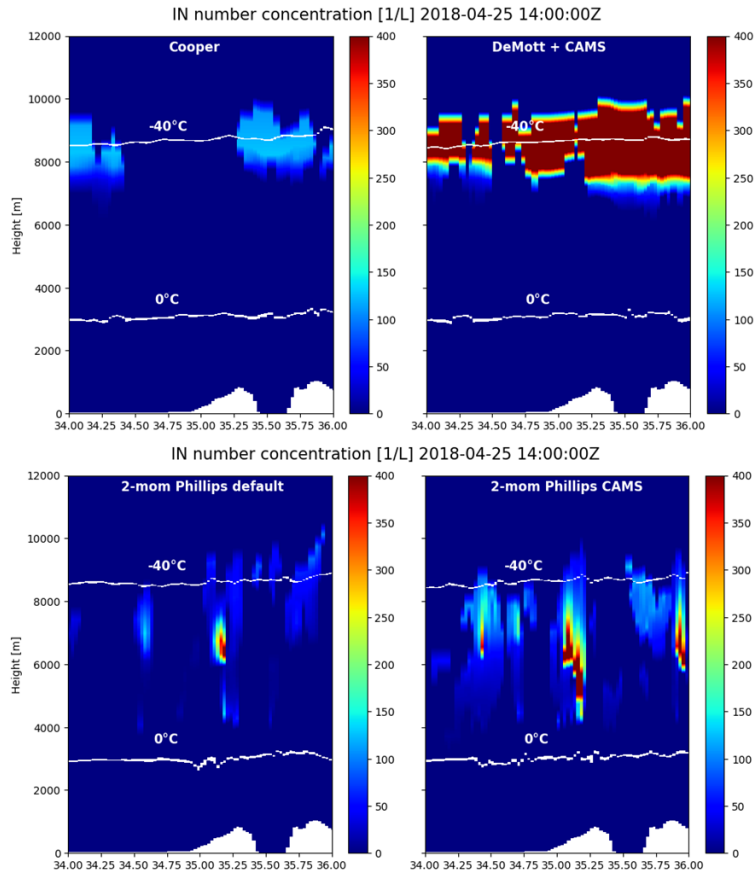
Figure 38: IN profiles in $[1/L]$ units for 1-moment microphysics using Cooper (1986) nucleation parametrization (upper left), 1-moment scheme using DeMott (2015) formulation using CAMS dust forecasted aerosols (upper right), 2-moment scheme using Phillips (2008) using default fixed aerosols number concentrations (lower left) and the same scheme using the 3D CAMS forecasted insoluble aerosols as input (lower right). The two white lines are the ice melting level and (roughly) the ice spontaneous freezing levels.
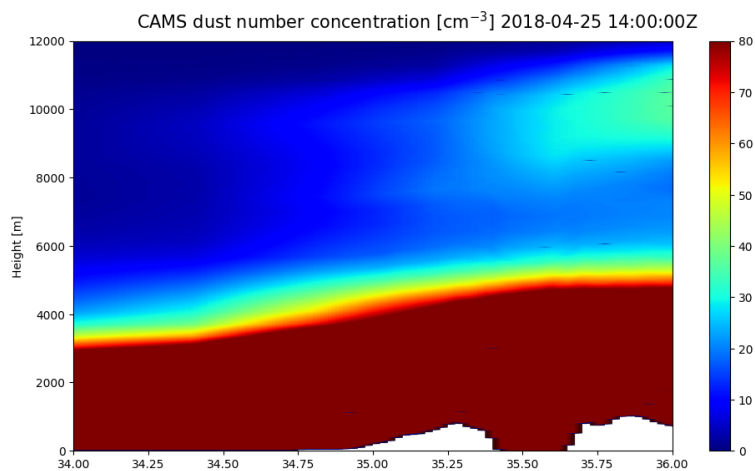
Figure 39: CAMS dust number concentration profiles forecasted for 25-04-2018 at 14:00. The scale was changed to emphasize the values at ice clouds heights (5000 m-10,000 m).
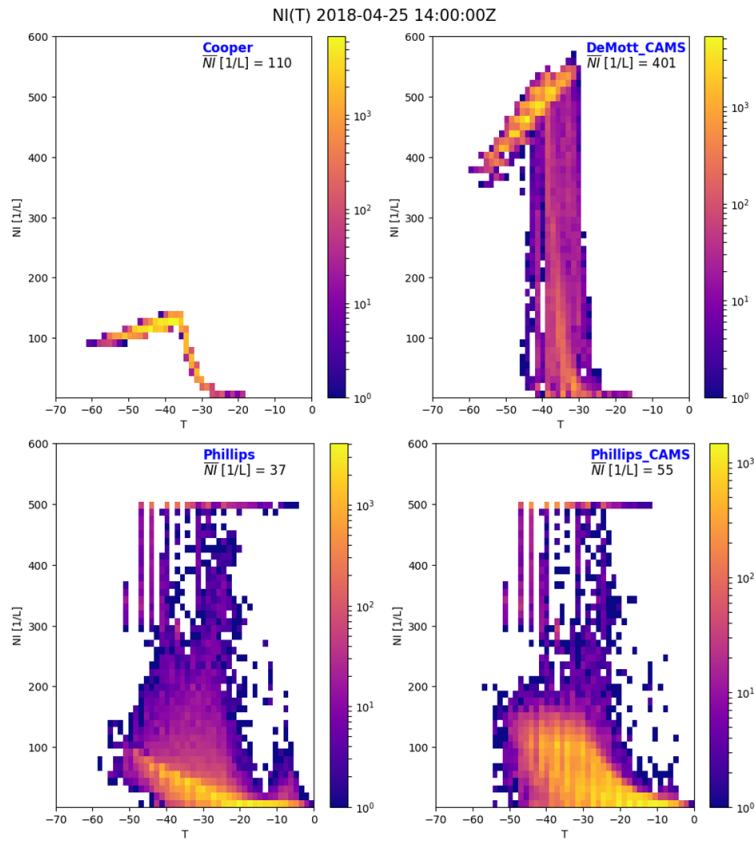
Figure 40: Occurrences plot for the IN concentration $[1/L]$ as a function of temperature for the same models described in Fig. 38. The number inside each panel represents the entire domain averages for grid point having non-zero ice content.
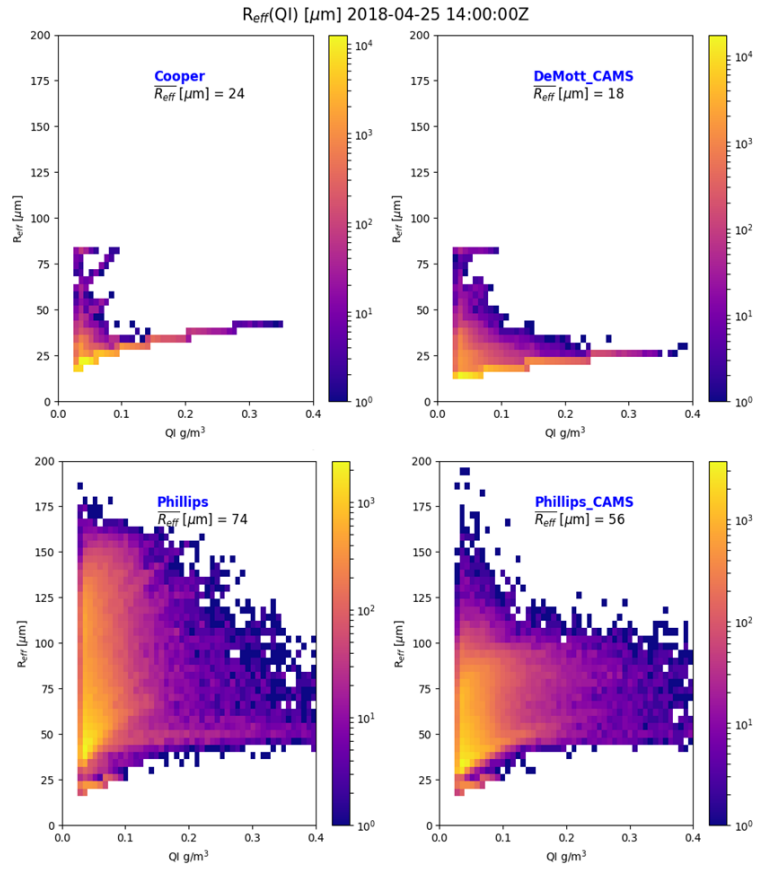
Figure 41: Occurrences plot for the IN concentration $[1/L]$ as a function of temperature for the same models described in Fig. 38. The number inside each panel represents the entire domain averages for grid point having non-zero ice content.
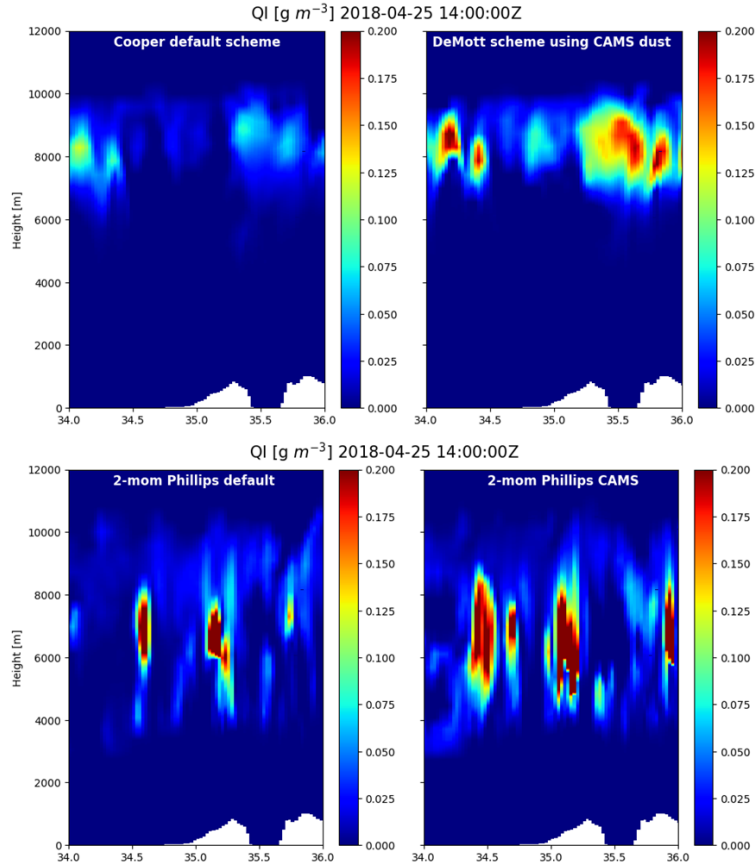
Figure 42: LWC profiles in [g/m^3] units for the same models described in Fig. 38.

7.4.6 DeMott (2015) ice nucleation scheme results vs. observational data

In order to statistically test the new DeMott (2015) ice nucleation scheme in COSMO using the CAMS forecasted dust field we performed 45 test cases runs in the IMS domain. The period chosen was in the October-November period and produced a 66-million points NI(T) plots as can be seen in Fig. 43. The upper left panel is for the default 1-moment COSMO microphysics using Cooper 1986 formula. In this plot of course, all points and the average (lime line) overlap. In the upper right panel the new DeMott & CAMS scheme results are presented. The scatter of points is due to the large divergence of dust particles densities. The averaged IN concentration for each temperature is in lime while point's colours visualize the occurrences in the domain. The same lime average line can be seen in the lower left panel but in a logarithmic vertical scale. The (schematic) blue line on this curve is copied on top of the plot in the lower right panel taken from Vergara-Temprado et al. (2018, with permission) which includes observational data from different locations around the globe. This shows that the new scheme implemented in COSMO fits the scattered points observed in terrestrial locations (red points).
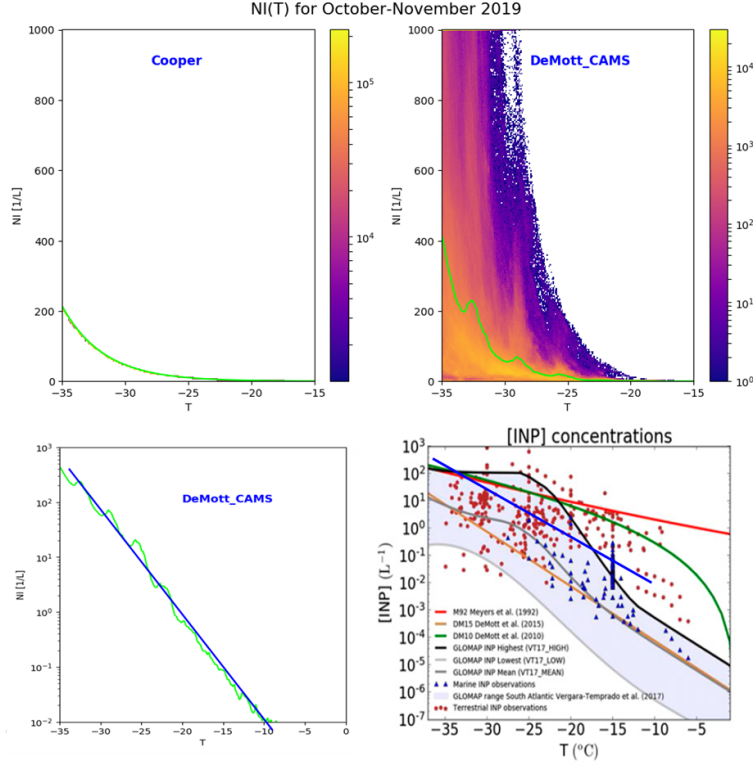
Figure 43: IN concentrations $[1/L]$ as a function of temperature for 45 test cases in the period of October-November 2019. Upper left: COSMO default ice nucleation scheme (Cooper, 1986), Upper right: COSMO new ice nucleation scheme using DeMott (2015) parametrization and CAMS forecasted dust concentrations, Lower left: the same but on a logarithmic scale, Lower right: observational data plot taken from Vergara-Temprado et al. (2018, with permission). See text for details.

8   Implementation of ICON-ART forecasted dust in COSMO radiation scheme

(H. Muskatel, D. Rieger, A. Shtivelman)

8.1   Introduction

ICON-ART is a global model system which online couples between ICON model (Zängl et al., 2015) and the ART modules for aerosols and reactive trace gases developed in KIT. The concentrations of the selected particles are calculated in every time step and synchronized with the NWP model dynamics.

COSMO model new CLOUDRAD radiation scheme has five options for aerosols input: Tanre climatology (Tanre et al., 1984, itype_aerosol = 1), Tegen climatology (Tegen et al., 1997, itype_aerosol = 2), MACv2 climatology (Kinne et al. 2013, itype_aerosol = 3), CAMS forecasted aerosols (Morcrette et al. 2009, itype_aerosol = 4) and now also ICON-ART-dust forecasted aerosols (itype_aerosol = 5). The details on ICON-ART model and especially dust forecast are discussed in Zängl et al. (2015), Schröter et al. (2018) and Gasch et al. (2017).

This semi-operational model, runs twice a day on global scale in DWD, currently including only three dust tracers but more aerosols species are planned for the future. As explained in the previous chapter regarding CAMS forecasted aerosols, the aerosols densities from the global aerosols model for every hour are interpolated in space and time by INT2LM over the whole domain. Since only dust forecast is available on a daily basis in ICON-ART, other four species of aerosols for the ICON-ART-dust option (itype_aerosol = 5) are taken from Tegen climatology (sea salt, organic matter, black carbon and sulfate).

8.2   ICON-ART dust aerosols direct effect on radiation

The direct effect of ICON-ART dust forecast on COSMO radiation was verified against ground-based measurements stations as detailed in Sec. 7 (see Fig. 28) and also 4 AERONET stations in Technion (Israel Institute of Technology in Haifa), Wiezmann Institute of Science (Rehovot), Sede-Boker and Elat. The time period selected was October-November 2018 and April-May 2019. These autumn and spring seasons in Israel region are very active in terms of dust outbreaks. The three COSMO-CLOUDRAD models aerosols inputs versions were: Tegen (1997) climatology, CAMS forecasted aerosols and ICON-ART-dust forecasted dust. The two variables which were evaluated were the downward shortwave radiation (global radiation) and the aerosols optical depth (AOD) at 500 nm. The global radiation in all skies conditions in all stations combined are presented in Fig. 44. The black 1:1 line represents the ideal model-observation match. The red/green lines are the linear fit to the model-observation scatter plot. Points located far from the black line means fiascos of radiation forecast and usually are due to cloud cover or cloud optical depth errors. Fig 45 is similar to Fig. 44 but for clear skies conditions. The clearness of the skies were defined as points for which all three models agreed on cloud cover less than 10%.
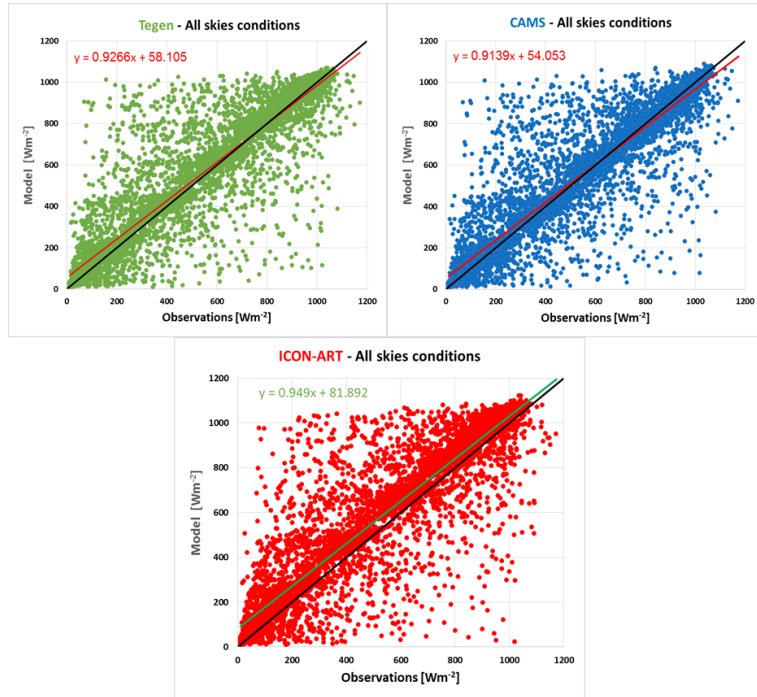
Figure 44: Global radiation model vs. observation for 10 ground based stations in Israel. For the period Oct-Nov-2018 & May-Apr-2019. All skies conditions at all grid-points and hourly snapshot time steps. Upper-left: CLOUDRAD scheme using Tegen climatology, upper right: CAMS forecasted aerosols, lower panel: ICON-ART-dust. Black line: 1:1 ideal match, red/green line: linear fit of the model-observation couples.
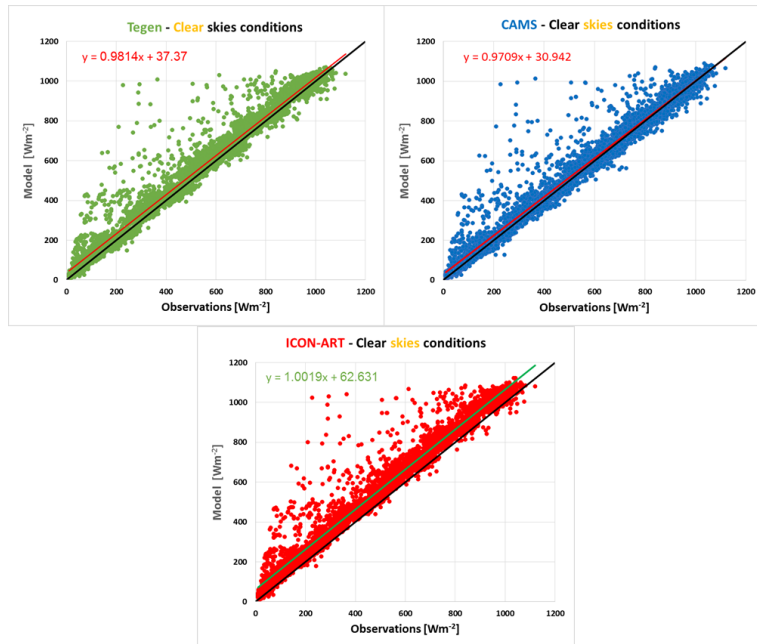
Figure 45: Same as in Fig. 44. For clear skies conditions defined for grid points in space and time for which at all models the total cloud cover was less than 10%.
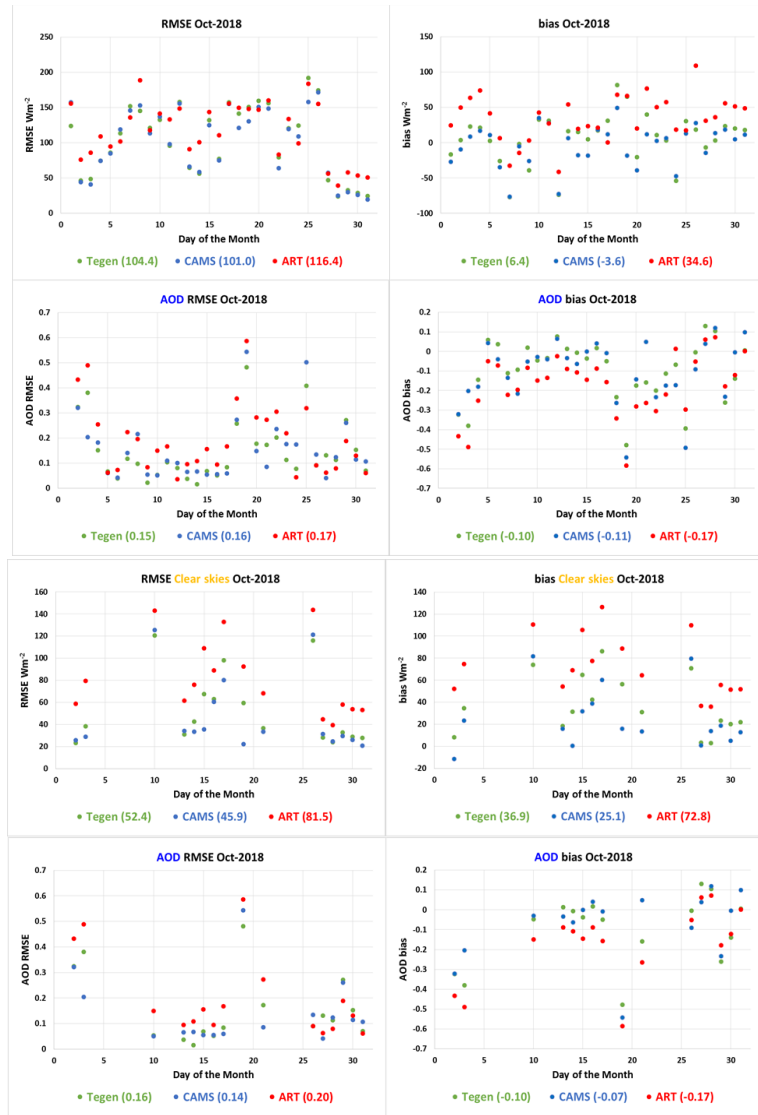
Figure 46: See text for details.

Figure 47: See text for details.
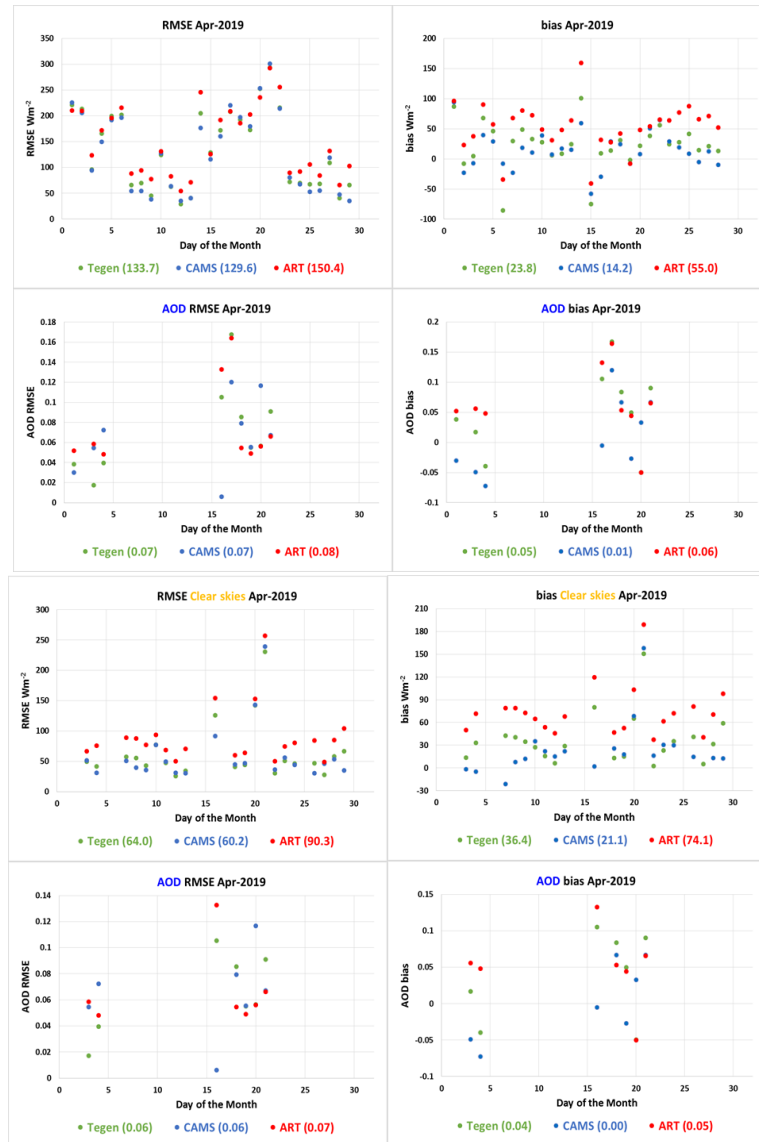
Figure 48: See text for details.

Figure 49: See text for details.

The results shown in Fig. 44 reveals the difficulty to forecast radiation fluxes without first having an accurate cloud cover estimation. Nevertheless, when observing the errors in 2-meter temperatures (not presented here) we see that usually the effect on surface temperature is in the order of 0.1 K. This is due to the fact that even when the cloud cover at a specific time step/grid point is wrong, the averaged fluxes over few minutes/hours are usually accurate when the overall synoptic situation is correctly forecasted. The clear-sky condition results shown in Fig. 45 reveals systematic errors in the models (apart from the outliers above the black line which are associated with clouded points not forecasted by the model). We can see that COSMO using Tegen climatology has a small radiative positive bias (negative AOD bias) which is more significant in the mornings and afternoons. CAMS forecasted aerosols linear fit red line almost overlaps the black line which means that the bias is very small during the whole day. On the other hand, ICON-ART-dust (with Tegen four other aerosols species) shows the poorest results with fixed positive bias which means that there is a negative bias in dust optical depth throughout the day. That may point to a systematic error in the dust forecast that may be a regional issue. Israel is in the midpoint between

76

two of the most significant dust emissions sources in the world – the Sahara Desert and the Arabian Peninsula. A systematic error due to a calculation error (code bug) is also a possibility which is being investigated.

Figs. 8.3 are subdivided into 4 pages, each page relates to a different month. In each page, the four upper plots represents the all-skies condition results and the four lower panels represents the clear-skies conditions points. Each point is a daily average value (over all stations and time steps of that day). For each 4-panels group, the upper-left/upper-right panels are the global radiation RMSE/bias averages and the lower-left/lower-right panels are for the AOD RMSE/biases. The monthly average values appear as coloured numbers under each plot. In October and November 2018, All models have a small negative AOD bias. Both radiation and AOD scores are very similar for both Tegen and CAMS forecast. CAMS results are slightly better with almost zero AOD bias in clear skies conditions. Unfortunately, the RMSE and bias is worsen when using ICON-ART-dust forecast. Although having similar AOD biases with Tegen, ICON-ART-dust has still much larger positive fluxes biases (~ 30 W/m^2) which needs further code investigation. In April 2019 all models showed an averaged positive AOD but still a positive radiation fluxes compared to the observations while in May 2019 only ICON-ART-dust showed a positive AOD bias. For these months as well, CAMS forecast had the best scores, second is Tegen climatology and third comes ICON-ART. The radiation RMSE are, as expected, larger for all-skies conditions (~ 100 W/m^2) compared with clear skies condition (~ 50 W/m^2) due to cloudiness but with much higher values for ICON-ART-dust compared with other models. This gap can be associated with the fixed positive bias in radiation when using the ICON-ART-dust aerosols. The RMSE for CAMS model is on the average $\sim$10-15 W/m^2 smaller compared to Tegen climatology RMSE due to the data assimilation and dynamical forecast of aerosols compared with the monthly mean values taken from Tegen (1997). We believe that in the future, such forecasted aerosols from ICON-ART or CAMS systems can be used also in the ICON model in both LAM or global modes of operations.

9   Verifications of the new COSMO radiation scheme in clear skies and cloudy skies conditions

(N. Chubarova, M. Shatunova, A. Poliukhov, A. Kirsanov, G. Rivin)

9.1   New MACv2 aerosol climatology and its verification in clear sky conditions

9.1.1   MACv2 aerosol climatology

The MACv2 climatology (Kinne, 2019) takes into account recent developments in aerosol modelling and experimental data and is a combination of the model ensemble data and ground-based aerosol measurements from AERONET dataset. It provides all necessary aerosol input parameters for the radiative computations in different spectral intervals for fine and coarse aerosol modes. It is also possible to retrieve an anthropogenic aerosol mode from this climatology. MACv2 aerosol climatology has monthly temporal resolution and provides 1°x1° spatial fields for wavelengths of 0.29, 0.32, 0.55, 0.87, 1.47, 2.0, and 2.6 μm in the solar spectrum and wavelengths 7, 8.85,9.75, 11.2 and 30 μm in the longwave range. An averaging procedure was performed to fit these wavelengths to COSMO 8-band radiative transfer model.

To include this aerosol climatology into the COSMO system we made the changes for the following blocks: EXTPAR, INT2LM and COSMO model. Unlike Tegen climatology (Tegen et al., 1997), receiving of all aerosol optical and radiation properties goes through EXTPAR, when using MACv2 climatology. Aerosol optical thickness (AOT), single scattering albedo (SSA) and asymmetry factor (ASI) values were normalized to the corresponding values at 550 nm and recorded in four-dimensional arrays: longitude, latitude, month and spectral interval.

9.1.2 Comparison with Tegen climatology and in-situ observations

We compared aerosol optical thickness (AOT), single scattering albedo (SSA) and asymmetry parameter (ASI) from the new MACv2 climatology as well from Tegen climatology with long-term measurements of AERONET at the Meteorological Observatory of the Moscow State University (further MSU MO or Moscow site) and AERONET/PFR data at the Lindenberg Observatory.

We used radiative measurements by Kipp & Zonen CNR-4 net radiometer at Moscow and by the BSRN (Baseline Surface Radiation Network) type of radiative instruments at Lindenberg. We focused mainly on the measurements of global solar irradiance. However, for obtaining surface albedo we also used reflected shortwave irradiance. Water vapour retrievals were also obtained using AERONET algorithm at 940 nm channel. In addition, we used upper – air soundings (temperature, water vapour) at both sites as well as Ozonesonde dataset - at Lindenberg. At Moscow air temperature measurements at 2 meters were analysed using routine observations and Vaisala automatic weather station. At Lindenberg the data from the automatic weather station were used. In order to reveal clear sky situations we used hourly visual observations at both sites.

AOT550 time series according to long-term measurements at the MSU MO (Abakumova et al., 2008, Chubarova et al., 2016) and MACv2 dataset are presented on Fig. 50. While AERONET data for Moscow site are available from 2002, AOT restored values from direct shortwave irradiance allowed to make comparison for the 30 years period. Increasing in AOT values are corresponded to eruptions of El-Chichon in 1982 and Pinatubo in 1991 and forest wildfires in 2002 and 2010. It is obvious that climatology does not take into account sharp random changes in AOT or other optical parameters. However, MACv2 data is in good agreement with point observations and demonstrates the same tendency in AOT decreasing during last 30 years.

MACv2 and Tegen climatologies overestimate AOT during most months at the both sites. SSA values from Tegen climatology practically do not vary throughout a year, while MACv2 SSA variations are closer to the observed values except winter when one can see noticeable overestimation for MACv2 data. Detailed comparison of MACv2, Tegen climatology data with in-situ observations for Moscow and Lindenberg sites presented in Chubarova et al., 2018 and Poliukhov et al., 2018.
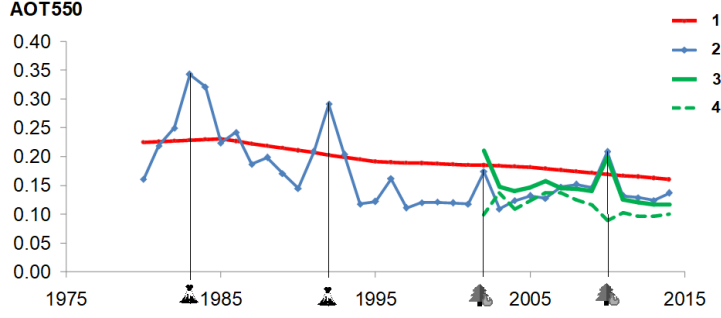
Figure 50: Comparison of aerosol optical thickness at 550 km from MACv2 climatology (1) with restored values from direct shortwave irradiance (2) and AERONET data mean (3) and median (4) values for MO MSU, Moscow.

In addition, the comparison for aerosol properties from Tegen and MACv2 climatologies against ground-based measurements over Israel in Eilat site with prevailing mineral type of aerosol, and over Arctic at the Tiksi Observatory in Russia have been performed. The results are described in Poliukhov et al., 2019.

9.1.3   Radiation fluxes assessment

To account the changes in all the aerosol properties (AOT, SSA, ASI) we chose global shortwave irradiance at ground as an aggregated characteristic. The comparisons between simulated and observed global solar irradiance datasets were fulfilled for different aerosol conditions and solar zenith angles for clear sky condition using accurate model simulations which were compared with solar measurements.

Using the obtained aerosol parameters from the climatologies and the observations we calculated global solar irradiance (Q) at ground and the corresponding difference $\Delta Q = Q_{climatology} - Q_{obs}$ (see Fig. 51). Radiative simulations were fulfilled using a modified CLI-RAD radiative transfer code (Tarasova and Fomin, 2005) for noon conditions at the central day of a month. Results for Moscow (Fig. 51a) shows that Tegen climatology Q values were underestimated with a negative bias of 11-26 W/m^2 while for MACv2 Q bias varies from -23 to +4 W/m^2. The annual mean bias for the MACv2 climatology, -10.8 W/m^2, is closer to the observations compared with Tegen climatology having bias of -17.3 W/m^2. For Lindenberg site, both climatologies provide underestimation of global solar irradiance of about -10 W/m^2 for annual means compared with the Q values simulated with the aerosol input parameters taken from observations. Both of them have lower solar irradiance for almost all months mainly due to the overestimated AOT. At the same time, for the Tegen climatology in April and November in conditions with only small AOT overestimation (ΔAOT = 0.01-0.02) we observe even positive bias in solar irradiance (1-2 W/m^2) due to the large difference in SSA. For these months Tegen climatology provides much higher SSA values (0.92) compared with the observations (0.85). For Tegen climatology, 10-20 % of aerosol optical thickness over Europe relates to black carbon aerosol, which should significantly increase the absorption especially in visible spectrum. However, this is not enough to explain the lower SSA values observed at Moscow site, which probably occur due to smaller aerosol size.

A positive bias of AOT results in the underestimation by 2-3 % in global solar irradiance simulated by COSMO radiative algorithm for Moscow and Lindenberg sites (Chubarova et al., 2018; Poliukhov et al., 2018). Nevertheless, for some polluted cases the situation

may differ (Fig. 51). A sharp increase in the concentration of pollutants observed on 21 November 2014 in Moscow resulted in the difference between observed and simulated global radiation. AOT550 AERONET values reached 0.17-0.20, AOT055 according Tegen and MACv2 climatologies was similar – 0.17. However, there was a high concentration of NO2 (Fig. 51c) and possible additional absorption in visible region of spectrum due to this gas. In this case radiative transfer simulations made with Tegen and MACv2 data show large overestimation compare to observations. It is interesting that simulations with the former Tanre climatology (Tanre et al., 1984) show the best agreement with observations in this particular case.
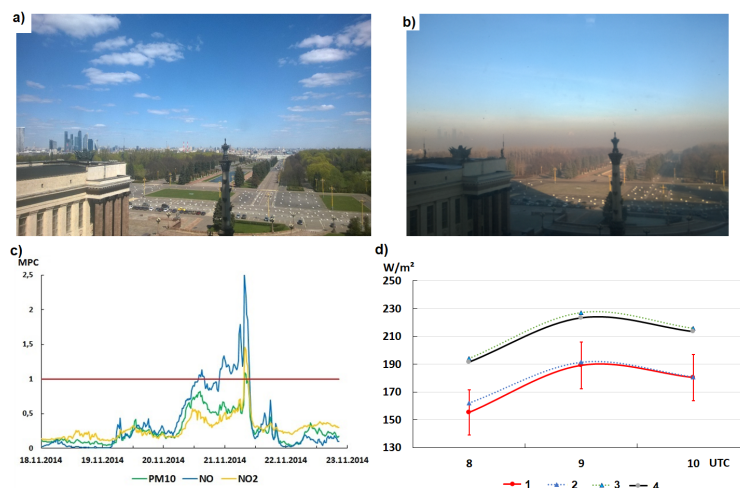

Figure 51: An example of polluted case: view over Moscow city on a) 17 November 2014 and b) 21 November 2014; c) observed level of pollutant concentration; d) observed (1) and simulated global radiation with Tanre (2), Tegen (3) and MACv2 (4) climatology data.

9.1.4 Temperature sensitivity to the changes in aerosol characteristics

The instant temperature effects of aerosol were analysed using different COSMO model runs with different aerosol climatologies and with zero aerosol conditions for the same clear sky days which are used in the analysis. Since aerosols over continental Europe are characterized by weak absorption in visible spectral range, it should provide the negative effect on temperature at ground level. To account the changes in all the aerosol properties (AOT, SSA and asymmetry factor) we chose net shortwave irradiance at ground as an aggregated characteristic. Net shortwave radiation is the difference in downwelling and upwelling shortwave irradiance and it also accounts for surface albedo effects, which play, however, minor role in our snow-less conditions. We analysed the dependence of difference in air temperature at 2 meters (ΔT) simulated in conditions with and without aerosols to the corresponding difference in net radiation (ΔB) to estimate the temperature sensitivity to aerosol. The negative values in net radiation at ground level due to aerosol provide negative effects on temperature difference. The difference in temperature should reach zero when $\Delta B=0$ in conditions with zero AOT.

For Moscow and Lindenberg we obtained a pronounced statistically significant dependence which provides similar aerosol temperature effects. For Moscow, the effect is 0.8 ± 0.2 K per 100 W/m^2, which is in agreement with our previous estimates (Poliukhov et al. 2017). For Lindenberg the value is 1.0 ± 0.3 K per 100 W/m^2 with correlation coefficients r = 0.5,

0.6 respectively. The observed deviations may occur due to some slight variations in other parameters (water vapour, differences in profiles, etc.) in COSMO model runs.

Another testing was made using similar approach using comparisons with observations. In this case we should have much more deviations due to the influence of the uncertainty in actual atmospheric parameters which may differ from the simulated ones. We obtained the same tendency with the increase of positive temperature shift with positive bias in net radiation, which is mainly a function of aerosol loading. The gradients are similar to those obtained in the previous pure model experiment. These results confirm the pronounced temperature sensitivity to aerosol loading via its influence on net radiation at ground.

For estimating typical aerosol temperature effects for Moscow and Lindenberg, the changes in net radiation due to the changes in corresponding aerosol properties against aerosol–free conditions should be used. These temperature effects comprise about -0.2 K to -0.3 K for typical aerosol loads over these sites.

9.1.5   Temperature forecast sensitivity to aerosols

To estimate aerosol temperature effects we made simulation using COSMO for large domain (Europe – North Asia) with 13.3 km grid spacing for the central months of the seasons – January, April, July and October 2017. We performed simulations with Tanre climatology as a reference. Monthly averaged differences in T2m for July 2017 for simulations with Tegen and MACv2 aerosol climatologies as well as with CAMS reanalysis (see 7) are presented in Fig. 52.

T2m difference reaches 0.5 K (mostly on the regions with high probability of dust aerosol - North Africa, Meddle East, Central Asia) between simulations with old Tanre aerosol climatology and new one (MACv2) or CAMS. Significant positive T2m response up to 1 K appears in the North Africa and southern Europe in the case of MACv2 (Fig. 52b).

The assessment of temperature forecast considering MACv2 climatology and forecasted aerosol from CAMS compared to simulations with Tanre aerosol data was fulfilled using SYNOP and upper air sounding data. Simulation results with of MACv2 and CAMS show T2m RMSE decreases in southern Europe on 0.2-0.4 K (Fig. 53a,b). An effect of the new aerosol data implementation is neutral for the upper atmosphere.
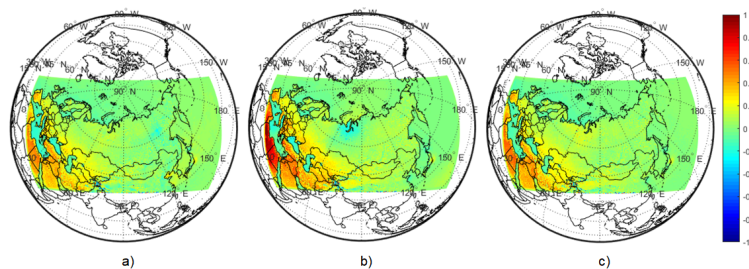

Figure 52: Monthly averaged differences in T2m for July 2017 for simulation with different aerosol setting compare to simulation with Tanre climatology: a) CAMS, b) MACv2, c) Tegen.
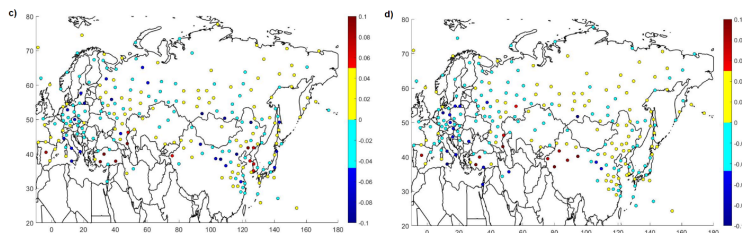
Figure 53: RMSE difference for T2m (a,b), T850 (c,d), T500 (e,f) forecasts between simulations with Tanre data and CAMS data (a,c,e) or MACv2 data (b,d,f).

9.2 Verifications in Cloudy skies conditions

9.2.1 Assessment of water vapour, liquid and ice water content in radiative scheme

To understand COSMO model behaviour in forecasting of the humidity characteristics we verified atmospheric water vapour content, cloud water and ice content, their vertical distribution and vertically integrated values using observations at Lindenberg observatory for the period March – October 2016. Appendix A contains the description of the experimental dataset.

All simulations were made with operational version of the model with 2.2 km grid spacing and 60 vertical levels for 550 x 600 km domain.

Results showed a correlation between errors in ice water content (QI) and water vapour content (QV) in the upper layers (6-12 km) (see Chubarova et al., 2018; Shatunova et al., 2019). An overestimation of QV values (see Fig. 2 in Chubarova et al., 2018) leads to overestimation of QI (Fig. 3 in Shatunova et al., 2019). In general, the model tends to overestimate total ice content. Model overestimate total water content (TQC) for rather small absolute values and underestimates TQC when its value is greater 0.1 kg/m^2.

9.2.2 Global radiation sensitivity to aerosol content

To investigate an impact of different aerosol setting on cloud optics and global radiation we made simulations with different set of concentration of cloud nuclei (CCN): fixed value characterized pure maritime, pollutant continental and intermediate clouds, and CCN calculated from Tegen aerosol climatology. Control runs were made with the default version of COSMO model without activation of the new COSMO radiation scheme (CLOUDRAD).

Simulations were performed with COSMO configuration with grid spacing 2.2 km for a domain covering Central Federal Region with Moscow located in the center of the domain for the warm period (April – October) of 2018. The data on global and direct radiation observed at the Meteorological observatory of Moscow State University were used to assess the quality of the obtained results.

Cloud optical thickness (OT) variation due to different CCN setting was investigated for the days with low cloud liquid water content. Cloud OT relative difference compare to control runs are presented in Fig. 54. Decreasing of cloud optical thickness within the lower 1.5

km layer of the atmosphere varies from 15% to 35 %. Smaller number concentration means larger water droplets and smaller OT (more transparent clouds).

The model setups tested (Figs 54, 55) were: the default radiation scheme (iradpar_cloud=1) as a control run, CCN calculated using SK2006 with Tegen aerosols as input (iradpar_cloud=4, cloud_num_type_rad = 2; itype_aerosol = 2), three setups with fixed number concentration at cloud base with exponential decay (iradpar_cloud=4, cloud_num_type_rad=1; itype_aerosol= 2, cloud_num_rad=100, 400, 1700) see Sec. 7 for details.

Comparison of global radiation simulated with default and CLOUDRAD schemes against observations is presented on Fig. 55. For the cases with optically thick clouds when the observed global radiation was less than 100 W/m^2 the errors of the predicted values do not exceed 50 W/m^2 and the old scheme showed here the best agreement. When observed global radiation is more than 250 W/m^2 which we can consider as optically thin cloud case, errors increase and difference between schemes become more evident. In overall, the results obtained with the new CLOUDRAD scheme have better agreement with observations (for details see Chubarova et al., 2018; Khlestova et al., 2019).
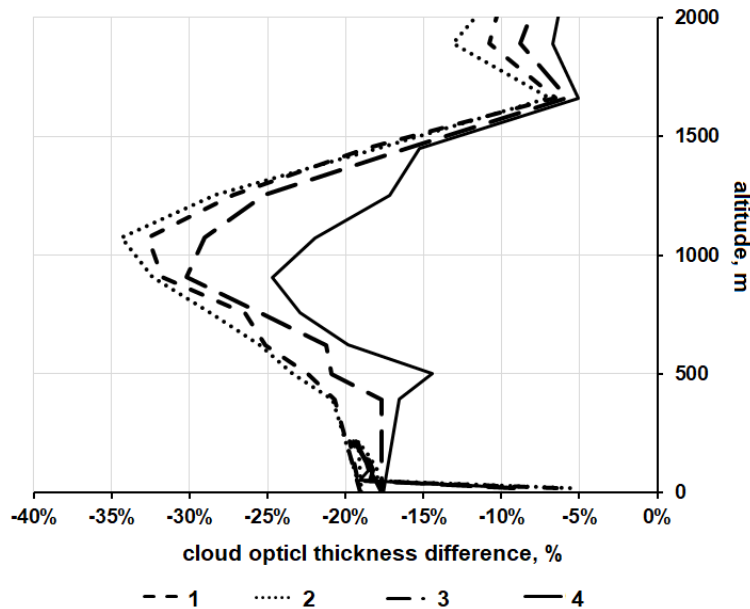
Figure 54: Cloud optical thickness relatively difference in dependence of CCN setting calculated with CLOUDRAD scheme compare to model version without CLOUDRAD. 1 – CCN from Tegen aerosol climatology, 2 – CCN = 100 cm^{-3}, 3 – CCN = 400 cm^{-3}, 4 – CCN = 1700 cm^{-3} see text for details of the setups.
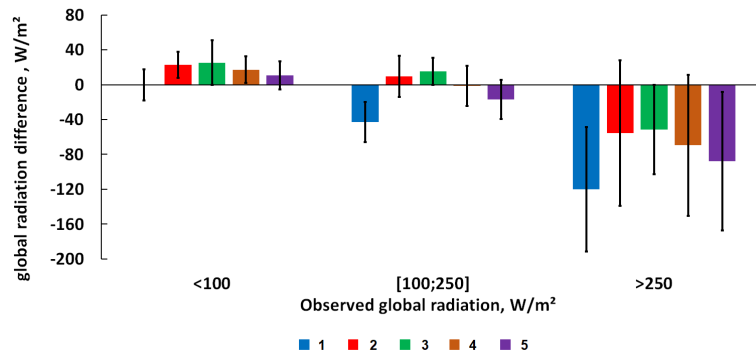
Figure 55: Verification of global radiation simulated with the old scheme (1) and the CLOUDRAD scheme with different aerosol setting (2 – CCN from Tegen aerosol climatology, 3 – CCN = 100 cm^{-3}, 4 – CCN = 400 cm^{-3}, 5 – CCN = 1700 cm^{-3}) against observations at Moscow State university observatory.

9.2.3 T2m forecast sensitivity

Taking into account the microphysical parameters of the cloud for evaluating its optical properties provide the increase in accuracy of both simulated global radiation, and air temperature forecast for the daytime. T2m forecast was verified against SYNOP observations (147 stations) for the period April-October 2018 for the Moscow region. Assessment shows that for the operational version (old scheme) RMSE equals 2.23 K and for the CLOUDRAD scheme RMSE is 2.04 K. The comparison of the scores for the two schemes is presented on Fig. 56. We should note that advantages of the old scheme within the first forecast hours is due to data assimilation system that was not applied for the simulations with CLOUDRAD.
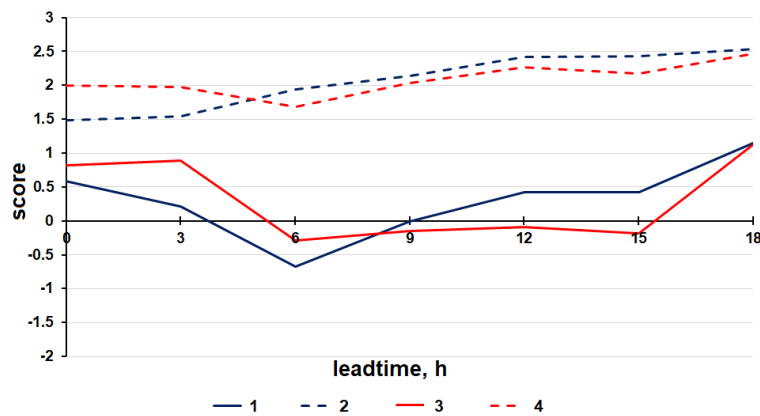
Figure 56: T2m forecast verification. Old scheme: 1 – Mean Error, 2 – RMSE; CLOUDRAD scheme: 3 –Mean Error, 4 – RMSE.

9.3 Conclusions

9.3.1 Clear sky case

MACv2 climatology provide better agreement with aerosol parameters for Moscow and Israel sites than Tegen climatology. The instant temperature sensitivity effects to aerosol loading is about 0.8-1.0 $\pm0.2°$C per 100 W/m^2 in net radiation at ground. The application of a new MACv2 aerosol climatology provides a significant positive temperature (T2m) response of up to 1 K over Northern Africa and southern Europe in case of MACv2 compared with the results with the Tanre climatology application. Simulated results with MACv2 and CAMS demonstrate the T2m RMSE decrease in southern Europe on 0.2-0.4 K.

9.3.2 Cloudy case

Verification of COSMO model against ground-based measurements was made using the standard and CLOUDRAD cloud-radiation schemes with 2.2 km grid and 60 vertical levels for 550 x 600 km domain with start time at 00 UTC. In days with low cloud liquid water content, with solar irradiance above 250 W/m^2 we obtained a pronounced decrease in cloud optical thickness of 15-35%, when a new CLOUDRAD scheme was used. This change provides the increase in global irradiance at ground, which, in turn, leads to a better agreement with the observed global irradiance. In situations with optically thick cloudiness (with solar irradiance less 100 W/m^2) there is no difference between the two schemes.

Temperature T2m forecast sensitivity using the new CLOUDRAD scheme has been verified against SYNOP observations over Moscow region. The results demonstrated better agreement with the new CLOUDRAD scheme with decrease in RMSE from 2.23 (for the standard scheme) to 2.04 (CLOUDRAD scheme).

10 Testing and tuning of the new cloud-radiation scheme

(P. Khain)

10.1 Overview

The new cloud-radiation-coupling scheme includes revised sub-grid scale clouds effect on radiation, detailed optical properties for liquid and frozen particles of different sizes, more accurate representation of aerosol effects on cloud microphysics, etc. From algorithmical point of view, the new scheme contains many cloud-radiation dependencies which contribution is described by about thirty parameters. Besides, different options are activated using ten logical switches. This makes the tuning of the scheme a difficult problem. The idealized COSMO framework was previously used to determine the parameters having particularly high influence on the radiative fluxes in the model (Khain et al., 2016). Here we utilize an "objective" parameters tuning (Voudouri et al., 2017; Khain et al., 2017) via comparison of real model forecasts against global radiation from CM-SAF satellite data (Müller et al., 2015). The experiments were performed for several month during 2016 over COSMO-DE domain. We present parameters values of four subversions of COSMO-cloudrad, which optimize the global radiation over Offenbach, Lindenberg and Munich regions.

10.2 Calibrated COSMO-CLOUDRAD versions

The main features of the four calibrated versions, and the list of tuned parameters for each version are summarized in table 101. The four versions are: "Basic" version – Tegen aerosol climatology is assumed as well as constant cloud droplets number concentration and effective radius; "CAMS" version – Similar to "Basic" but assuming interpolated in time and space CAMS aerosol background; "SK basic" version – Tegen aerosol climatology is assumed, Segal-Khain parametrization is used for estimation of droplets number concentration and effective radius; "SK-SAM" version – similar to "SK basic" version with the use of "adiabatic" parametrization for droplets microphysics in convective SGS clouds (see chapter 5).

Key switches	Tuned continuous parameters	Calibrated versions			
Parameter meaning	**Parameter**	**Basic version**	**CAMS version**	**SK basic version**	**SK-SAM version**
Tegen/CAMS CCN	itype_aerosol	2	4	2	2
Use Segal Khain parametrization for the droplets number concentration	icloud_num_type_rad	1	1	2	2
Use constant SGS droplets effective radius	luse_reff_ini_c_as_reffc_sgs	TRUE	TRUE	FALSE	FALSE
Use adiabatic profiles for droplets microphysics in convective SGS clouds	luse_qc_adiab_for_reffc_sgs	FALSE	FALSE	FALSE	TRUE
LWC reduction due to SGS variability	radqcfact [0.4 0.5 0.9]	X	X	X	X
IWC reduction due to SGS variability	radqifact [0.4 0.5 0.9]	X	X	X	X
SGS droplets effective radius	reff_ini_c [3 5 20]·10^{-6}	X	X		
SGS LWC scale factor	qvsatfact_sgscl_rad [0.005 0.01 0.02]	X	X	X	X
Droplets number concentration for radiation	cloud_num_rad [0.5 2 5]·10^{8}	X	X		
SGS droplets effective radius scale of adiabatic profile	reff_avg_fact [0.5 0.9 1]				X
SGS droplets concentration scale of adiabatic profile (clouds dilution)	qnc_avg_fact [0.1 0.38 1]				X

Figure 57: The main features of the four calibrated COSMO-cloudrad versions, and the list of tuned parameters for each version.

10.2 Global Radiation sensitivity

Before performing the calibration, we analyse the sensitivity of the global radiation to the change in the parameters (see Fig. 58). For every version and every parameter (X in Fig. 57) the averaged modelled (solid line) global radiation for 12Z is plotted against the parameter value (keeping other parameters in their default value) and is compared to the averaged observed value (dashed line).
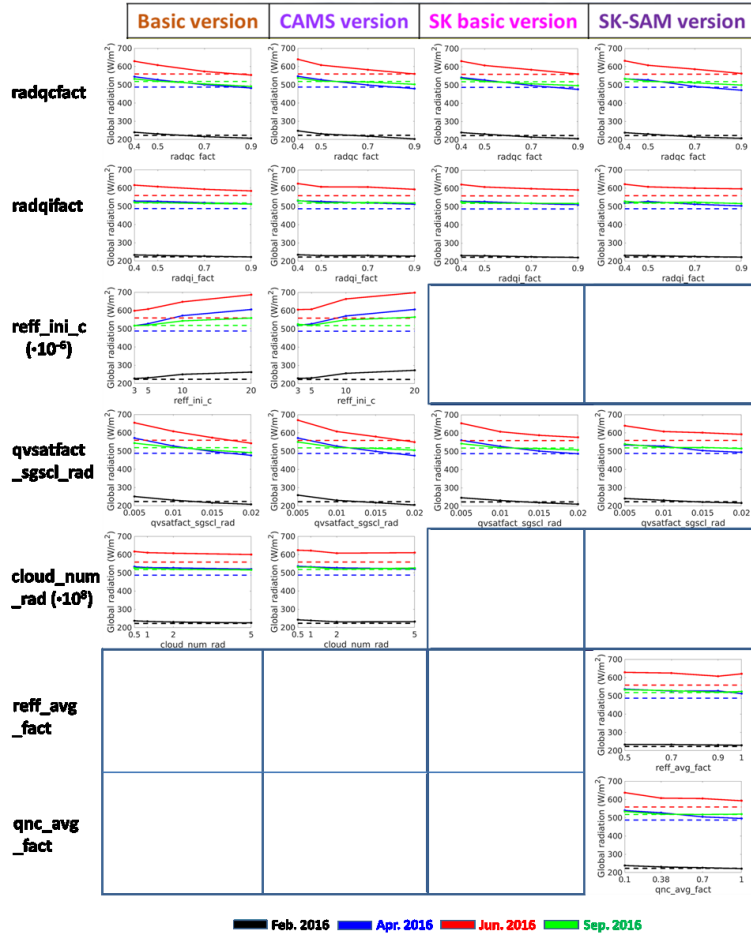
Figure 58: Sensitivity of the global radiation to the change in the parameters. For every version and every parameter (X in Fig. 57) the averaged modelled (solid line) global radiation (shortwave downward radiation on surface) for 12Z is plotted against the parameter value (keeping the other parameters default) and is compared to the averaged observed value (dashed line). February, April, June and September 2016 are denoted by black, blue, red and green lines, respectively.

Intermediate insights from Fig. 58:

1. Increase in radqcfact strongly reduces the global radiation due to increase grid scale and sub-grid scale clouds LWC.

2. radqifact, related to cloud ice water content, has weaker effect.

3. Increase in reff_ini_c, meaning higher SGS effective radius i.e. larger droplets, strongly increases the global radiation.

4. Larger qvsatfact_sgscl_rad, or larger SGS LWC, strongly reduces the global radiation.

5. Increasing cloud_num_rad (higher water droplets number concentration) slightly reduces the global radiation.

6. reff_avg_fact has two contradicting effects. A larger value increases the size of droplets in SGS cumulus making them more transparent. On the other hand, it increases clouds LWC which enlarge their optical depth.

87

7. Larger qnc_avg_fact slightly reduces the global radiation (because lower dilution leads to larger SGS LWC in cumulus. This parameter is more significant in convective seasons (i.e. April and June).

10.3   Calibration method

We have calibrated four COSMO-DE 2.8km 5.1 CLOUDRAD versions (Fig. 57) driven by ICON-EU analyses. For each version several continuous parameters are tuned (cyan in Fig. 57). The simulation and calibration domains are presented in Fig. 59.
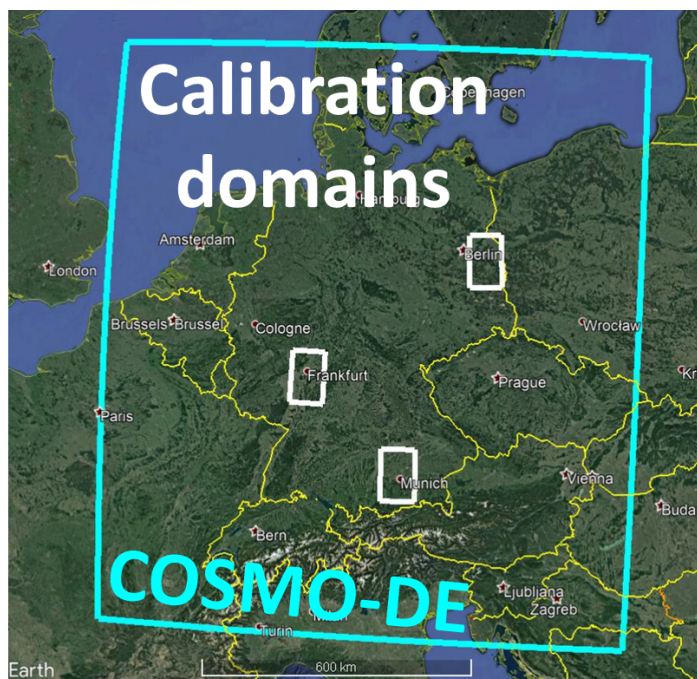
Figure 59: Simulation domain of COSMO-DE (cyan) and calibration domains (three white areas).

The calibration method is the following. First, several parameters combinations are chosen according to specific design (Voudouri et al. 2017). For each combination, COSMO runs are performed for February, April, June and September 2016. For every hour at every grid point, the forecast of global radiation is then interpolated in parameters space using 2nd order polynomial with interaction terms. These interpolations yield a guess for the global radiation for any chosen parameters combination (Meta-Model). For optimization, the parameters space is then sampled by large number of parameter combinations. For each combination the Meta-Model is verified against CM-SAF hourly global radiation at 5km resolution. We look for the optimal parameters combination using a convergence algorithm (Khain et al. 2017). Finally the parameters combination which yields the optimal Meta-Model guess is defined.

10.4 Calibration results

	Basic version	CAMS version	SK basic version	SK-SAM version
radqcfact	0.547 (34.5%) 0.55 (17%) 0.503 (4.1%) 0.571 (19.6%)	0.507 (13.3%) 0.555 (13%) 0.492 (1.8%) 0.532 (22.8%)	0.496 (5.4%) 0.573 (24.2%) 0.468 (9.4%) 0.495 (5.9%)	0.483 (8.4%) 0.613 (42.7%) 0.496 (3.2%) 0.495 (7.3%)
radqifact	0.509 (14%) 0.493 (6.2%) 0.491 (1.1%) 0.486 (8.2%)	0.476 (8.6%) 0.485 (4.9%) 0.508 (6.5%) 0.487 (1.4%)	0.711 (89.4%) 0.581 (77.3%) 0.497 (8%) 0.487 (5.6%)	0.481 (10.5%) 0.48 (6%) 0.503 (2.9%) 0.493 (9.5%)
reff_ini_c $(\cdot 10^{-6})$	5.85 (7%) 5.785 (1.2%) 5.87 (1.2%) 5.838 (8%)	5.965 (7.8%) 5.67 (3.3%) 5.461 (3.3%) 5.672 (4.9%)		
qvsatfact_sgscl_rad	0.012 (72.2%) 0.01 (50.7%) 0.014 (44.1%) 0.009 (26.2%)	0.014 (47.1%) 0.01 (25.1%) 0.012 (30%) 0.01 (36.4%)	0.011 (71.2%) 0.008 (22.5%) 0.017 (15.1%) 0.011 (76.6%)	0.012 (62.5%) 0.008 (16.2%) 0.01 (3.6%) 0.009 (26.3%)
cloud_num_rad $(\cdot 10^{8})$	1.216 (11.2%) 1.281 (1.3%) 1.331 (15%) 1.3 (6.7%)	1.673 (11.2%) 1.274 (2.5%) 1.288 (5.6%) 1.536 (12.8%)		
reff_avg_fact				0.933 (2.9%) 0.923 (1.2%) 0.94 (1%) 0.933 (3.4%)
qnc_avg_fact				0.513 (70.8%) 0.32 (4.9%) 0.898 (2.4%) 0.685 (52.4%)

Figure 60: Optimal parameters values for February, April, June and September 2016 (black, blue, red and green, respectively) averaged over the 3 regions. In parenthesis – uncertainty with respect to parameter range.

Fig. 60 presents the optimal parameters values for the four calibrated COSMO-cloudrad versions for each of the four selected month.
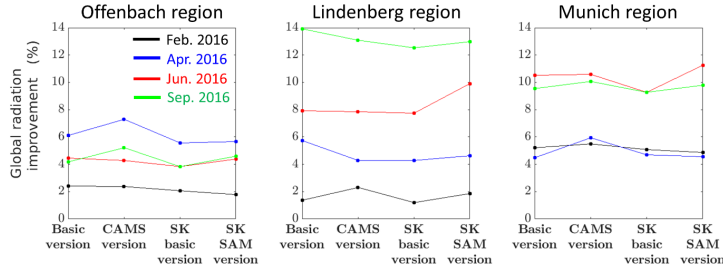
Figure 61: Global radiation estimated improvement (%) when using the optimal parameter combinations.

One can see that the global radiation forecast improvement by various COSMO-CLOUDRAD versions is similar. In summertime it reaches ∼10%. CAMS version has little effect with respect to the "Basic" because in that version the prognostic CCN plays role in the clear sky conditions only. The "SK-SAM" version improves the "SK basic" in summertime due to larger role of SGS cumulus clouds over Germany. Larger improvement from SK parametrization is expected when prognostic CCN is used for droplets activation but this experiment was not performed in this study.

11 Acknowledgements

nucleation processes, Alessio Bozzo for numerous discussions and for providing the aerosols optical properties data set used in ECMWF, Alexander Khain for fruitful discussions on cloud formation and aerosols and Theodore Andreadis for creating the COSMO cloud optics web-app.

12 References

Abakumova G., Gorbarenko, E., 2008. Transparency of the atmosphere in Moscow over the last 50 years and its changes in Russia. *LKI Publishing House (in Russian)*, p. 192

Alpert P., Neeman B.U., Shay-El Y., 1990. Climatological analysis of Mediterranean cyclones using ECMWF data. *Tellus*, **42A**, 65-77

Baldauf M., Seifert A., Förstner J., Majewski D., Raschendorfer M., Reinhardt T., 2011. Operational convective-scale numerical weather prediction with the COSMO model: description and sensitivities. *Mon. Weather Rev.* **139**, 3887–3905, https://doi.org/10.1175/MWR?D?10?05013.1

Baum, B.A., A.J. Heymsfield, P. Yang, and S.T. Bedka, 2005. Bulk Scattering Properties for the Remote Sensing of Ice Clouds. Part I: Microphysical Data and Models. *J. Appl. Meteor.*, **44**, 1885–1895

Baum, B.A., P. Yang, A.J. Heymsfield, C.G. Schmitt, Y. Xie, A. Bansemer, Y. Hu, and Z. Zhang, 2011. Improvements in Shortwave Bulk Scattering and Absorption Models for the Remote Sensing of Ice Clouds. *J. Appl. Meteor. Climatol.*, **50**, 1037–1056

Beard, K.V., 1976. Terminal velocity and shape of cloud and precipitation drops aloft. *J. Atmos. Sci.*, **33**, 852–864

Ben Bouallègue Z, Theis SE. 2014. Spatial techniques applied to precipitation ensemble forecasts: from verification results to probabilistic products. *Met. Apps*, **21**, 922–929. doi:10.1002/met.1435

Blahak, U., 2015. Simulating idealized cases with the cosmo-model. http://www.cosmo-model.org/content/model/documentation/core/artif_docu.pdf

Blahak, U. and Ritter, B., 2013. Towards revised cloud radiation coupling for the COSMO Model, COSMO/CLM User Seminar, 5-8 March, Offenbach, Germany

Bott, A., 1998. A flux method for the numerical solution of the stochastic collection equation. *J. Atmos. Sci.*, **55**, 2284–2293, doi:10.1175/1520-0469(1998)055<2284:AFMFTN>2.0.CO;2

Chubarova N. Y., Poliukhov A. A., and Gorlova I. D., 2016. Long-term variability of aerosol optical thickness in Eastern Europe over 2001–2014 according to the measurements at the Moscow MSU MO AERONET site with additional cloud and NO 2 correction. *Atmospheric Measurement Techniques*, **9**(2), pp. 313–334

Chubarova N. , J. Khlestova, M. Shatunova, V. Platonov, G. Rivin, U. Görsdorf, and R. Becker, 2018. Cloud characteristics and cloud radiative effects according to cosmo mesoscale model and measurements. Proc. SPIE 10833, 24th International Symposium on Atmospheric and Ocean Optics: Atmospheric Physics, 10833:108331N–1–108331N–8

Chubarova Natalia, Poliukhov Aleksei, Shatunova Marina, Rivin Gdaliy, Becker Ralf, and Kinne Stefan, 2018. Clear-sky radiative and temperature effects of different aerosol climatologies in the cosmo model. *Geography, Environment, Sustainability*, **11**(1), 74–84

Chubarova, N., Khlestova, J., Shatunova, M., Platonov, V., Rivin, G., Görsdorf, U., &

Becker, R., 2018a. Cloud characteristics and cloud radiative effects according to COSMO mesoscale model and measurements. Proc. SPIE 10833, 24th International Symposium on Atmospheric and Ocean Optics: Atmospheric Physics, 108331N (13 December 2018); https://doi.org/10.1117/12.2504340

Chubarova, N., Poliukhov, A., Shatunova, M., Rivin, G., Becker, R., & Kinne, S., 2018b. Clear-Sky Radiative And Temperature Effects Of Different Aerosol Climatologies In The Cosmo Model. *Geography, Environment, Sustainability*, **11**(1), 74–84. DOI: 10.24057/2071-9388-2018-11-1-74-84

Cooper, W. A., 1986. Ice initiation in natural clouds. Precipitation Enhancement: A Scientific Challenge. *Meteor. Monogr. Amer. Meteor. Soc.*, **43**, 29–32

Dagan G., I. Koren, O. Altaratz, and RH. Heiblum, 2016. Aerosol effect on the evolution of the thermodynamic properties of warm convective cloud fields. *Sci. Rep.*, **6**, 38769, doi:10.1038/srep38769

Davis C. A., Brown B. G., and Bullock R. G., 2006a. Object-based verification of precipitation forecasts. Part I: Methodology and application to mesoscale rain areas. *Mon. Wea. Rev.*, **134**, 1785–1795

Davis C. A., Brown B. G., and Bullock R. G. 2006b. Object-based verification of precipitation forecasts. Part II: Application to convective rain systems. *Mon. Wea. Rev.*, **134**, 1785–1795

Davis C. A., Brown B. G., Bullock R. G. and Halley-Gotway J., 2009. The method for object-based diagnostic evaluation (MODE) applied to numerical forecasts from the 2005 NSSL/SPC Spring Program. *Wea. Forecasting*, **24**, 1252–1267

Deardorff, W. J., 1970. Preliminary results from numerical integrations of the unstable boundary layer. *J. Atmos. Sci.*, **27**, 1209–1231

DeMott, P.J., Prenni, A.J., McMeeking, G.R., Sullivan, R.C., Petters, M.D., Tobo, Y., Niemand, M., Möhler, O., Snider, J.R., Wang, Z., Kreidenweis, S.M., 2015. Integrating laboratory and field data to quantify the immersion freezing ice nucleation activity of mineral dust particles. *Atmos. Chem. Phys.*, **15**, 393–409

Doms G, Foerstner J, Heise E, Herzog HJ, Mironov D, Raschendorfer M, Reinhardt T, Ritter B, Schrodin R, Schulz JP, Vogel G. 2011. A Description of the Nonhydrostatic Regional COSMO Model, part 2: Physical Parameterization. (Available at: http://www.cosmo-model.org)

Duc L, Saito K, H. Seko H. 2013. Spatial-temporal fractions verification for high-resolution ensemble forecasts, *Tellus A: Dynamic Meteorology and Oceanography*, **65**(1), DOI: 10.3402/tellusa.v65i0.18171

Ebert E., 2009. Neighbourhood Verification: A Strategy for Rewarding Close Forecasts. *Wea. Forecasting*, *24*, 1498–1510, https://doi.org/10.1175/2009WAF2222251.1

Field, P.R., Hogan, R.J., Brown, P.R.A., Illingworth, A.J., Choularton, T.W. and Cotton, R.J., 2005. Parametrization of ice-particle size distributions for mid-latitude stratiform cloud. *Q.J.R. Meteorol. Soc.*, **131**, 1997–2017, doi:10.1256/qj.04.134

Fu, Q. and K.N. Liou, 1993. Parameterization of the Radiative Properties of Cirrus Clouds. *J. Atmos. Sci.*, **50**, 2008–2025

Fu, Q., 1996. An Accurate Parameterization of the Solar Radiative Properties of Cirrus Clouds for Climate Models. *J. Climate*, **9**, 2058–2082

Fu, Q., 2007. A New Parameterization of an Asymmetry Factor of Cirrus Clouds for Climate Models. *J. Atmos. Sci.*, **64**, 4140–4150

Fu, Q., Yang, P., & Sun, W., 1998. An Accurate Parameterization of the Infrared Radiative Properties of Cirrus Clouds for Climate Models. *Journal of Climate*, **11**(9), 2223–2237

Gasch, P., Rieger, D., Walter, C., Khain, P., Levi, Y., Knippertz, P., and Vogel, B., 2017. Revealing the meteorological drivers of the September 2015 severe dust event in the Eastern Mediterranean. *Atmos. Chem. Phys.*, **17**, 13573–13604, https://doi.org/10.5194/acp-17-13573-2017

Gasparini, B., and Lohmann, U., 2016. Why cirrus cloud seeding cannot substantially cool the planet. *J. Geophys. Res. Atmos.*, **121**, 4877– 4893

Ghan, S. J., Hayder Abdul-Razzak, A. Nenes, Yi Ming, Xiaohong Liu, M. Ovchinnikov, Ben Shipway, N. Meskhidze, Jun Xu, and X. Shi, 2011. Droplet nucleation: Physically-based parameterizations and comparative evaluation. *J. Adv. Model. Earth Syst.*, **3**, M10001, 33 pp. DOI:10.1029/2011MS000074

Gilleland, E., D. Ahijevych, B.G. Brown, B. Casati, and E.E. Ebert, 2009. Intercomparison of Spatial Forecast Verification Methods. *Wea. Forecasting*, **24**, 1416–1430

Gilleland, E., D.A. Ahijevych, B.G. Brown, and E.E. Ebert, 2010. Verifying Forecasts Spatially. *Bull. Amer. Meteor. Soc.*, **91**, 1365–1376, https://doi.org/10.1175/2010BAMS2819.1

Giorgetta, M. A., Brokopf, R., Crueger, T., Esch, M., Fiedler, S., Helmert, J., 2018. ICON-A, the atmosphere component of the ICON Earth system model: I. Model description. *Journal of Advances in Modeling Earth Systems*, **10**, 1613–1637, https://doi.org/10.1029/2017MS001242

Gruber, S., Blahak, U., Haenel, F., Kottmeier, C., Leisner, T., Muskatel, H., et al., 2019. A process study on thinning of Arctic winter cirrus clouds with high-resolution ICON-ART simulations. *Journal of Geophysical Research: Atmospheres*, **124**

Hess M., Koepke P. and Schult I., 1998. Optical Properties of Aerosols and Clouds: The Sofware Package OPAC, *Bulletin of the American Meteorological Society*, p. 831

Hogan R., Mittermaier M., Illingworth A., 2006. The retrieval of Ice Water Content from Radar Reflectivity Factor and Temperature and Its Use in Evaluating A Mesoscale Model, *American Meteorological Society*

Hogan R.J., Illingworth A.J., 2003. Parameterizing ice cloud inhomogeneity and the overlap of inhomogeneities using cloud radar data, *J. Atmos. Sci.*, **60**, 756–767

Hu, Y.X. and K. Stamnes, 1993. An Accurate Parameterization of the Radiative Properties of Water Clouds Suitable for Use in Climate Models. *J. Climate*, **6**, 728–742

Illingworth A.J. et.al., 2007. Cloudnet – Evaluation of Cloud Profiles in Seven Operational Models Using Ground-Based Observations, *Bull. Amer. Met. Soc.*, **88**, 883–898

Jiang, H., G. Feingold, H. H. Jonsson, M.-L. Lu, P. Y. Chuang, R. C. Flagan, and J. H. Seinfeld, 2008. Statistical comparison of properties of simulated and observed cumulus clouds in the vicinity of Houston during the Gulf of Mexico Atmospheric Composition and Climate Study (GoMACCS), *J. Geophys. Res.*, **113**, D13205, doi:10.1029/2007JD009304

Joseph, J.H., W.J. Wiscombe, and J.A. Weinman, 1976. The Delta-Eddington Approximation for Radiative Flux Transfer. *J. Atmos. Sci.*, **33**, 2452–2459, https://doi.org/10.1175/1520-0469(1976)033<2452:TDEAFR>2.0.CO;2

Key, J. R., Yang, P., Baum, B. A., and Nasiri, S. L., 2002. Parameterization of short-

wave ice cloud optical properties for various particle habits, *J. Geophys. Res.*, **107**(D13), doi:10.1029/2001JD000742

Khain P., H. Muskatel and U. Blahak, 2016. Priority Project T2RC2: Determination of governing parameters in the new radiation scheme. COSMO User Seminar 2016

Khain P., I. Carmona, A. Voudouri, E. Avgoustoglou, J-M. Bettems, F. Grazzini, P. Kaufmann, 2017. CALMO - Progress Report. COSMO technical report 31, available at www.cosmo-model.org, DOI: 10.5676/DWDpub/nwv/cosmo-tr31

Khain, A. P., A. Pokrovsky, M. Pinsky, A. Seifert, and V. Philips, 2004. Simulation of effects of atmospheric aerosols on deep turbulent convective clouds by using a spectral microphysics mixed-phase cumulus cloud model. Part I: Model description and possible applications. *J. Atmos. Sci*, **61**, 2963–2982

Khain, A. P., and M. Pinsky, 2018. Physical Processes in Clouds and Cloud Modeling. *Cambridge University Press*, 642 pp.

Khain, A. P., M. Ovchinnikov, M. Pinsky, A. Pokrovsky, and H. Krugliak, 2000. Notes on the state-of-the-art numerical modeling of cloud microphysics, *Atmos. Res.*, **55**, 159–224

Khain, A., T. V. Prabha, N. Benmoshe, G. Pandithurai, and M. Ovchinnikov, 2013. The mechanism of first raindrops formation in deep convective clouds, *J. Geophys. Res. Atmos.*, **118**, 9123–9140, doi:10.1002/jgrd.50641

Khain, P., R. Heiblum, U. Blahak, Y. Levi, H. Muskatel, E. Vadislavsky, O. Altaratz, I. Koren, G. Dagan, J. Shpund, and A. Khain, 2019. Parameterization of Vertical Profiles of Governing Microphysical Parameters of Shallow Cumulus Cloud Ensembles Using LES with Bin Microphysics. *J. Atmos. Sci.*, **76**, 533–560, https://doi.org/10.1175/JAS-D-18-0046.1

Khairoutdinov, M. F., and D. A. Randall, 2003. Cloud resolving modeling of the ARM summer 1997 IOP: Model formulation, results, uncertainties, and sensitivities, *J. Atmos. Sci.*, **60**(4), 607–625, doi:10.1175/1520-0469

Khlestova J., Chubarova N., Shatunova M., 2019. Radiative and temperature effects of clouds based on the results of numerical experiments of the COSMO mesoscale model and measurement data. Proceedings of SPIE (The International Society for Optical Engineering), *25th International Symposium on Atmospheric and Ocean Optics: Atmospheric Physics*, **11208**

Khvorostyanov, V.I. and J.A. Curry, 1999. Toward the Theory of Stochastic Condensation in Clouds. Part I: A General Kinetic Equation. *J. Atmos. Sci.*, **56**, 3985–3996, https://doi.org/10.1175/1520-0469

Kinne S., 2019. The Macv2 aerosol climatology. *Tellus B Chem. Phys. Meteorol.*, **71**, 1–21

Kunz M., Blahak U., Handwerker J., Schmidberger M., Punge H.J., Mohr S., Fluck E., Bedka K.M., 2018. The severe hailstorm in southwest Germany on 28 July 2013: characteristics, impacts and meteorological conditions. *Q.J.R. Meteorol. Soc.*, **144**, 231-250, doi:10.1002/qj.3197

Lindner, T.H. and J. Li, 2000. Parameterization of the Optical Properties for Water Clouds in the Infrared. *J. Climate*, **13**, 1797–1805

Lohnert U., Meijgaard E., Baltinck H., Grob S., Boers R., 2007. Accuracy assessment of an integrated profiling technique for operationally deriving profiles of temperature, humidity and cloud liquid water. *Jour. Of Geoph. Res.*, **112**, D04205, doi:10.1029/2006JD007379

Lu, M. and J.H. Seinfeld, 2005. Study of the Aerosol Indirect Effect by Large-Eddy Simulation of Marine Stratocumulus. *J. Atmos. Sci.*, **62**, 3909–3932, https://doi.org/10.1175/JAS3584.1

Müller R., Pfeifroth U., Träger-Chatterjee C., Cremer R., Trentmann, J., Hollmann R., 2015. Surface Solar Radiation Data Set - Heliosat (SARAH) - Edition 1, *Satellite Application Facility on Climate Monitoring*, DOI:10.5676/EUM_SAF_CM/SARAH/V001

Macke, A., J. Mueller, and E. Raschke, 1996. Single Scattering Properties of Atmospheric Ice Crystals. *J. Atmos. Sci.*, **53**, 2813–2825

Magaritz-Ronen, L., A. Khain, and M. Pinsky, 2016b. About the horizontal variability of effective radius in stratocumulus clouds, *J. Geophys. Res. Atmos.*, **121**, 9640–9660, doi:10.1002/2016JD024977

Mittermaier M., Roberts N. 2010. Intercomparison of Spatial Forecast Verification Methods: Identifying Skillful Spatial Scales Using the Fractions Skill Score. *Wea. Forecasting*, **25**, 343–354, https://doi.org/10.1175/2009WAF2222260.1

Morcrette, J., et al., 2009. Aerosol analysis and forecast in the European Centre for Medium-Range Weather Forecasts Integrated Forecast System: Forward modeling. *J. Geophys. Res.*, **114**, D06206, doi:10.1029/2008JD011235

Muskatel, H.B., Blahak, U., Khain, P., Levi, Y., Fu, Q., 2021. Parametrizations of Liquid and Ice Clouds Optical Properties in Operational Numerical Weather Prediction Models. *Atmosphere*, **12**, 89, https://doi.org/10.3390/atmos12010089

Nickovic, S., Cvetkovic, B., Madonna, F., Rosoldi, M., Pejanovic,G., Petkovic, S., and Nikolic, J., 2016. Cloud ice caused by atmospheric mineral dust – Part 1: Parameterization of ice nuclei concentration in the NMME-DREAM model. *Atmos. Chem. Phys.*, **16**, 11367–11378, doi:10.5194/acp-16-11367-2016

Petty, G. W. and Huang W., 2011. The Modified Gamma Size Distribution Applied to Inhomogeneous and Non-spherical Particles: Key Relationships and Conversions. *Journal of the Atmospheric Sciences*, **68**(7), 1460–1473

Phillips, V. T. J., P. J. DeMott, and C. Andronache, 2008. An Empirical Parameterization of Heterogeneous Ice Nucleation for Multiple Chemical Species of Aerosol. *J. Atmos. Sci.*, **65**, 2757–2783, https://doi.org/10.1175/2007JAS2546.1

Pinsky, M. and A. Khain, 2018a. Theoretical Analysis of the Entrainment-Mixing Process at Cloud Boundaries. Part I: Droplet Size Distributions and Humidity within the Interface Zone. *J. Atmos. Sci.*, **75**, 2049–2064

Pinsky, M. and A. P. Khain, 2002. Effects of in-cloud nucleation and turbulence on droplet spectrum formation in cumulus clouds. *Quart. J. Roy. Meteorol. Soc.*, **128**, 1–33

Pinsky, M., A. Khain, I. Mazin, and A. Korolev, 2012. Analytical estimation of droplet concentration at cloud base. *J. Geophy. Res.*, **117**, D18211, doi:10.1029/2012JD017753

Pinsky, M., I. Mazin, A. Korolev and A. Khain, 2014. Supersaturation and diffusional droplet growth in liquid clouds: Polydisperse spectra. *J. Geophys Res.*, **119**, 12872–12887

Pinsky, M., Khain, A. P., and M. Shapiro, 2001. Collision efficiency of drops in a wide range of Reynolds numbers: Effects of pressure on spectrum evolution. *J. Atmos. Sci.*, **58**, 742–764

Pinsky, M., Khain, A., and Korolev, A. 2016b. Theoretical analysis of mixing in liquid clouds – Part 3: Inhomogeneous mixing. *Atmos. Chem. Phys.*, **16**, 9273-9297. www.atmos-chem-

phys.net/16/9273/2016/doi:10.5194/acp-16-9273-2016

Poliukhov A. A., N. E. Chubarova, D. V. Blinov, T. A. Tarasova, A. P. Makshtas, and H. Muskatel, 2019. Radiation effects of different types of aerosol in Eurasia according to observations and model calculations. *Russian Meteorology and Hydrology*, **44**(9), 579–587

Poliukhov, A. A., Chubarova, H. E., Shatunova, M. V., Rivin, G. S., Tarasova, T. A., Makshtas, A. P., Muskatel, H., 2018. Radiative effect of different aerosol types in clear sky conditions according to COSMO-Ru model. In 24th International Symposium on Atmospheric and Ocean Optics: Atmospheric Physics (**10833**, p. 1083308). International Society for Optics and Photonics. DOI: 10.1117/12.2504299

Poliukhov, A., Chubarova, N., Kinne, S., Rivin, G., Shatunova, M., & Tarasova, T., 2017. Comparison between calculations of shortwave radiation with different aerosol datasets and measured data at the MSU MO (Russia). In AIP Conference Proceedings (**1810**, 1, p. 100006). AIP Publishing. DOI: 10.1063/1.4975561

Pontikis, C. A., 1996. Parameterization of the droplet effective radius of warm layer clouds. *Geophys. Res. Lett.*, **23**(19), 2629–2632

Reid, J. S., Hobbs, P. V., Rangno, A. L., and Hegg, D. A., 1999. Relationships between cloud droplet effective radius, liquid water content, and droplet concentration for warm clouds in Brazil embedded in biomass smoke. *J. Geophys. Res.*, **104**(D6), 6145–6153, doi:10.1029/1998JD200119

Ritter, B. and J. Geleyn, 1992. A Comprehensive Radiation Scheme for Numerical Weather Prediction Models with Potential Applications in Climate Simulations. *Mon. Wea. Rev.*, **120**, 303–325

Roberts N.M., Lean H.W. 2008. Scale-Selective Verification of Rainfall Accumulations from High-Resolution Forecasts of Convective Events. *Mon. Wea. Rev.*, **136**, 78–97, https://doi.org/10.1175/2007MWR2123.1

Rosenfeld D., 2006. Aerosol-Cloud Interactions Control of Earth Radiation and Latent Heat Release Budgets. *Space Sci. Rev.*, **125**, 149–157, doi:10.1007/s11214-006-9053-6

Rosenfeld, D., I. M. Lensky, 1998. Satellite-Based Insights into Precipitation Formation Processes in Continental and Maritime Convective Clouds, *Bull. Am. Meteorol. Soc.*, **79**, 2457–2476, doi:10.1175/1520-0477

Rosenfeld, D., Lohmann, U., Raga, G. B., O'Dowd, C. D., Markku, M., Fuzzi, S., Reissell, A. and Andreae, M. O., 2008. Flood or Drought: How Do Aerosols Affect Precipitation? *Science*, 1309–1313

Rossow, W.B., and R.A. Schiffer, 1999. Advances in understanding clouds from ISCCP. *Bull. Amer. Meteorol. Soc.*, **80**, 2261–2288

Sassen, K., Wang, Z., and Liu, D., 2008. Global distribution of cirrus clouds from CloudSat/Cloud-Aerosol Lidar and Infrared Pathfinder Satellite Observations (CALIPSO) measurements. *J. Geophys. Res.*, **113**

Schröter, J., Rieger, D., Stassen, C., Vogel, H., Weimer, M., Werchner, S., Förstner, J., Prill, F., Reinert, D., Zängl, G., Giorgetta, M., Ruhnke, R., Vogel, B., and Braesicke, P., 2018. ICON-ART 2.1: a flexible tracer framework and its application for composition studies in numerical weather forecasting and climate simulations, *Geosci. Model Dev.*, **11**, 4043–4068, https://doi.org/10.5194/gmd-11-4043-2018

Schwartz, C.S., R.A. Sobash, 2017. Generating Probabilistic Forecasts from Convection-

Allowing Ensembles Using Neighborhood Approaches: A Review and Recommendations. *Mon. Wea. Rev.*, **145**, 3397–3418, https://doi.org/10.1175/MWR-D-16-0400.1

Segal Y., A. P. Khain, 2006. Dependence of droplet concentration on aerosol conditions in different cloud types: application to droplet concentration parameterization of aerosol conditions, *J. Geophys. Res.*, **111**, D15204, doi:10.1029/2005JD006561

Sharon D, Kutiel H. 1986. The distribution of rainfall intensity in Israel, its regional and seasonal variations and its climatological evaluation. *International Journal of Climatology*. **6**, 277–291

Shatunova, M.V., Khlestova, Y.O., Chubarova, N.E., 2020. Forecast of Microphysical and Optical Characteristics of Large-Scale Cloud Cover and Its Radiative Effect Using the COSMO Mesoscale Weather Prediction Model. *Atmos. Ocean Opt.*, **33**, 154–160, https://doi.org/10.1134/S1024856020020098

Shay-El Y, Alpert P. 1991. A diagnostic study of winter diabetic heating in the Mediterranean in relation to cyclones. *Quarterly Journal of the Royal Meteorological Society*, **117**, 715–747

Siebesma, A.P., Bretherton, C.S., Brown, A., Chlond, A., Cuxart, J., Duynkerke, P.G., Jiang, H., Khairoutdinov, M., Lewellen, D., Moeng, C.H. and Sanchez, E., 2003. A large eddy simulation intercomparison study of shallow cumulus convection. *Journal of the Atmospheric Sciences*, **60**(10), 1201–1219

Slingo, A., Schrecker, H. M., 1982. On the shortwave radiative properties of stratiform water clouds. *Q.J.R. Meteorol. Soc.*, **108**, 407–426

Slingo, A., 1989. A GCM Parameterization for the Shortwave Radiative Properties of Water Clouds. *J. Atmos. Sci.*, **46**, 1419–1427

Steinke, I., Hoose, C., Möhler, O., Connolly, P., and Leisner, T., 2015. A new temperature- and humidity-dependent surface site density approach for deposition ice nucleation, *Atmos. Chem. Phys.*, **15**, 3703–3717, https://doi.org/10.5194/acp-15-3703-2015

Stephens, G. L., 1979. Optical properties of eight water cloud types. CSIRO: Division of Atmospheric Physics, Tech. report 36

Stephens, G.L., 1984. The Parameterization of Radiation for Numerical Weather Prediction and Climate Models. *Mon. Wea. Rev.*, **112**, 826–867

Steppeler J., Doms G., Schattler U., Bitzer H.W., Gassmann A., Damrath U., Gregoric G., 2003. Meso gamma scale forecasts by non-hydrostatic model LM. *Meteorological Atmospheric Physics*, **82**, 75–96

Takano, Y., K. Liou, 1989. Solar Radiative Transfer in Cirrus Clouds. Part I: Single-Scattering and Optical Properties of Hexagonal Ice Crystals. *J. Atmos. Sci.*, **46**, 3–19

Tanre D., Geleyn J. F., and Slingo J. M., 1984. First results of the introduction of an advanced aerosol-radiation interaction in the ECMWF low resolution global model. *Aerosols and their climatic effects*, 133–177

Tarasova, Yarkho, 1991. Determination of aerosol optical thickness according to ground-based measurements of integral solar irradiance. *Russian Meteorology and Hydrology*, Planeta Publishing House, **12**, 66–71

Tegen, I., Hollrig, P., Chin, M., Fung, I., Jacob, D., and Penner, J., 1997. Contribution of different aerosol species to the global aerosol extinction optical thickness: Estimates from

model results. *Journal of Geophysical Research: Atmospheres*, **102**(D20), 23895–23915

Vergara-Temprado J., Miltenberger A.K., Furtado K., Grosvenor D.P., Shipway B.J., Hill A.A., Wilkinson J.M., Field P.R., Murray B.J., Carslaw K.S., 2018. Strong control of Southern Ocean cloud reflectivity by ice-nucleating particles. *Proceedings of the National Academy of Sciences of the United States of America*, **115**, 2687–2692

Voudouri A., Khain P., Carmona I., Bellprat O., Grazzini F., Avgoustoglou E. , Bettems J-M. and Kaufmann P., 2017. Objective calibration of numerical weather prediction models. *Atm. Res.*, **190**, 128–140

Ware R., Carpenter R., Guldner J., Liljegren J., Nehrkorn T., Solheim F., Vandenberghe F., 2003. A multichannel radiometric profiler of temperature, humidity and cloud liquid, *RADIO SCIENCE*, **38**, 4, 8079, doi:10.1029/2002RS002856

Wiscombe, W. J., 1977. The Delta-Eddington Approximation for a Vertically Inhomogeneous Atmosphere. NCAR Technical Note NCAR/TN-121+STR

Yanai, M., Esbensen, S., and Chu, J.-H., 1973. Determination of bulk properties of tropical cloud clusters from large-scale heat and moisture budgets. *J. Atmos. Sci.*, **30**, 611–627

Yang, P. and K. N. Liou, 1995. Light scattering by hexagonal ice crystals: comparison of finite-difference time domain and geometric optics models. *J. Opt. Soc. Am. A*, **12**, 162–176

Yang, P. and K. N. Liou, 1996. Finite-difference time domain method for light scattering by small ice crystals in three-dimensional space. *J. Opt. Soc. Am. A*, **13**, 2072–2085

Yang, P., L. Bi, B.A. Baum, K. Liou, G.W. Kattawar, M.I. Mishchenko, and B. Cole, 2013. Spectrally Consistent Scattering, Absorption, and Polarization Properties of Atmospheric Ice Crystals at Wavelengths from 0.2 to 100 μm. *J. Atmos. Sci.*, **70**, 330–347

Yang, P., Liou, K. N., Wyser, K., and Mitchell, D., 2000. Parameterization of the scattering and absorption properties of individual ice crystals, *J. Geophys. Res.*, **105**(D4), 4699–4718

Zängl, G., D. Reinert, P. Ripodas, and M. Baldauf, 2015. The ICON (ICOsahedral Nonhydrostatic) modelling framework of DWD and MPI-M: Description of the non-hydrostatic dynamical core. *Q.J.R. Meteorol. Soc.*, **141**, 563–579

Ziv B, Dayan U, Kushnir Y, Roth C, Enzel Y. 2006. Regional and global atmospheric patterns governing rainfall in the southern Levant. *International Journal of Climatology*, **26**(1), 55–73

List of COSMO Newsletters and Technical Reports

(available for download from the COSMO Website: www.cosmo-model.org)

COSMO Newsletters

No. 1: February 2001.

No. 2: February 2002.

No. 3: February 2003.

No. 4: February 2004.

No. 5: April 2005.

No. 6: July 2006.

No. 7: April 2008; Proceedings from the 8th COSMO General Meeting in Bucharest, 2006.

No. 8: September 2008; Proceedings from the 9th COSMO General Meeting in Athens, 2007.

No. 9: December 2008.

No. 10: March 2010.

No. 11: April 2011.

No. 12: April 2012.

No. 13: April 2013.

No. 14: April 2014.

No. 15: July 2015.

No. 16: July 2016.

No. 17: July 2017.

No. 18: November 2018.

No. 19: October 2019.

No. 20: December 2020.

COSMO Technical Reports

No. 1: Dmitrii Mironov and Matthias Raschendorfer (2001):
*Evaluation of Empirical Parameters of the New LM Surface-Layer Parameterization
Scheme. Results from Numerical Experiments Including the Soil Moisture Analysis.*
DOI: 10.5676/DWD_pub/nwv/cosmo-tr_1

No. 2: Reinhold Schrodin and Erdmann Heise (2001):
The Multi-Layer Version of the DWD Soil Model TERRA_LM.
DOI: 10.5676/DWD_pub/nwv/cosmo-tr_2

No. 3: Günther Doms (2001):
A Scheme for Monotonic Numerical Diffusion in the LM.
DOI: 10.5676/DWD_pub/nwv/cosmo-tr_3

No. 4: Hans-Joachim Herzog, Ursula Schubert, Gerd Vogel, Adelheid Fiedler and Roswitha Kirchner (2002):
LLM ¯ the High-Resolving Nonhydrostatic Simulation Model in the DWD-Project LIT-FASS. Part I: Modelling Technique and Simulation Method.
DOI: 10.5676/DWD_pub/nwv/cosmo-tr_4

No. 5: Jean-Marie Bettems (2002):
EUCOS Impact Study Using the Limited-Area Non-Hydrostatic NWP Model in Operational Use at MeteoSwiss.
DOI: 10.5676/DWD_pub/nwv/cosmo-tr_5

No. 6: Heinz-Werner Bitzer and Jürgen Steppeler (2004):
Documentation of the Z-Coordinate Dynamical Core of LM.
DOI: 10.5676/DWD_pub/nwv/cosmo-tr_6

No. 7: Hans-Joachim Herzog, Almut Gassmann (2005):
Lorenz- and Charney-Phillips vertical grid experimentation using a compressible non-hydrostatic toy-model relevant to the fast-mode part of the 'Lokal-Modell'.
DOI: 10.5676/DWD_pub/nwv/cosmo-tr_7

No. 8: Chiara Marsigli, Andrea Montani, Tiziana Paccagnella, Davide Sacchetti, André Walser, Marco Arpagaus, Thomas Schumann (2005):
Evaluation of the Performance of the COSMO-LEPS System.
DOI: 10.5676/DWD_pub/nwv/cosmo-tr_8

No. 9: Erdmann Heise, Bodo Ritter, Reinhold Schrodin (2006):
Operational Implementation of the Multilayer Soil Model.
DOI: 10.5676/DWD_pub/nwv/cosmo-tr_9

No. 10: M.D. Tsyrulnikov (2007):
Is the particle filtering approach appropriate for meso-scale data assimilation ?
DOI: 10.5676/DWD_pub/nwv/cosmo-tr_10

No. 11: Dmitrii V. Mironov (2008):
Parameterization of Lakes in Numerical Weather Prediction. Description of a Lake Model.
DOI: 10.5676/DWD_pub/nwv/cosmo-tr_11

No. 12: Adriano Raspanti (2009):
COSMO Priority Project "VERification System Unified Survey" (VERSUS): Final Report.
DOI: 10.5676/DWD_pub/nwv/cosmo-tr_12

No. 13: Chiara Marsigli (2009):
COSMO Priority Project "Short Range Ensemble Prediction System" (SREPS): Final Report.
DOI: 10.5676/DWD_pub/nwv/cosmo-tr_13

No. 14: Michael Baldauf (2009):
COSMO Priority Project "Further Developments of the Runge-Kutta Time Integration Scheme" (RK): Final Report.
DOI: 10.5676/DWD_pub/nwv/cosmo-tr_14

No. 15: Silke Dierer (2009):
COSMO Priority Project "Tackle deficiencies in quantitative precipitation forecast"
(QPF): Final Report.
DOI: 10.5676/DWD_pub/nwv/cosmo-tr_15

No. 16: Pierre Eckert (2009):
COSMO Priority Project "INTERP": Final Report.
DOI: 10.5676/DWD_pub/nwv/cosmo-tr_16

No. 17: D. Leuenberger, M. Stoll and A. Roches (2010):
Description of some convective indices implemented in the COSMO model.
DOI: 10.5676/DWD_pub/nwv/cosmo-tr_17

No. 18: Daniel Leuenberger (2010):
Statistical analysis of high-resolution COSMO Ensemble forecasts in view of Data Assimilation.
DOI: 10.5676/DWD_pub/nwv/cosmo-tr_18

No. 19: A. Montani, D. Cesari, C. Marsigli, T. Paccagnella (2010):
Seven years of activity in the field of mesoscale ensemble forecasting by the COSMO–LEPS system: main achievements and open challenges.
DOI: 10.5676/DWD_pub/nwv/cosmo-tr_19

No. 20: A. Roches, O. Fuhrer (2012):
Tracer module in the COSMO model.
DOI: 10.5676/DWD_pub/nwv/cosmo-tr_20

No. 21: Michael Baldauf (2013):
A new fast-waves solver for the Runge-Kutta dynamical core.
DOI: 10.5676/DWD_pub/nwv/cosmo-tr_21

No. 22: C. Marsigli, T. Diomede, A. Montani, T. Paccagnella, P. Louka, F. Gofa, A. Corigliano
(2013):
The CONSENS Priority Project.
DOI: 10.5676/DWD_pub/nwv/cosmo-tr_22

No. 23: M. Baldauf, O. Fuhrer, M. J. Kurowski, G. de Morsier, M. Müllner, Z. P. Piotrowski,
B. Rosa, P. L. Vitagliano, D. Wójcik, M. Ziemiański (2013):
The COSMO Priority Project 'Conservative Dynamical Core' Final Report.
DOI: 10.5676/DWD_pub/nwv/cosmo-tr_23

No. 24: A. K. Miltenberger, A. Roches, S. Pfahl, H. Wernli (2014):
Online Trajectory Module in COSMO: a short user guide.
DOI: 10.5676/DWD_pub/nwv/cosmo-tr_24

No. 25: P. Khain, I. Carmona, A. Voudouri, E. Avgoustoglou, J.-M. Bettems, F. Grazzini
(2015):
The Proof of the Parameters Calibration Method: CALMO Progress Report.
DOI: 10.5676/DWD_pub/nwv/cosmo-tr_25

No. 26: D. Mironov, E. Machulskaya, B. Szintai, M. Raschendorfer, V. Perov, M. Chumakov,
E. Avgoustoglou (2015):
The COSMO Priority Project 'UTCS' Final Report.
DOI: 10.5676/DWD_pub/nwv/cosmo-tr_26

No. 27: J-M. Bettems (2015):
The COSMO Priority Project 'COLOBOC': Final Report.
DOI: 10.5676/DWD_pub/nwv/cosmo-tr_27

No. 28: Ulrich Blahak (2016):
RADAR_MIE_LM and RADAR_MIELIB - Calculation of Radar Reflectivity from Model Output.
DOI: 10.5676/DWD_pub/nwv/cosmo-tr_28

No. 29: M. Tsyrulnikov and D. Gayfulin (2016):
A Stochastic Pattern Generator for ensemble applications.
DOI: 10.5676/DWD_pub/nwv/cosmo-tr_29

No. 30: D. Mironov and E. Machulskaya (2017):
A Turbulence Kinetic Energy – Scalar Variance Turbulence Parameterization Scheme.
DOI: 10.5676/DWD_pub/nwv/cosmo-tr_30

No. 31: P. Khain, I. Carmona, A. Voudouri, E. Avgoustoglou, J.-M. Bettems, F. Grazzini, P. Kaufmann (2017):
CALMO - Progress Report.
DOI: 10.5676/DWD_pub/nwv/cosmo-tr_31

No. 32: A. Voudouri, P. Khain, I. Carmona, E. Avgoustoglou, J.M. Bettems, F. Grazzini, O. Bellprat, P. Kaufmann and E. Bucchignani (2017):
Calibration of COSMO Model, Priority Project CALMO Final report.
DOI: 10.5676/DWD_pub/nwv/cosmo-tr_32

No. 33: N. Vela (2017):
VAST 2.0 - User Manual.
DOI: 10.5676/DWD_pub/nwv/cosmo-tr_33

No. 34: C. Marsigli, D. Alferov, M. Arpagaus, E. Astakhova, R. Bonanno, G. Duniec, C. Gebhardt, W. Interewicz, N. Loglisci, A. Mazur, V. Maurer, A. Montani, A. Walser (2018):
COsmo Towards Ensembles at the Km-scale IN Our countries" (COTEKINO), Priority Project final report.
DOI: 10.5676/DWD_pub/nwv/cosmo-tr_34

No. 35: G. Rivin, I. Rozinkina, E. Astakhova, A. Montani, D. Alferov, M. Arpagaus, D. Blinov, A. Bundel, M. Chumakov, P. Eckert, A. Euripides, J. Förstner, J. Helmert, E. Kazakova, A. Kirsanov, V. Kopeikin, E. Kukanova, D. Majewski, C. Marsigli, G. de Morsier, A. Muravev, T. Paccagnella, U. Schättler, C. Schraff, M. Shatunova, A. Shcherbakov, P. Steiner, M. Zaichenko (2018):
The COSMO Priority Project CORSO Final Report.
DOI: 10.5676/DWD_pub/nwv/cosmo-tr_35

No. 36: A. Raspanti, A. Celozzi, A. Troisi, A. Vocino, R. Bove, F. Batignani (2018):
The COSMO Priority Project VERSUS2 Final Report.
DOI: 10.5676/DWD_pub/nwv/cosmo-tr_36

No. 37: A. Bundel, F. Gofa, D. Alferov, E. Astakhova, P. Baumann, D. Boucouvala, U. Damrath, P. Eckert, A. Kirsanov, X. Lapillonne, J. Linkowska, C. Marsigli, A. Montani, A. Muraviev, E. Oberto, M.S. Tesini, N. Vela, A. Wyszogrodzki, M. Zaichenko, A. Walser (2019):
The COSMO Priority Project INSPECT Final Report.
DOI: 10.5676/DWD_pub/nwv/cosmo-tr_37

No. 38: G. Rivin, I. Rozinkina, E. Astakhova, A. Montani, J-M. Bettems, D. Alferov, D. Blinov, P. Eckert, A. Euripides, J. Helmert, M.Shatunova (2019):
The COSMO Priority Project CORSO-A Final Report.
DOI: 10.5676/DWD_pub/nwv/cosmo-tr_38

No. 39: C. Marsigli, D. Alferov, E. Astakhova, G. Duniec, D. Gayfulin, C. Gebhardt, W. Interewicz, N. Loglisci, F. Marcucci, A. Mazur, A. Montani, M. Tsyrulnikov, A. Walser (2019):
Studying perturbations for the representation of modeling uncertainties in Ensemble development (SPRED Priority Project): Final Report.
DOI: 10.5676/DWD_pub/nwv/cosmo-tr_39

No. 40: E. Bucchignani, P. Mercogliano, V. Garbero, M. Milelli, M. Varentsov, I. Rozinkina, G. Rivin, D. Blinov, A. Kirsanov, H. Wouters, J.-P. Schulz, U. Schättler (2019):
Analysis and Evaluation of TERRA_URB Scheme: PT AEVUS Final Report.
DOI: 10.5676/DWD_pub/nwv/cosmo-tr_40

No. 41: X. Lapillonne, O. Fuhrer (2020):
Performance On Massively Parallel Architectures (POMPA): Final report.
DOI: 10.5676/DWD_pub/nwv/cosmo-tr_41

No. 42: E. Avgoustoglou, A. Voudouri, I Carmona, E. Bucchignani, Y. Levy, J. -M. Bettems (2020):
A methodology towards the hierarchy of COSMO parameter calibration tests via the domain sensitivity over the Mediterranean area.
DOI: 10.5676/DWD_pub/nwv/cosmo-tr_42

COSMO Technical Reports

Issues of the COSMO Technical Reports series are published by the *COnsortium for Small-scale MOdelling* at non-regular intervals. COSMO is a European group for numerical weather prediction with participating meteorological services from Germany (DWD, AWGeophys), Greece (HNMS), Italy (USAM, ARPA-SIMC, ARPA Piemonte), Switzerland (MeteoSwiss), Poland (IMGW), Romania (NMA) and Russia (RHM). The general goal is to develop, improve and maintain a non-hydrostatic limited area modelling system to be used for both operational and research applications by the members of COSMO. This system is initially based on the COSMO-Model (previously known as LM) of DWD with its corresponding data assimilation system.

The Technical Reports are intended

- for scientific contributions and a documentation of research activities,
- to present and discuss results obtained from the model system,
- to present and discuss verification results and interpretation methods,
- for a documentation of technical changes to the model system,
- to give an overview of new components of the model system.

The purpose of these reports is to communicate results, changes and progress related to the LM model system relatively fast within the COSMO consortium, and also to inform other NWP groups on our current research activities. In this way the discussion on a specific topic can be stimulated at an early stage. In order to publish a report very soon after the completion of the manuscript, we have decided to omit a thorough reviewing procedure and only a rough check is done by the editors and a third reviewer. We apologize for typographical and other errors or inconsistencies which may still be present.

At present, the Technical Reports are available for download from the COSMO web site (www.cosmo-model.org). If required, the member meteorological centres can produce hardcopies by their own for distribution within their service. All members of the consortium will be informed about new issues by email.

For any comments and questions, please contact the editor:

Massimo Milelli
Massimo.Milelli@arpa.piemonte.it